# Accurate wideband measurement of human body absorption cross section in reverberation chamber: A morphological parameters study from 1 GHz to 18 GHz

**Xiaotian Zhang**

Doctor of Philosophy

University of York
Electronic Engineering
September 2017

# Abstract

The human body absorption cross section (ACS) is important in the non-ionized dosimetry, indoor channel modelling, design of electrical biomedical devices, etc. In order to find the relations between morphological parameters and the human body ACS, we developed new measurement techniques which can obtain human body ACS quickly and accurately. Empirical models were inducted from the accurate measurement results, which enables the human body ACS to be quickly evaluated from the morphological parameters.

Our researches include the following parts. First, the new measurement techniques which can give ACS result accurately had been validated by measuring the ACS of a sphere model with known structure and material in the reverberation chamber (RC). The measurement result matches very well with the analytical solution of the sphere ACS.

After the new measurement techniques had been validated, measurements on the human body ACS of 48 subjects were performed to find its relation to morphological parameters. A strong linear correlation between the ACS and the body surface area (BSA) was found above 6 GHz and a linear equation was inducted. No strong linear correlations between the ACS and all morphological parameters were found below 6 GHz, therefore, the coordinate of several markers on the ACS curve were correlated to the morphological parameters to evaluate the ACS below 6 GHz.

At last, due to the similarities between the measured ACS and the ACS given by multilayer analytical model, a numerical method that can calculate the ACS of object with arbitrary shape was given. The numerical method was specially optimized for calculating the object with multiple thin surface layers, and its accuracy was demonstrated by solving the ACS of a 2D multilayer cylinder, of which the ACS can be solved analytically. The numerical result matches well with the analytical solution.

# Contents

**Abstract** **i**

**List of Tables** **v**

**List of Figures** **vii**

**List of Symbols** **xiii**

**Acknowledgements** **xv**

**Declaration** **xvii**

**Published Work** **xviii**

**1 Introduction** **1**

1.1 Backgrounds . . . . . 1

1.2 Aims of research . . . . . 2

1.3 Review: Human body ACS and morphological parameters . . 2

1.4 Summary . . . . . 7

**2 Theory** **11**

2.1 Dielectric relaxation and power loss in tissues . . . . . 11

2.2 The multi-layer planar ACS model of human body . . . . . 13

2.3 The Spherical ACS model of human body . . . . . 25

2.4 Measurement of human body ACS in the RC . . . . . 26
2.5 Determining $< Q >$ of RC by IFFT . . . . . 29
2.6 Advantages of determining averaged Q factor by IFFT . . . . 31
2.7 Extracting chamber time constant by linear curve fitting and its inaccuracy . . . . . 33
2.8 The nonlinear curve fitting . . . . . 37
2.9 Estimating the starting value for nonlinear curve fitting . . . . 44
2.10 The early time behaviour of RC and the effect of zero padding in signal processing . . . . . 47
2.11 The variation coefficient of chamber time constant extracted by nonlinear curve fitting . . . . . 49
2.12 Evaluating the variation coefficient of ACS from the variation coefficient of chamber time constant . . . . . 53
2.13 The chamber time constants can give ACS with smaller variation coefficient than the G factors do . . . . . 56
2.14 Summary . . . . . 58

**3 Validation experiments of IFFT techniques 60**
3.1 The selection of reference object . . . . . 60
3.2 The University of York reverberation chamber . . . . . 61
3.3 Calculating the independent number of $S_{21}$ samples . . . . . 63
3.4 Choosing the stirrer speed . . . . . 65
3.5 Segmented sweeping . . . . . 68
3.6 Measurement results: Non-shifted model and shifted model . . 69
3.7 Measurement results: application of different window functions 70
3.8 Measurement results: IFFT method vs. G factor method . . . 73
3.9 Measurement results: Measurement range of ACS . . . . . 78
3.10 The polystyrene sheets to support human subjects . . . . . 81

3.11 Determining the structure of the sphere model by genetic algorithm . . . . . 82
3.12 Summary . . . . . 85

**4 Human body ACS measurement 86**
4.1 The ACS of human body with different postures . . . . . 86
4.2 Populations under study . . . . . 87
4.3 The skin fold thickness formula for evaluating body fat percentage . . . . . 90
4.4 The skin fold measurement techniques . . . . . 93
4.5 The human ACS measurement result . . . . . 97
4.6 Simple predictors of human body ACS . . . . . 104
4.7 Expansion of human body absorption coefficient into series of models absorption coefficient . . . . . 107
4.8 Impedance patching on the surface . . . . . 117
4.9 Summary . . . . . 131

**5 Conclusion 134**
5.1 Future works . . . . . 135

**6 Appendices 137**
6.1 Huygen's equivalent principle . . . . . 137

**List of Abbreviations 142**

**Bibliography 144**

# List of Tables

1.1 An overview of voxel models and their morphological parameters. Citations were put on the right side of the data to show where does it come from. The asterisk '*' means BFP values were not directly given but calculated from the fat masses and body masses given in the literature. . . . . 8

3.1 The setups of sphere measurement. The 'Repeats of frequency sweeping' means the times of frequency sweeping from 1 GHz to 18 GHz during the 'Measurement time'. Techniques of segmented frequency sweeping were applied in all the measurements, which is introduced in Sec. 3.5. The total number of frequency samples from 1 GHz to 18 GHz is 8721. . . . . 66

3.2 Mean absolute percentage error (MAPE) of cube ACS measurement . . . . . 79

3.3 Setups for GA optimization . . . . . 83

3.4 A comparison of GA optimized sphere parameters and measured parameters . . . . . 84

4.1 The SFT equations for estimating BFP and BD. $S$ denotes the sum of all skin folds in mm. $Y$ is age in years. BD is body density in grams/cc. $(M)$ means male. $(F)$ means female. The parameters of SFT equation #1 and #2 were listed in Table 4.2 and Table 4.3 . . . . . 92
4.2 the $c_1$ and $m_1$ value for male subjects . . . . . 92
4.3 the $c_1$ and $m_1$ value for female subjects . . . . . 92
4.4 The morphological parameters of 48 subjects. 'N': Subject number, 'G': Gender, 'F': Female, 'M': Male, 'E': Ethics, 'Y': Age in years, 'H': Height in cm, 'W': Weight in kg, 'SF1': Skin fold at abdominal site in mm, 'SF2': Skin fold at tricep site in mm, 'SF3': Skin fold at thigh site in mm, 'SF4': Skin fold at supraillium site in mm, 'N/A': the skin over thigh is too tight to measure the skin fold. . . . . 95
4.5 Linear relations between $\xi$ and morphological parameters at 2.5 GHz . . . . . 103
4.6 Correlation coefficient between simple predictors and morphological parameters, the parameters in bold font are the correlation coefficients whose absolute value higher than 0.5 . . . . 106

# List of Figures

1.1 The $WBSAR_{max}$ comparison between NORMAN and NAOMI 6

1.2 The $WBSAR_{max}$ comparison between TARO and HANAKO . 6

1.3 Documented $WBSAR_{max}$ of male voxel models: 1. NORMAN, data from [22], figure resolution $2.4 \times 10^{-4}$ mW/kg; 2. Zubal, data from [16], figure resolution $1.2 \times 10^{-4}$ mW/kg; 3. TARO, data from [13], 4. Duke, data from [20], figure resolution $1.2 \times 10^{-4}$ mW/kg; 5. CVH Male, data from [20], figure resolution $1.2 \times 10^{-4}$ mW/kg; 6. VIP Man, data from [16], figure resolution $1.2 \times 10^{-4}$ mW/kg, 7-9. VCH Deformable models, data from [15], figure resolution $1.2 \times 10^{-4}$ mW/kg. The E-field are all vertically polarized and the strength is 1 V/m. The asterisk '*' means data is extracted from the plot in the document. The 'figure resolution' means the resolution of original figure from which the data is extracted. . . . . 9

1.4 Documented $WBSAR_{max}$ of female voxel models: 1. NAOMI, data from [5]; 2. HANAKO, data from [13]; 3. CVH Female, data from [20], figure resolution $1.2 \times 10^{-4}$ mW/kg; 4. Ella, data from [20], figure resolution $1.2 \times 10^{-4}$ mW/kg. The E-field are all vertically polarized and the strength is 1 V/m. The asterisk '*' means data is extracted from the plot in the document. The 'figure resolution' means the resolution of original figure from which the data is extracted. . . . . 10

2.1 The real part of permittivity of three major tissues at the surface of human body [28] . . . . . 14
2.2 The imaginary part of permittivity of three major tissues at the surface of human body [28] . . . . . 15
2.3 Transmission coefficient of three different tissues . . . . . 16
2.4 The penetration depth of three different tissues . . . . . 16
2.5 The multilayer ACS model . . . . . 19
2.6 The multi-reflection in each layer of planar model . . . . . 19
2.7 The absorption coefficient of planar model with different fat layer thickness (2 mm skin layer thickness) . . . . . 20
2.8 Resonant frequencies of planar model, skin layer thickness = 2 mm . . . . . 21
2.9 Percentage of power loss in each layer of multi-layer planar model: 2mm fat layer thickness . . . . . 23
2.10 Percentage of power loss in each layer of multi-layer planar model: 6mm fat layer thickness . . . . . 23
2.11 Percentage of power loss in each layer of multi-layer planar model: 10mm fat layer thickness . . . . . 24
2.12 Percentage of power loss in each layer of multi-layer planar model: 14mm fat layer thickness . . . . . 24

2.13 The absorption coefficient of the multi-layer spherical model . 26
2.14 The measured PDP at one stirrer position in the RC . . . . . 31
2.15 The measured PDP averaged over 200 stirrer positions in the RC . . . . . 32
2.16 The linear fitting range is selected as the top half of PDP . . . 34
2.17 PDP extracted by applying different window functions at 15 GHz. Win #1: total width 5 MHz, 100 kHz frequency step, 51 samples; Win #2: total width 2 MHz, 100 kHz frequency step, 21 samples; Win #3: total width 1 MHz, 100 kHz frequency step, 11 samples. The filtered $S_{21}$ were all padded to zero frequency to show the ringing effect of piecewise window functions in full detail, because adding more zeros to the discrete spectrum of $S_{21}$ in frequency domain is equivalent to increasing the resolution of signal in time domain [49]. . . . . 36
2.18 Linear curve fitting results of different PDP extracted by applying different window functions . . . . . 37
2.19 The Quantile-Quantile plot of the real part of CIR h($n_0\Delta t$) where $n_0\Delta t = 5\mu s$ . . . . . 39
2.20 The Quantile-Quantile plot of the imaginary part of CIR h(5 $\mu s$) . . . . . 40
2.21 the nonlinear model matches well with the PDP . . . . . 43
2.22 The first and final estimation of PDP . . . . . 46
2.23 The RMS difference between estimated PDP and measured PDP 47
2.24 The PDP without shift and PDP shifted 0.4 $\mu$s . . . . . 48
2.25 The benefit of including the delay of PDP's first peak in nonlinear curve fitting . . . . . 50
2.26 The fitting quality of nonlinear fit with shifted model and nonshifted model . . . . . 51

2.27 Delay of the first peak of PDP. The quantized level is due to the times step of PDP. The sample number of $S_{21}$ in IFFT is 512 (including the number of padded zeros), and the frequency step is $\Delta f = 100$kHz. So the time step can be calculated by $\Delta t = \frac{1}{512 \times \Delta f} \approx 0.02$ns . . . . . 52
2.28 Monte Carlo method of evaluating uncertainty of chamber time constant measurement . . . . . 54

3.1 Top View of the University of York RC . . . . . 62
3.2 The small RC . . . . . 62
3.3 Correlation coefficient of $S_{21}$ vs stirrer position lag . . . . . 63
3.4 correlation coefficient of s21 vs frequency lag . . . . . 64
3.5 Correlation functions in the RC loaded with reference sphere . 67
3.6 Correlation functions in the empty RC . . . . . 67
3.7 The segmented frequency sweeping setups . . . . . 68
3.8 The measurement setups of the sphere model . . . . . 69
3.9 Benefit of fitting with shifted PDP model on ACS measurement 71
3.10 The ACS extracted by linear curve fitting . . . . . 72
3.11 The ACS extracted by nonlinear curve fitting . . . . . 73
3.12 The measurement setups for evaluating ACS measurement uncertainty . . . . . 74
3.13 The ACS extracted by G factor method and the ACS extracted by IFFT method . . . . . 75
3.14 The picture of the ventilation panel in the University of York RC . . . . . 76
3.15 The structure of the ventilation panel in the University of York RC . . . . . 76
3.16 The coefficient of variation of measured ACS . . . . . 77
3.17 The series of absorber cuboids, made from carbon-loaded foam 79

3.18 The ACS of the absorber cuboids extracted by Win #1. The dashed line is the results calculated by Mie series. . . . . 80
3.19 ACS of polystyrene sheets . . . . . 82
3.20 The ACS of Sphere: comparison between measurement value and Mie results . . . . . 84

4.1 The five different postures measured in the RC. The names of the all poses are (left to right, top to bottom): Seated-1, Seated-2, Supine-Normal, Supine-Star, Supine-X . . . . . 88
4.2 The human body ACS of the subject in Fig. 4.1 in five different postures . . . . . 89
4.3 The normalized human body ACS the subject in Fig. 4.1 in four different postures . . . . . 89
4.4 The population composition of 48 subjects under test . . . . . 91
4.5 BFP calculated by empirical SFT equation vs. BFP calculate by BMI . . . . . 96
4.6 The overview of the ACS of human body. The outlier belongs to the subject with very high BMI, which is 47.0kg/m$^2$, while the average BMI of the rest of the subjects is 23.2kg/m$^2$ . . . 97
4.7 the ACS of subjects with maximum, mean, and minimum skin fold readings . . . . . 98
4.8 The correlation coefficient between human body ACS and morphological parameters at different frequencies . . . . . 99
4.9 The coefficient of linear ACS model from 6 GHz to 18 GHz . . 100
4.10 $R^2$ of linear ACS model . . . . . 101
4.11 The overview of the absorption coefficient of human body . . . 102
4.12 The correlation coefficient between human body absorption coefficient and morphological parameters at different frequencies 102
4.13 Features of absorption coefficient . . . . . 104

4.14 The absolute value of correlation coefficient between simple predictors and morphological parameters . . . . . 105
4.15 The linear regression of simple predictors . . . . . 108
4.16 The linear regression of simple predictors . . . . . 109
4.17 The linear regression of simple predictors . . . . . 110
4.18 The basis functions for expanding absorption coefficient of Subject No. 1 . . . . . 115
4.19 Fitting the absorption coefficient of Subject No.1 by genetic algorithm . . . . . 115
4.20 The GA predicted SFT vs. SFT measured by calliper, the red line is the reference line. The more accurate the GA prediction, the closer the dots to the reference line . . . . . 116
4.21 The value of minimized cost function . . . . . 116
4.22 The GA predicted SFT of 10 times of optimization . . . . . 117
4.23 The value of cost functions of 10 times of optimization . . . . 118
4.24 Field transmission through multilayer structure . . . . . 122
4.25 The coated water cylinder scattered by a TM wave . . . . . 125
4.26 Equivalent problems of a plane wave scattered by a coated water cylinder . . . . . 126
4.27 The point pairs on the surface . . . . . 128
4.28 The E-field on the outer surface of cylinder at 6 GHz . . . . . 129
4.29 E field on the outer surface of the muscle cylinder at 6 GHz . 130
4.30 The EM power absorbed by a unit length of the muscle cylinder 131

6.1 The Huygens equivalent principle . . . . . 137
6.2 The equivalent problems of scattering problem . . . . . 139

# List of Symbols

| | |
|---|---|
| $P_d$ | power dissipated in the media |
| $m$ | mass |
| $P_{d,wb}$ | power dissipated into the whole human body |
| $\vec{S}$ | Poynting vector |
| $\vec{E}$ | electric field |
| $\vec{H}$ | magnetic field |
| $\epsilon$ | dielectric permittivity |
| $k$ | wave number |
| $\mu$ | dielectric permeability |
| $\lambda$ | wave length |
| $j$ | imaginary unit |
| $\omega$ | angular frequency |
| $\sigma$ | conductivity |
| $d_{\text{penetration}}$ | the dielectric penetration depth |
| $\tau_d$ | dielectric relaxation time |
| $T$ | transmission coefficient |
| $Z$ | characteristic impedance in the media |
| $\xi$ | absorption coefficient |
| $\sigma_a$ | the absorption cross section |
| $Q$ | the Q factor |

| | |
|---|---|
| $Q_{wo}$ | the Q factor of reverberation chamber with object loaded |
| $Q_{no}$ | the Q factor of reverberation chamber with no object loaded |
| $U$ | energy stored in the reverberation chamber |
| $V$ | volume of the reverberation chamber |
| $W$ | Energy density |
| $c$ | speed of light |
| $G$ | the net transfer function |
| $S_{mn}$ | the scattering parameter between port 'm' and port 'n' |
| $\eta_{\mathrm{Tx}}$ | radiation efficiency of transmitting antenna |
| $\eta_{\mathrm{Rx}}$ | radiation efficiency of receiving antenna |
| $\tau$ | the chamber time constant |
| $h(t)$ | channel impulse response |
| $N(t)$ | Gaussian random process with zero mean and variance of one |
| $W(k)$ | window function in frequency domain |
| $N_{\mathrm{ind}}$ | independent number of $S_{21}$ samples |
| $c_v$ | variation coefficient |
| $\xi$ | absorption coefficient |
| $\vec{J}$ | electric current |
| $\vec{M}$ | magnetic current |

# Acknowledgements

Producing this thesis is not a easy task. When I look back, I should say the work would not even be possible with out the help of many people. I really appreciate all your work in this research and I will always keep your guidance and advices in my mind.

Firstly, I want to thank my supervisor Dr. Martin P. Robinson, who is a really open-mind and easy going person. He gave so much support to all the idea of mine, and he showed me what the scientific research was like by his rich experience in bio-medical engineering. For those unaccomplished idea I have discussed with him, I will try my best to realize them. Thank you so much Martin!

Then, I want to give my great thankfulness to Dr. Ian D. Flintoft, who is a super regiment and highly skilled researcher. I can't remember how many times I have interrupted his work by my silly question, but he always stopped and gave me the feed back. Because of his super high level of theoretical knowledge, the problem in my research can be quickly handled. Thank you so much Ian!

I also want to thank to Dr. John F. Dawson, who is really a critical thinker and a walking encyclopaedia. His mastering of engineering skills makes the fascinate ideas being realized instantly. Its him that help me to get things going when the research work got stuck. His words at the weekly meeting is very helpful in my preceding of research. Thank you so much

John!

I want to thank my parents, Zhang Juan and Zhang Xiaohu, who gave me unbelievably many encouragement and love when I want to give up. I truly feel the parents love is the greatest love in the world. My thesis is also my greatest gift to them. I will try to be the best version of myself in the future, and I love you all, my beloved families.

I want to thank Dr. Shane Thurlow, who gave me hand to hand instructions on how to do the skin fold measurement. He drove tens of miles to my lab to show me how the measurement was done all for free. Thanks a lot Shane! And also, thanks to Sarah Parker who acted as my female experimenter when doing skin fold measurements on female subjects!

I want to thank everyone who has ever helped me in my oversea studying life: Murtaza Ali, Yahui Wu, Qinhui Huang, and my landlord Robert Hustwick. With your help, I can focus on my research without worrying trifling things daily.

At last, thanks to all the subjects who have taken part in this research. Thanks to your contributions to the human knowledge and the progress of science!

# Declaration

I declare that this thesis is a presentation of original work and I am the sole author. This work has not previously been presented for an award at this, or any other, University. All sources are acknowledged as References.

# Published Work

- X. Zhang, M.P. Robinson, I.D. Flintoft, and J.F. Dawson. "*Efficient Determination of Reverberation Chamber Time Constant.*" IEEE Transactions on Electromagnetic Compatibility, Dec. 2017.

- X. Zhang, M.P. Robinson, I.D. Flintoft, and J.F. Dawson. "*Inverse fourier transform technique of measuring averaged absorption cross section in the reverberation chamber and Monte Carlo study of its uncertainty*" 2016 International Symposium on Electromagnetic Compatibility (EMC EUROPE), pp. 263-267, Sep. 2016.

- X. Zhang, M.P. Robinson, I.D. Flintoft, and J.F. Dawson. "*On measurement of reverberation chamber time constant and related curve fitting techniques*" 2015 International Symposium on Electromagnetic Compatibility (EMC EUROPE), pp. 263-267, Sep. 2015.

- M.P. Robinson, X. Zhang, I.D. Flintoft "*Time Domain Technique for Rapid, Broadband Measurement of Human Absorption Cross Section in a Reverberation Chamber*". 32nd URSI General Assembly and Scientific Symposium, Aug, 2016.

# Chapter 1

# Introduction

## 1.1 Backgrounds

The human body is a heterogeneous object with complex shape. It is formed by numerous different types of tissues, which makes its electromagnetic (EM) properties hard to model. However, there are many applications in which the knowledge of the EM properties of the human body is important, such as the non-ionizing dosimetry, indoor radio channel modelling, military defence and so on [1].

Our research focuses on measuring absorption cross section (ACS) of human body in diffuse environment because it is the diffuse EM fields under which the human body is exposed on daily basis.

We introduced new techniques to improve the measurement speed and accuracy. A group study was performed on 48 subjects and the empirical formulas were inducted for evaluating the human body ACS from morphological parameters. The measurement also provides valuable reference data for future researchers who will be studying the same topic.

## 1.2 Aims of research

There are three aims of our research.

The first aim of the research is to develop techniques of measuring the human body ACS in the reverberation chamber (RC) as accurate as possible and to record human body ACS data for the future researchers.

The second aim is to model the human body ACS by morphological parameters.

The third aim of this research is to explain the ACS by the mechanism of EM power loss in human body by basic EM theories.

## 1.3 Review: Human body ACS and morphological parameters

Before starting the measurement on the ACS of human body, it is quite necessary to have a review on the previous researches of modelling human body ACS by morphological parameters, such as height, body mass, body fat percentage (BFP) and so on.

Instead of quantifying the non-ionizing dosimetry of human body by the ACS, most of the previous papers use specific absorption rate (SAR). The SAR is defined as the normalization of the EM power dissipated in a particular piece of tissue by its weight [2]:

$$\mathrm{SAR} = \frac{P_d}{m} \tag{1.1}$$

where $P_d$ is the EM power dissipated in the piece of tissue in the human body; $m$ is the mass of that tissue.

Since human body is not isotropic, $P_d$ would change with different excitation field. In particular, when the excitation field is a plane wave incident

from a specific direction, $P_d$ would be a function of angles of incident plane waves, written as:

$$\mathrm{SAR}(\theta, \phi) = \frac{P_d(\theta, \phi)}{m} \tag{1.2}$$

where $(\theta, \phi)$ denotes the direction of incident plane wave in the classical spherical coordinate. $\theta$ is the angle between wave vector and $z$ axis. $\phi$ is the angle between wave vector and $x$ axis.

If $P_d(\theta, \phi)$ was chosen as all the power dissipated in human body, the whole body SAR (WBSAR) can be obtained by [3]:

$$\mathrm{WBSAR}(\theta, \phi) = \frac{P_{d,wb}(\theta, \phi)}{M} \tag{1.3}$$

where $P_{d,wb}(\theta, \phi)$ is all the EM power dissipates in the human body, $M$ is the whole body mass. The WBSAR$(\theta, \phi)$ can be converted to the human body ACS by the following equation [3]:

$$\sigma_a(\theta, \phi) = \frac{P_{d,wb}(\theta, \phi)}{|\vec{S}(\theta, \phi)|} = \frac{\mathrm{WBSAR}(\theta, \phi) \cdot M}{|\vec{S}(\theta, \phi)|} \tag{1.4}$$

where $\sigma_a(\theta, \phi)$ denotes the human body ACS. $\vec{S}(\theta, \phi)$ is the Poynting vector of the incident plane wave. The magnitude of $\vec{S}(\theta, \phi)$ equals to the energy flux density.

Since it is hard to measure the WBSAR$(\theta, \phi)$ at a particular direction, numerical calculation was widely used in the study on the morphological parameters' effects on non-ionizing dosimetry. There are two advantages of studying WBSAR$(\theta, \phi)$ by numerical calculation: First, the numerical calculation is easier to perform than measuring the WBSAR$(\theta, \phi)$ and the excitation field can be set arbitrarily; Second, the 3-dimensional (3D) numerical models involved in WBSAR$(\theta, \phi)$ calculation usually have well documented internal morphological parameters such as body fat percentage (BFP). Among all the methods of calculating the WBSAR$(\theta, \phi)$, the finite difference time do-

main (FDTD) method is the most popular one [4, 5]. The FDTD method discretizes the solution region into many small coupling cells, and the field in each cell is calculated by the numerical differentiation. Since the FDTD does not involve solving big matrix, it is good at solving high frequency problems with electrically large objects. But in the study of morphological parameters' effects on the WBSAR$(\theta, \phi)$, the disadvantage of numerical calculation is apparent as well. The high resolution voxel models are usually constructed from the magnetic resonance imaging (MRI) or the pictures of pathological slices of the human body. Obtaining the section images would be very time consuming and expensive, which makes the numerical method poor for large population study. Fortunately, there had already been a lot of studies on the numerical calculation of the WBSAR$(\theta, \phi)$ of different voxel models. The results of all these studies could shed some light on how the WBSAR$(\theta, \phi)$ is changed by morphological parameters.

Since WBSAR$(\theta, \phi)$ depends upon the direction, we should choose a specific direction of incident wave for inter-comparison between different studies. Gandhi had pointed out the standing human body absorbs the most EM power when the incident plane wave whose E-field is vertically polarized is coming from the front [6]. This setup of incident wave is most commonly studied by many researchers. Here we denote the value of WBSAR$(\theta, \phi)$ calculated in this case as $\mathrm{WBSAR}_{\mathrm{max}}$.

In the 1970s, due to the relatively low computational power, the resolution of human voxel model was low. Hagmann calculated the $\mathrm{WBSAR}_{\mathrm{max}}$ of a human voxel model consisted of only 180 cells by the method of moments (MoM) [7]. The dielectric properties of each cell in Hagmann's model was assigned with respect to anatomical cross sections photos.

Since the low efficiency of MoM in memory usage, the calculation of $\mathrm{WBSAR}_{\mathrm{max}}$ at higher frequencies was hard to perform until 1987, Sullivan introduced the FDTD method into the SAR calculation [8].

One year later in 1988, Dimbylow published his research on calculating the SAR of the high resolution lower leg voxel model by FDTD method [9]. Dimbylow then conducted the well known research of building up a voxel model called NORMAN [4]. NORMAN was constructed via MRI scan of a human male and the model is consisted by 9 million cells. The height and weight of the model were normalized to the reference man in the ICRP 66 (International Commission on Radiological Protection), hence its name 'NORMAN' [10]. Thanks to the high resolution of 'NORMAN', the $\mathrm{WBSAR_{max}}$ was able to be calculated up to the frequency of 1 GHz.

After 1997, numerous similar researches were conducted but with different voxel models. Considering the morphological difference between Asian and Caucasian, the Japanese voxel models were developed by Nagaoka in 2003 [11]. the Japanese models include a male model and a female model. Both of the models were constructed from the MRI image of volunteers. The $\mathrm{WBSAR_{max}}$ of the Japanese models were calculated from 30 MHz to 3 GHz [11].

In 2005, the voxel model NAOMI was developed by Dimbylow as a female counterpart of NORMAN [12], and the $\mathrm{WBSAR_{max}}$ value of NAOMI was published in his later research [5]. Comparing to the $\mathrm{WBSAR_{max}}$ of NORMAN, the $\mathrm{WBSAR_{max}}$ curve of NAOMI has a "hump" at about 900 MHz while the $\mathrm{WBSAR_{max}}$ of NORMAN is flat. This hump makes the WBSAR of NAOMI 25% higher than that of NORMAN. (See Fig. 1.1) The higher $\mathrm{WBSAR_{max}}$ of NAOMI at 900 MHz was attributed to the thicker subcutaneous fat layer thickness. The Japanese female model HANAKO also has a 17% higher $\mathrm{WBSAR_{max}}$ at 900 MHz than her male conterpart TARO [13] (See Fig. 1.2).

The higher $\mathrm{WBSAR_{max}}$ of female model was also reported by Sandrini [14]. In Sandrini's work, the pose and scale of the female voxel model were adjusted to that of the male model and a constant higher $\mathrm{WBSAR_{max}}$ was

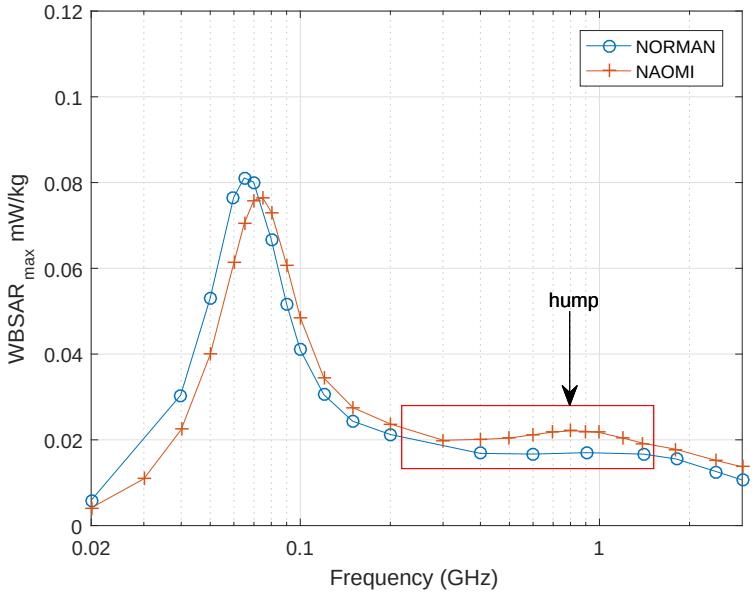


Figure 1.1: The $\mathrm{WBSAR}_{\mathrm{max}}$ comparison between NORMAN and NAOMI

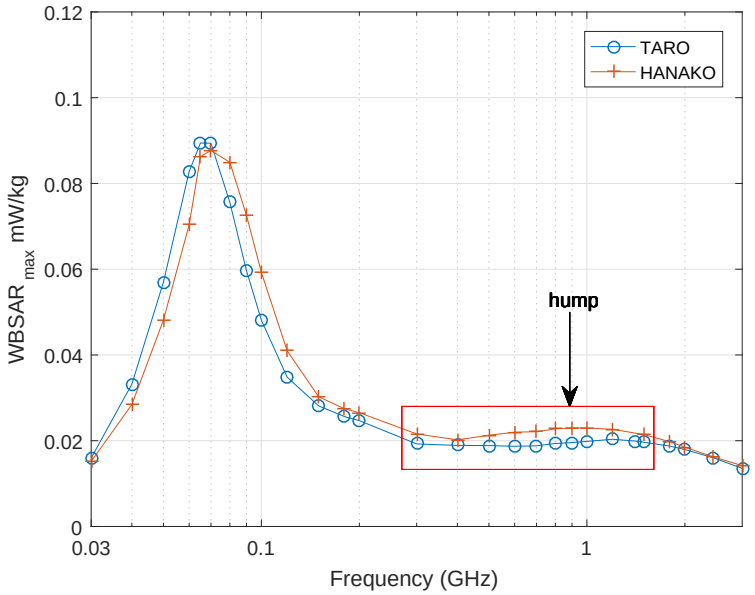


Figure 1.2: The $\mathrm{WBSAR}_{\mathrm{max}}$ comparison between TARO and HANAKO

given by modified female model from 1 GHz to 4 GHz.

However, there are also researchers gave contradictory results on the effect of body fat on $WBSAR_{max}$. Yu preformed a study on the deformable polygon human models [15]. The deformable human model was deformed to three different body types of the same height (underweight, normal weight, overweight) by adjusting the body fat percentage (BFP) , then the the model was voxelized to calculate the $WBSAR_{max}$. Results shown the model with higher body mass index (BMI) tend to have lower $WBSAR_{max}$ from 20 MHz to 3 GHz.

The negative correlation between the BMI and $WBSAR_{max}$ from 80 MHz to 2.4 GHz was given in Conil's work in which the $WBSAR_{max}$ of five different voxel models were computed [16]. Similar conclusion was also given by Hirata [17]. He also suggested that the lower $WBSAR_{max}$ at resonant frequencies was caused by higher BFP. Except from the voxel models mentioned above, there are many other voxel models with well documented morphological parameters and the $WBSAR_{max}$, such as the VIP-man [18, 19], the Chinese visible human (CVH) models [20], the High definition reference korean man (HDRK) [21], etc. The morphological parameters of all these models were listed in Table 1.1, and the documented $WBSAR_{max}$ were plotted in Fig. 1.3 and Fig. 1.4.

## 1.4 Summary

A simple review on the human body ACS was done in this chapter. The previous researchers gave contradictory conclusions on the effect of morphological parameters on the ACS. Some researchers suggest high BFP would increase $WBSAR_{max}$ while others hold the opposite view. Due to the lack of experiments on measurement of human body ACS, we will present the accurate measurement techniques and show the relation between morphological parameters and the human body ACS in the following chapters.

| Name | Gender | Weight (kg) | Height(cm) | Ethnicity | BFP% | Image | comments |
|---|---|---|---|---|---|---|---|
| NORMAN [4, 22] | male | 73 | 176 | Caucasian | 22 % [16] | MRI | |
| NAOMI [12] | female | 60 | 163 | Caucasian | 40.10%*[12] | MRI | Fat including breast tissue |
| Zubal [23] | male | 70 | 178 | Caucasian | 18%[16] | CT | Morphological parameters are obtained from measuring volunteers, not voxel data. |
| TARO [11] | male | 65 | 173 | Asian | 22 %* [11] | MRI | |
| HANAKO [11] | female | 53 | 160 | Asian | 31%* [11] | MRI | |
| Duke [24] | male | 70 | 174 | Caucasian | 17% [20] | MRI | |
| Ella [24] | female | 58 | 160 | Caucasian | 25% [20] | MRI | |
| HDRK [21] | male | 68 | 171 | Asian | 34%* [21] | Section Photo | The extra adipose tissue was added to adjust the weight and inner organ size of HDRK to that of the reference Korean model [25] |
| CVH Male [20] | male | 63 | 172 | Asian | 24% [20] | Section Photo | |
| CVH Female [20] | female | 54 | 162 | Asian | 35% [20] | Section Photo | |
| VIP Man [18] | male | 104 | 186 | Caucasian | 35%*[18] | Section Photo | |
| VCH Deformable [15] | male | 53 | 170 | Asian | 30%[15] | Section Photo | |
| | | 62 | | | 38%[15] | | |
| | | 75 | | | 48%[15] | | |

Table 1.1: An overview of voxel models and their morphological parameters. Citations were put on the right side of the data to show where does it come from. The asterisk '*' means BFP values were not directly given but calculated from the fat masses and body masses given in the literature.

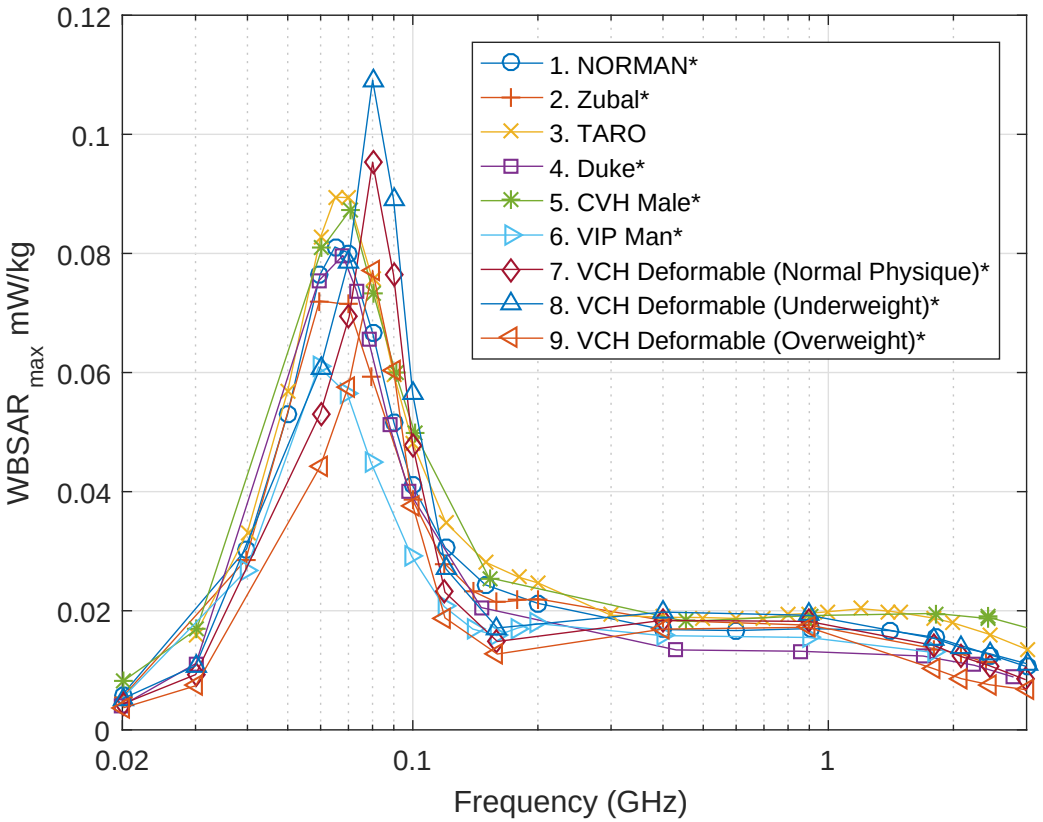


Figure 1.3: Documented $\mathrm{WBSAR}_{\mathrm{max}}$ of male voxel models: 1. NORMAN, data from [22], figure resolution $2.4 \times 10^{-4}$ mW/kg; 2. Zubal, data from [16], figure resolution $1.2 \times 10^{-4}$ mW/kg; 3. TARO, data from [13], 4. Duke, data from [20], figure resolution $1.2 \times 10^{-4}$ mW/kg; 5. CVH Male, data from [20], figure resolution $1.2 \times 10^{-4}$ mW/kg; 6. VIP Man, data from [16], figure resolution $1.2 \times 10^{-4}$ mW/kg, 7-9. VCH Deformable models, data from [15], figure resolution $1.2 \times 10^{-4}$ mW/kg. The E-field are all vertically polarized and the strength is 1 V/m. The asterisk '*' means data is extracted from the plot in the document. The 'figure resolution' means the resolution of original figure from which the data is extracted.

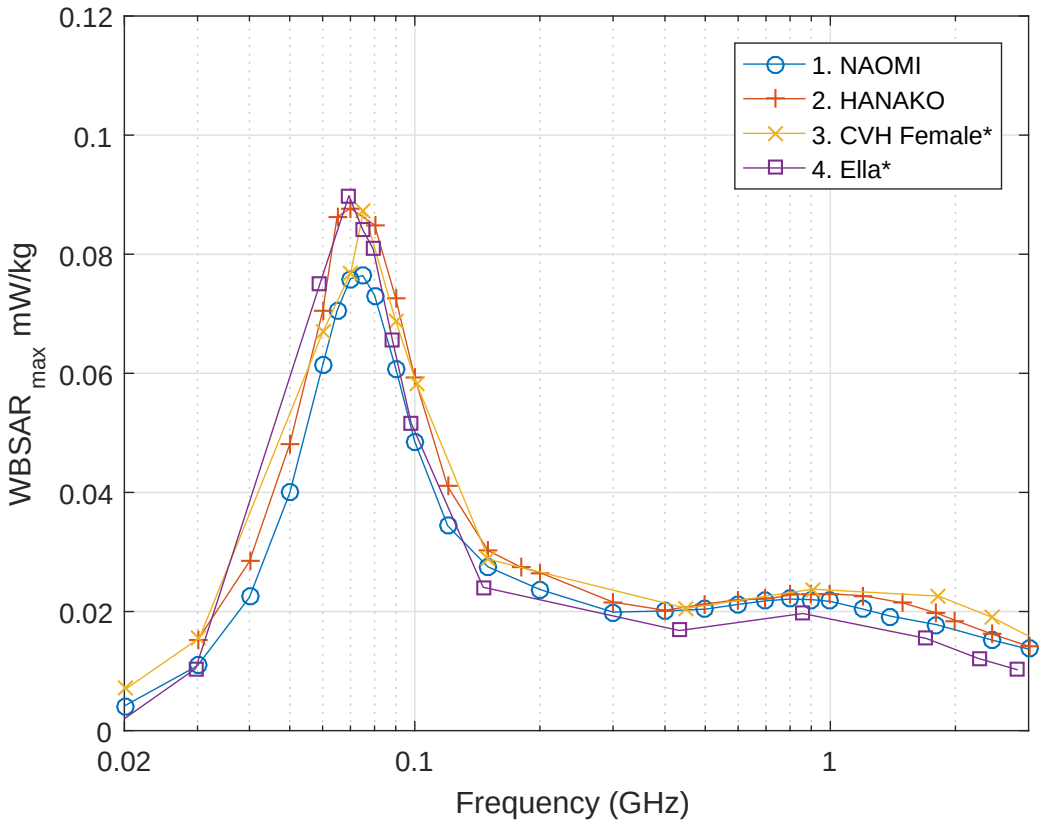


Figure 1.4: Documented $\mathrm{WBSAR}_{\mathrm{max}}$ of female voxel models: 1. NAOMI, data from [5]; 2. HANAKO, data from [13]; 3. CVH Female, data from [20], figure resolution $1.2 \times 10^{-4}$ mW/kg; 4. Ella, data from [20], figure resolution $1.2 \times 10^{-4}$ mW/kg. The E-field are all vertically polarized and the strength is 1 V/m. The asterisk '*' means data is extracted from the plot in the document. The 'figure resolution' means the resolution of original figure from which the data is extracted.

# Chapter 2

# Theory

## 2.1 Dielectric relaxation and power loss in tissues

The relaxation rate of a material tells how fast its state change when a stress is suddenly applied on it, or conversely, how fast it would return to its original state when the stress is suddenly being removed (even though sometimes the material would no longer change back to its original state) [26]. Here the stress is applied by electromagnetic field, and the status of material is the electrical polarization strength of the tissue. According to Poynting's Theorem, the power loss in a non-ferrite lossy material is [27]:

$$\mathrm{Re}\left(\oint_S \vec{E} \times \overrightarrow{H^*} \mathrm{d}S\right) = \mathrm{Re}\left(\int_V j\omega(\epsilon^*|\vec{E}|^2 - \mu|\vec{H}|^2)dV\right) \tag{2.1}$$

where $\epsilon$ is the complex permittivity. $\omega$ is the angular frequency; $\vec{E}$ is the electric field; $\vec{H}$ is the magnetic field; $\mu$ is the permeability of the lossy material; Here the star '*' symbol means complex conjugation. The real part of both sides of the equation would be non-zero only if the permittivity $\epsilon$

is a complex number because $\mu$ of a non-ferrite material is real. In other words, the dielectric relaxation is the reason of heat loss in non-ferrite lossy material, such as human tissue.

A literature survey on the permittivity of human tissues had been done by Gabriel [28]. In his survey, Gabriel pointed out that at GHz region, the relaxation is dominated by the polarization of water molecules [28]. The complex permittivity of tissues has form:

$$\epsilon = \epsilon' - j\frac{\sigma}{\omega} \tag{2.2}$$

where $\epsilon'$ is the real part of permittivity. $\sigma$ is the conductivity. (2.2) shows the imaginary part of $\epsilon$ is controlled by $\sigma$, which affects the total absorption power with respect to (2.1).

In order to clearly demonstrate the how lossy the material is, the 'penetration depth' is used to show how effectively an electromagnetic wave can transmit through a material. The penetration depth is given in (2.3), which only stands when $\sigma \gg \omega\epsilon'$:

$$d_{\text{penetration}} = \sqrt{\frac{2}{\omega\mu\sigma}} \tag{2.3}$$

where $d_{\text{penetration}}$ is penetration depth. The complex permittivity $\epsilon$ of tissues in frequency domain is not a constant but a spectrum varying with frequencies. Debye model is one of the most simplest dielectric relaxation model[29]. By assuming the polarization level decreases exponentially after the stress is removed, the Debye model in frequency domain can be given by Fourier transform:

$$\epsilon = \epsilon_\infty + \frac{\epsilon_\infty - \epsilon_s}{1 + j\omega\tau_d} \tag{2.4}$$

where $\epsilon_s$ and $\epsilon_\infty$ are the permittivity at zero frequency and the permittivity as frequency approaches infinity; $\tau_d$ is the relaxation time constant. The

Debye model has only three degrees of freedom which makes it inaccurate in modelling the complex dielectric relaxation behaviour.

It Gabriel's work, the Cole-Cole model with more parameters was used to fit the dielectric properties of tissues [30, 31]:

$$\epsilon = \epsilon_\infty + \sum_n \frac{\Delta\epsilon_n}{1 + (j\omega\tau_n)^{(1-\alpha_n)}} + \frac{\sigma}{j\omega\epsilon_0} \tag{2.5}$$

where $\epsilon_0$ is the permittivity in free space; $\Delta\epsilon_n$ is the $n$th term of total permittivity; $\tau_n$ is the $n$th relaxation time; the index $\alpha_n$ is the index which determines the order of the $n$th relaxation time. Gabriel chose max(n)=4. Comparing to the Debye model, the Cole-Cole model achieves a better fitting accuracy, but the non-integer index $(1-\alpha_n)$ on $j\omega$ makes it hard to map the operator '$j\omega$' in the frequency domain to the partial differentiation operator $\frac{\partial}{\partial t}$ of time domain Maxwell's equations, thus the Cole-Cole model is hard to apply to FDTD[32]. The mapping solution is given in [33], which is $\Gamma$ function involved:

$$j\omega(j\omega)^{\beta-1}P(\omega) \xrightarrow{\text{IFT}} \frac{\partial}{\partial t}\int_0^t \frac{1}{\tau^\beta\Gamma(1-\beta)}P(t-\tau)d\tau \tag{2.6}$$

where $\beta = 1 - \alpha_n$; $P(t)$ is an arbitrary function whose Fourier transform is $P(\omega)$; 'IFT' is the abbreviation of inverse Fourier transform.

## 2.2 The multi-layer planar ACS model of human body

Previous researches have shown that the human body resonates at tens of MHz at which the body height is about 0.36-0.4 of wave length in free space [6, 17]. At frequencies way above the resonance frequency, such as tens of GHz, the ACS is dominated by the body surface area due to the high loss of

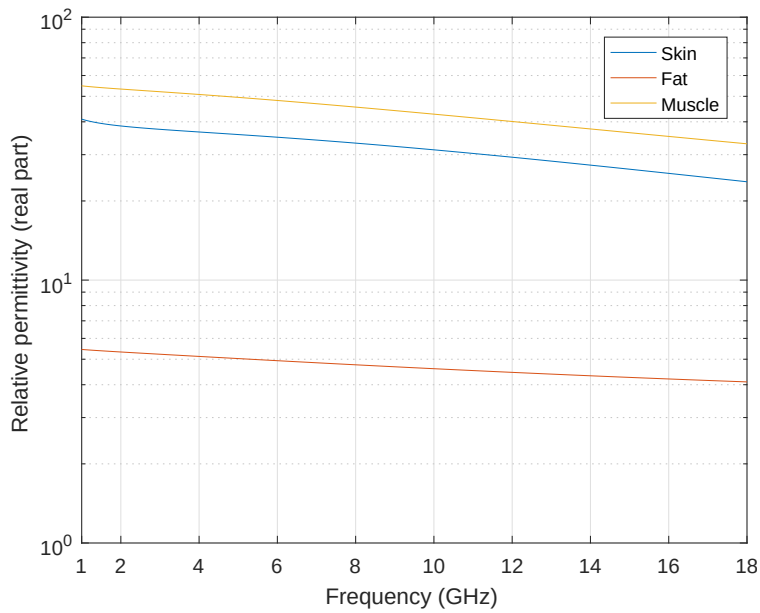


Figure 2.1: The real part of permittivity of three major tissues at the surface of human body [28]

skin[34, 3]. But at frequencies between these two bands, fast and accurate modelling of ACS from morphological parameters can be hard since the ACS is close related to both of shape and superficial layer structure of human body. Previous researches suggested using layered planar, cylindrical and spherical model to model the ACS of humna body [35, 36, 37]. The layer models were usually consisted of three layers which are skin, fat, and muscle. The real and imaginary part of the permittivity of skin, fat and muscle are compared in Fig. 2.1 and Fig. 2.2.

Fig.2.1 and Fig.2.2 show that the magnitudes of both the real part and imaginary part of fat's permittivity are smaller than those of muscle and skin from 1 GHz to 18 GHz, which implies the characteristic impedance of fat is closer to the characteristic impedance of free space. Therefore fat is less reflective than muscle if a plane wave is incident perpendicularly from free space onto its surface. The transmission coefficient of three different tissues

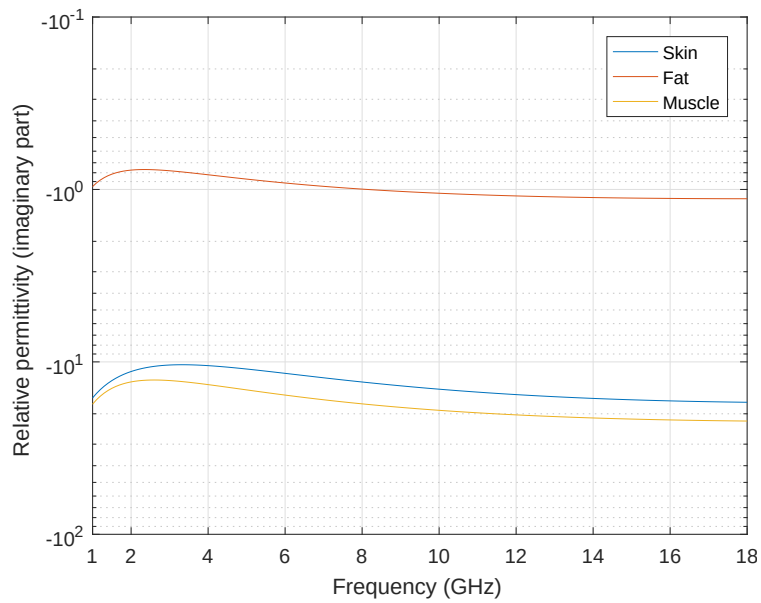


Figure 2.2: The imaginary part of permittivity of three major tissues at the surface of human body [28]

can be calculated by:

$$T = \frac{2Z}{Z + Z_0} = \frac{2\sqrt{\epsilon_0}}{\sqrt{\epsilon_0} + \sqrt{\epsilon}} \tag{2.7}$$

where $T$ is the transmission coefficient; $Z_0, Z$ are the characteristic impedances of free space and tissues; $\epsilon_0$ is the permittivity of free space; $\epsilon$ is the permittivity of tissues. The transmission coefficients of the three tissues are plotted in Fig. 2.3, which shows fat have much higher transmission coefficient than skin and muscle:

The penetration depth of the three tissues were also calculated by (2.3) and plotted in Fig. 2.4.

It can be seen that the penetration depths of all three tissues are lower than 5 cm above 5 GHz, which suggests the surface layer structure at the most superficial 5 cm of human body may dominate the ACS at this frequency

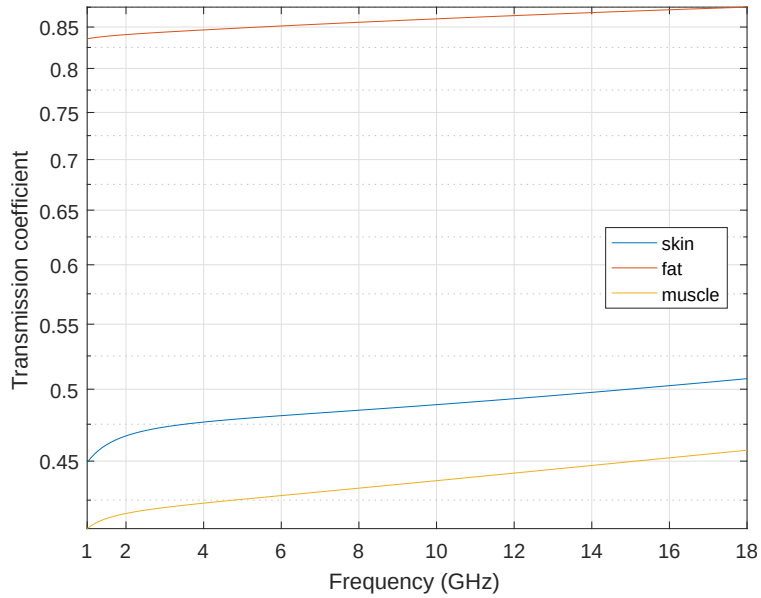


Figure 2.3: Transmission coefficient of three different tissues

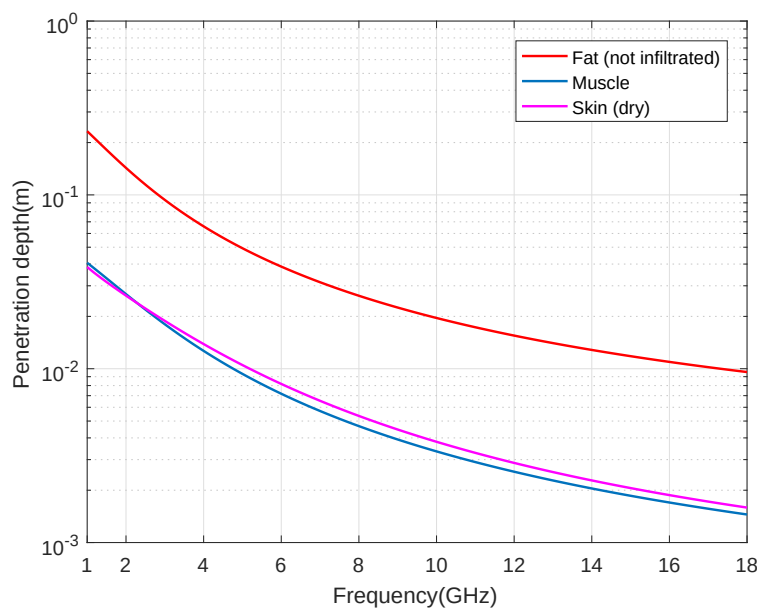


Figure 2.4: The penetration depth of three different tissues

range. Considering the human body is not homogeneous, the power loss in human body can not simply modelled by the transmission coefficient and penetration depth. A multilayer model is required to calculate the EM power dissipation in human body.

One famous study was conducted by Massoudi who did an analytical study on the cylindrical skin-fat-muscle model [37]. He reported the WBSAR of a three-layer cylinder model (skin layer is 0.2 cm, fat layer is 1 cm, radius is 10.08 cm) is 102% higher at 1.2 GHz and 55% smaller at 4.5 GHz than the homogeneous muscle cylinder model when the TM wave (the E-field parallel to the cylinder axis) is incident to the cylinder. In the TE case (the H-field parallel to the cylinder axis), the WBSAR of the three-layer cylinder is 53% higher at 1.3 GHz and 58% less at 4.5 GHz than the homogeneous muscle cylinder. Massoudi also gave a graph of resonance frequency versus fat layer thickness. Then Massoudi used a multi-cylinder model to evaluate the WBSAR of human body. The SAR of the multi-cylinder model is calculated by averaging the SARs of 52 different cylinders. Each cylinder represents a specific part of human body, and the structure of this particular cylinder is determined from the cross section of the body part it represented. For instance, the arms of the man are represented by eight short different cylinders, and each one of the eight cylinders have its own combinations of layers thickness. The multi-cylinder model still shows an increase of WBSAR at 1 GHz and a decrease of WBSAR at 5 GHz. Massoudi also studied the effect of dry cloth on WBSAR. He suggests the effect of dry clothes on the WBSAR is almost neglectable. Similar conclusions on dry clothes had also been made by Barber [35].

To clearly explain the mechanism of absorption, the planar model have been rebuilt in this thesis. The human body tissue is divided into three layers, namely skin, fat and muscle. The thickness of skin is assumed to be 2 mm. A plane wave is incident from the left to the right, as shown in Fig. 2.6. Since there is no active sources presented in the tissues, the E-field and

H-field should be continuous at the boundary of each layer. Then it comes the following six equations:

$$\begin{cases} E_{\text{inc}} + E_{\text{ref}} & = E_{1,\text{i}} + E_{1,\text{r}} \\ \frac{k_0}{\omega\mu_0} E_{\text{inc}} - \frac{k_0}{\omega\mu_0} E_{\text{ref}} & = \frac{k_1}{\omega\mu_0} E_{1,\text{i}} - \frac{k_1}{\omega\mu_0} E_{1,\text{r}} \\ E_{1,\text{i}} \exp(-jk_1x_1) + E_{1,\text{r}} \exp(jk_1x_1) & = E_{2,\text{i}} \exp(-jk_2x_1) + E_{2,\text{r}} \exp(jk_2x_1) \\ \frac{k_1}{\omega\mu_0} E_{1,\text{i}} \exp(-jk_1x_1) - \frac{k_1}{\omega\mu_0} E_{1,\text{r}} \exp(jk_1x_1) & = \frac{k_2}{\omega\mu_0} E_{2,\text{i}} \exp(-jk_2x_1) - \frac{k_2}{\omega\mu_0} E_{2,\text{r}} \exp(jk_2x_1) \\ E_{2,\text{i}} \exp(-jk_2x_2) + E_{2,\text{r}} \exp(jk_2x_2) & = E_{3,\text{i}} \exp(-jk_3x_2) \\ \frac{k_2}{\omega\mu_0} E_{2,\text{i}} \exp(-jk_2x_2) - \frac{k_2}{\omega\mu_0} E_{2,\text{r}} \exp(jk_2x_2) & = \frac{k_3}{\omega\mu_0} E_{3,\text{i}} \exp(-jk_3x_2) \end{cases} \tag{2.8}$$

where $E_{\text{inc}}$ is the strength of incident E-field in free space; $E_{\text{ref}}$ is the strength of reflected E-field in free space; $E_{n,i}$ $\{n = 1, 2, 3\}$ is the strength of E-field propagating inward in the $n$th layer of tissue; $E_{n,r}$ $\{n = 1, 2\}$ is the strength of E-field propagating outward in the $n$th layer of tissue; $k_n = \omega\sqrt{\epsilon_n\mu_0}$ is the complex wave number and $\epsilon_n$ is the complex permittivity of the $n$th layer of tissue. The permeability of each layer of tissue were chosen as $\mu_0$ which is equal to the permeability of free space because the tissues are non-ferrite materials. The definition of the symbols were illustrated in Fig. 2.6.

The value of $E_{\text{ref}}$ can be obtained by solving (2.8), then the absorption coefficient of the planar model can be calculated by the following equation:

$$\xi_{\text{plane}} = \frac{< \sigma_a >}{S_{\text{silhouette}}} \tag{2.9}$$

where $\xi_{\text{plane}}$ is the absorption coefficient of the planar model, $S_{\text{silhouette}}$ denotes the silhouette area of the absorbing object. Equation (2.9) is a generalized definition of $\xi$, so that it can be applied to absorbing objects with different shapes, including human bodies. It can be shown the absorption coefficient of planar model $< \xi_{\text{plane}} >$ is equal to its transmission coefficient. Let the planar model incident by a plane wave, then the EM power going through a surface area of the model equals to the multiplication of transmission coefficient,

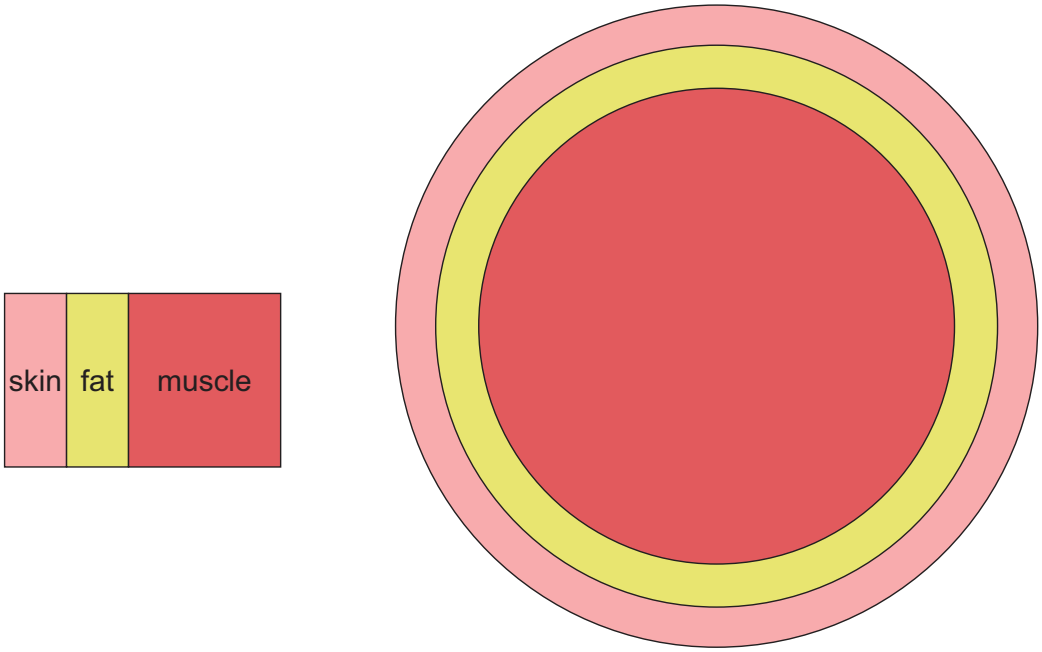


Figure 2.5: The multilayer ACS model

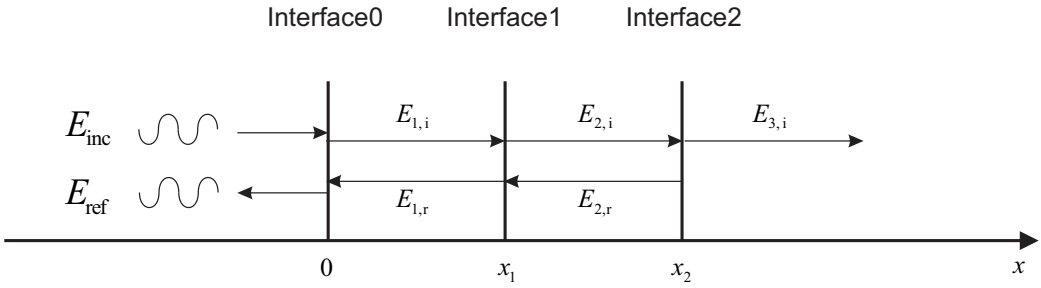


Figure 2.6: The multi-reflection in each layer of planar model

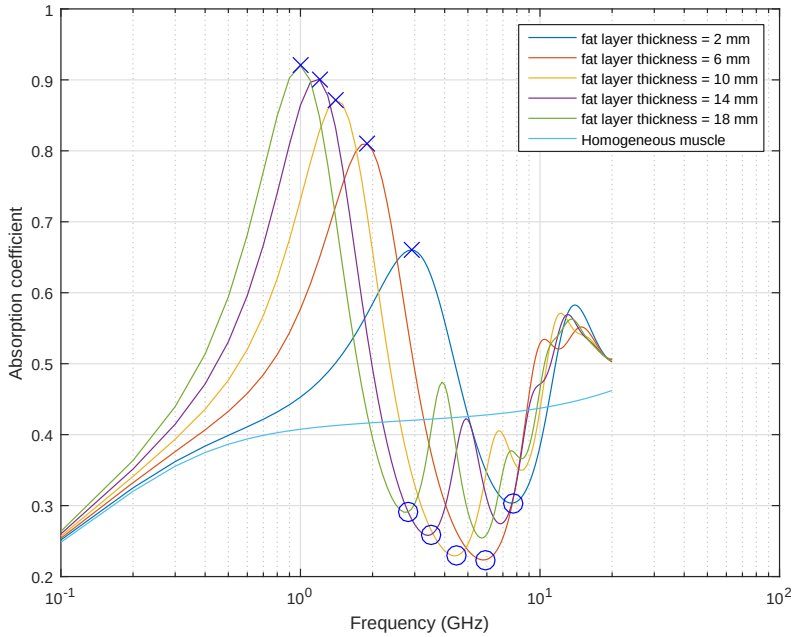


Figure 2.7: The absorption coefficient of planar model with different fat layer thickness (2 mm skin layer thickness)

surface area, and the power flux of the incident plane wave:

$$P_{\text{d,plane}} = |\vec{S}| A_{\text{plane}} T \tag{2.10}$$

where $P_{\text{d,plane}}$ is the power dissipates in the planar model; $\vec{S}$ is Poynting vector; $A_{\text{plane}}$ is an arbitrary area on the model's surface; $T$ is the transmission coefficient of the model. Considering the definition of ACS given in (1.4), it can be shown the $\xi_{\text{plane}}$ is equal to the $T$ by assuming the $A_{\text{plane}} = S_{\text{silhouette}}$:

$$\xi = \frac{\sigma_a}{S_{\text{silhouette}}} = \frac{\sigma_a}{A_{\text{plane}}} = \frac{P_{\text{d,plane}}}{|\vec{S}| A_{\text{plane}}} = T \tag{2.11}$$

The $\xi$ of multilayer planar model with different fat layer thickness were plotted in Fig. 2.7.

A conclusion similar to Massoudi's can be generalized from Fig. 2.7 [37].

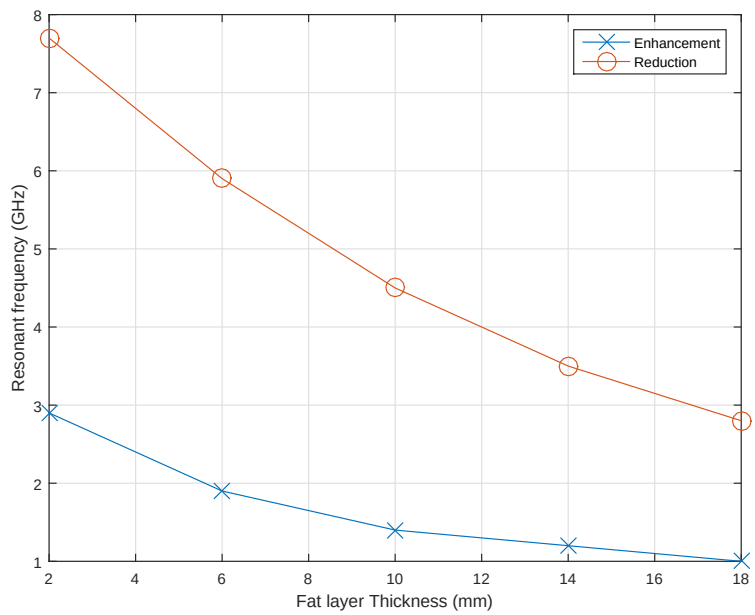


Figure 2.8: Resonant frequencies of planar model, skin layer thickness = 2 mm

When the fat layer is 10 mm thick, the $\xi$ is 110% higher than the $\xi$ of homogeneous model at 1.4 GHz (the value in Massoudi's research is 102% higher at 1.2 GHz), and we call this frequency point as the 'enhancement point', which is defined as the local maximum point of $\xi$ whose frequency is closest to 1 GHz; In the same case, the $\xi$ is 46 % lower at 4.4 GHz (the value in Massoudi's research is 55% lower at 4.5 GHz), and we call this point as 'reduction point', which is defined as the local minimum point of $\xi$ that is closest to 1 GHz. The enhancement points of cylinder models with different fat layer thickness are marked by '$\times$' in Fig. 2.7, and so do the reduction points by '$\circ$'. Fig.2.8 plots the frequencies of enhancement points and reduction points against different fat layer thickness, which shows the their frequencies all decrease as the fat layer thickness increases. The resonant feature of planar model in Fig. 2.7 implies the fat layer may act as a matching layer between skin and muscle. Considering the fat itself is also a

lossy media, more calculation is needed to determine whether the lossy effect dominates the overall absorption, or the matching effect.

Here the percentage of power dissipated in each layer of tissue is calculated. The effective value of EM power dissipated is each tissue layer can be calculated by:

$$P_{\mathrm{d,i}} = \int_{V_i} \frac{1}{2}\sigma_i |\vec{E}|^2 \mathrm{d}V \tag{2.12}$$

where $P_{\mathbf{d,i}}$ is the power dissipated in $i$th layer; $\sigma_i$ is the conductivity of $i$th layer; $|\vec{E}|$ is the magnitude of E-field strength at a particular position; $V_i$ is the volume of i$th$ layer with a constant interface area. The percentage of $P_{\mathrm{d,i}}$ in the total power loss $P_{\mathrm{d}}$ calculated by:

$$\alpha_i = \frac{P_{\mathrm{d,i}}}{P_{\mathrm{d}}} \times 100\% \tag{2.13}$$

The $\alpha_i$ in each tissue layer is plotted from Fig. 2.9 to Fig. 2.12 as the fat layer thickness varies from 2 mm to 14 mm, the skin layer thickness are all 2 mm.

Generally, below 1 GHz, the percentage of power loss in fat is lower than 6% in all the cases. Most of the EM power dissipates in muscle below 1 GHz. Above 5 GHz, the skin starts to absorb more power than any other tissues beneath it, which means the body surface area (BSA) would be the factor dominating ACS. In the cases of fat layer equals to 2 mm, 6 mm and 10 mm, the power dissipated in fat layer is always smaller than the power disspated in skin and muscle from 1 GHz to 18 GHz, which means the power losses in fat was not being able to dominate the whole absorption. In the case of 14 mm fat layer thickness, the power loss in fat only exceed skins at 4 GHz. Similar result on the distribution of power in each layer can be found in the work of Yu who did the calculation on the full scale human phantom [15]. Yu's result shows the skin absorbs the similar amount of power as muscle and fat do at 3 GHz. At frequencies higher than 3 GHz, the skin absorbs

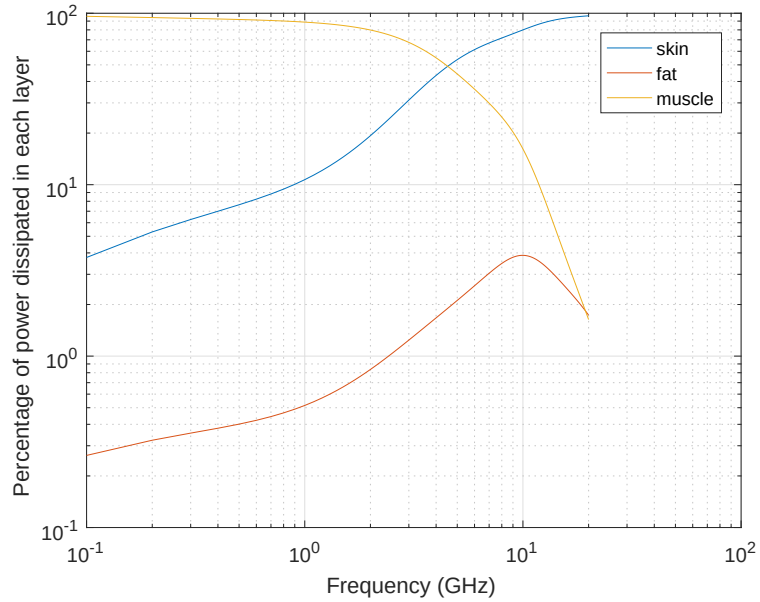


Figure 2.9: Percentage of power loss in each layer of multi-layer planar model: 2mm fat layer thickness

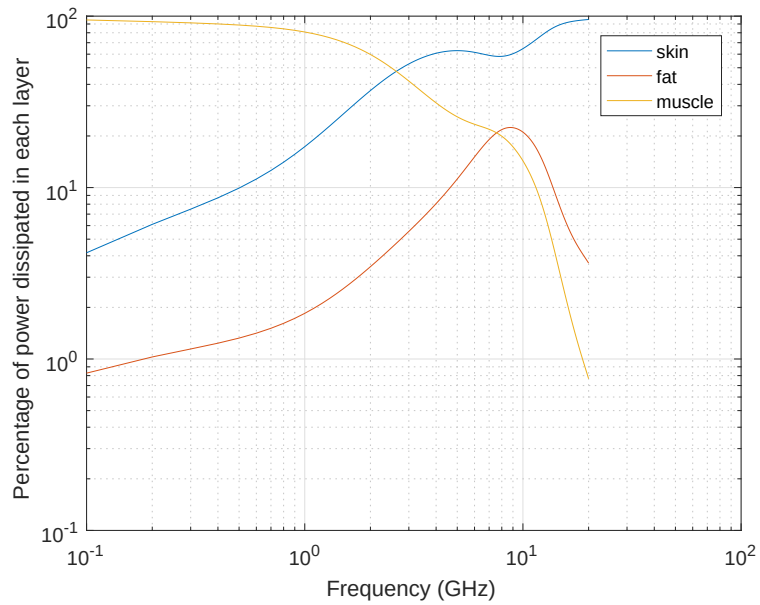


Figure 2.10: Percentage of power loss in each layer of multi-layer planar model: 6mm fat layer thickness

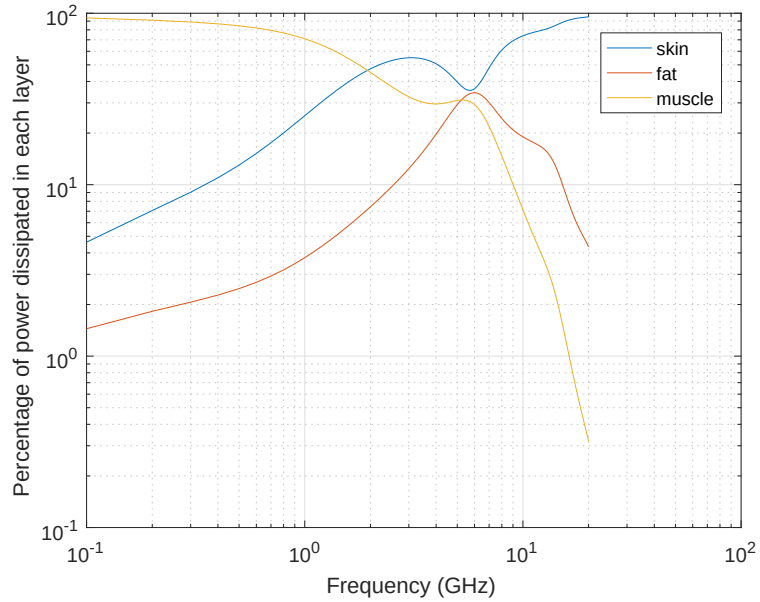


Figure 2.11: Percentage of power loss in each layer of multi-layer planar model: 10mm fat layer thickness

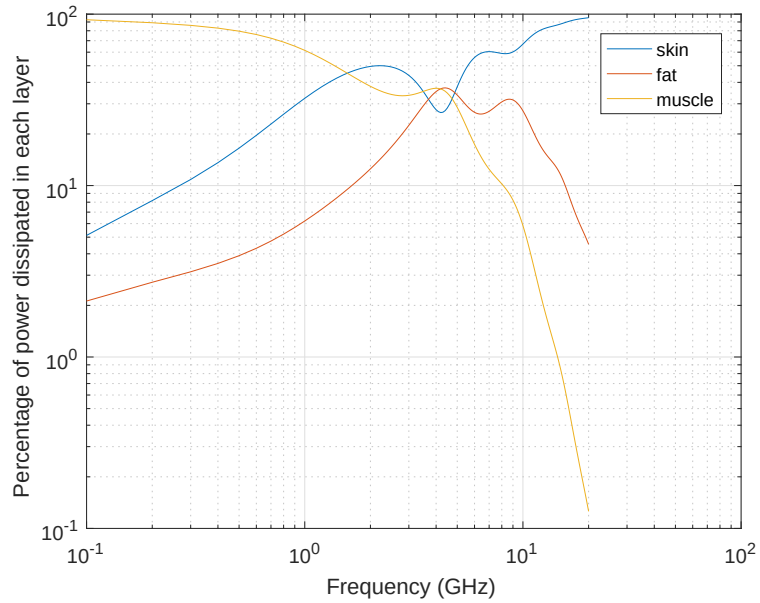


Figure 2.12: Percentage of power loss in each layer of multi-layer planar model: 14mm fat layer thickness

the most. Because of the low percentage of power loss in the fat layer at GHz level, it is reasonable to guess the matching effect of fat dominates the overall ACS of human body.

## 2.3 The Spherical ACS model of human body

One disadvantage of multi-layer planar model is the human body surface curvature was not taken into account. A multi-layer spherical model would be better in modelling the human body surface curvature than the planar model. When the sphere radius is over 10% of the wavelength of the incident wave, the Rayleigh scattering start to lose its accuracy and the Mie series should be applied to calculate the scattering properties of the sphere. Developed by Gustav Mie, the Mie series use spherical harmonics to solve the sphere scattering problem. The relatively easy derivation can be found in Harrington's book [38]. The software package of calculating Mie series applied in this thesis is SPlaC V1.0 [39].

Assuming the skin layer thickness of the sphere model is 2 mm; the circumference of the multilayer sphere is 90 cm which similar to the size of human waist; Fig. 2.13 demonstrated the sphere model's absorption coefficient which is defined as the ratio of sphere ACS to the silhouette area of the sphere model:

$$< \xi_{a,\text{sphere}} >= \frac{< \sigma_{a,\text{sphere}} >}{S_{\text{sphere}}} \tag{2.14}$$

where $< \xi_{a,\text{sphere}} >$ is the absorption coefficient of the sphere; $< \sigma_{a,\text{sphere}} >$ is the ACS of the sphere; $S_{\text{sphere}}$ is the silhouette area of the sphere, which is also equal to the maximum cross section area of the sphere.

Comparing to the absorption coefficient of planar model demonstrated in Fig. 2.7, the resonance behaviour of the sphere model is very similar. The resonant frequencies of the spherical model go low as the fat layer thickness

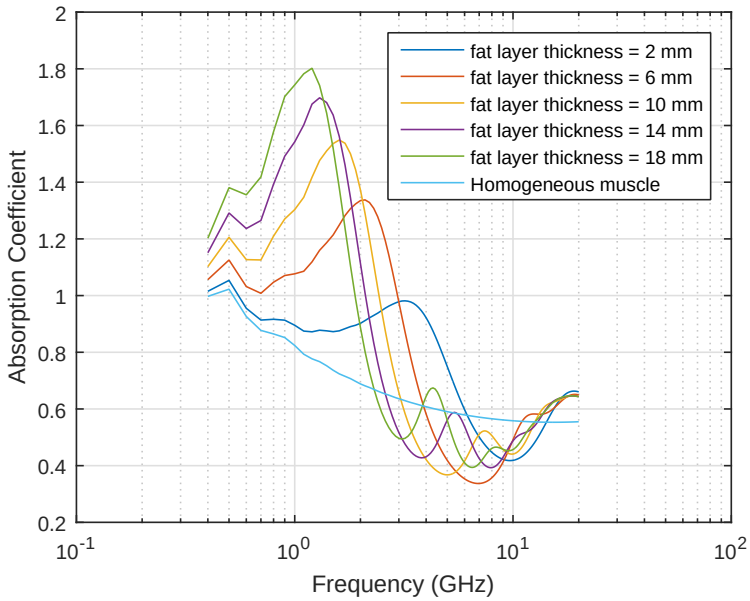


Figure 2.13: The absorption coefficient of the multi-layer spherical model

goes high. But the spherical model tend to have a much higher absorption coefficient at 1 GHz than the planar model.

## 2.4 Measurement of human body ACS in the RC

As stated before, the large population study on the human body ACSs is hard to achieve by full wave numerical methods, especially at high frequencies. Thus we use the reverberation chamber (RC) to do the population study over a wide band of frequency. It is important to point out that the ACS measured in the RC is different from the the ACS acquired by FDTD calculation. The ACS measured in the RC is the ACS averaged over different directions, which

is [40]:

$$< \sigma_a >= \frac{1}{4\pi}\int_0^{\pi}\int_0^{2\pi}\sigma_a(\theta,\phi)\sin\theta \mathrm{d}\theta\mathrm{d}\phi \approx \frac{\frac{1}{4\pi}\int_0^{\pi}\int_0^{2\pi}P_d(\theta,\phi)\sin\theta\mathrm{d}\theta\mathrm{d}\phi}{\frac{1}{4\pi}\int_0^{\pi}\int_0^{2\pi}S(\theta,\phi)\sin\theta\mathrm{d}\theta\mathrm{d}\phi} = \frac{< P_d >}{< S >} \quad (2.15)$$

where $< \sigma_a >$ means averaged ACS; $< P_d >$ means $P_d(\theta,\phi)$ averaged over different directions; $< S_d >$ means $S_d(\theta,\phi)$ averaged over different directions. The angle bracket symbol $< \cdot >$ means averaging. Our research covers the human body ACS measurement from 1 GHz up to 18 GHz which is the operation frequency range of the available measurement system.

The RC is a cavity loaded with a moving stirrer which creates a stochastic field configuration inside. The power losses in an object loaded in the RC can be obtained by the power balance model since the RC is a enclosed environment. According to Hill's theory, the stochastic field in RC can be expanded into a series of plane wave coming from all directions, therefore the ACS measured in the RC is the averaged ACS as given by (2.15) [40].

The averaged ACS $< \sigma_a >$ of all objects in the RC can be obtained from measuring the averaged Quality factor. The averaged Quality (Q) factor is defined by [40, 41]:

$$< Q >= \omega\frac{U}{< P_d >} \quad (2.16)$$

where $U$ is the energy stored in the RC; $\omega$ is the angular frequency; $< P_d >$ is the amount of averaged power loss in the RC. Assume the energy distributed homogeneously in the RC, (2.16) transform into:

$$< Q >= \omega\frac{WV}{< P_d >} \quad (2.17)$$

where $W$ is the energy density in RC; $V$ is the volume of RC. Since the power

flow density and energy density has following relation:

$$W = \frac{< S >}{c} \tag{2.18}$$

where $c$ is the speed of light. Substitute (2.18) into (2.17) gives:

$$< Q >= \omega \frac{< S > V}{c < P_d >} \tag{2.19}$$

And by substituting (2.15) into (2.19) we have:

$$< \sigma_{\mathrm{a}} >= \frac{\omega V}{c < Q >} = \frac{2\pi V}{\lambda < Q >} \tag{2.20}$$

where $\lambda$ is wavelength. The $< \sigma_a >$ obtained by (2.20) includes all the power loss mechanism in the RC. Equation (2.20) shows $< \sigma_a >$ is inversely proportional to $< Q >$. (2.20) also implies the averaged ACS of object under test can be obtained by measuring the averaged Q factor before and after the chamber is loaded, which is:

$$< \sigma_a >= \frac{2\pi V}{\lambda} \left( \frac{1}{< Q_{\mathrm{wo}} >} - \frac{1}{< Q_{\mathrm{no}} >} \right) \tag{2.21}$$

where the subscript 'wo' means with the object loaded in the RC; 'no' means no object loaded in the RC. Therefore accurate measurement of averaged Q factor is very important to the accurate measurement of ACS.

One method of determining averaged Q factor is by measuring the transmission coefficient between the two ports of antennas in the RC [42]:

$$< Q >= \frac{16\pi^2 V}{\lambda^3} G \tag{2.22}$$

where G is the net transfer function which equals to:

$$G = \frac{< |S_{21}|^2 >}{(1 - | < S_{11} > |^2)\,(1 - | < S_{22} > |^2)\,\eta_{\mathrm{Tx}}\eta_{\mathrm{Rx}}} \tag{2.23}$$

where $\eta_{\mathrm{Tx}}$ and $\eta_{\mathrm{Rx}}$ are the radiation coefficients of transmitting antenna and receiving antenna. $S_{mn}$ are the S-parameters measured at the ports of antennas loaded in the RC.

The disadvantage of determining $< Q >$ by this method is obvious, it requires antenna efficiencies to be known. Inaccurate values of antenna radiation efficiencies would deteriorate the accuracy of ACS measurement in the RC.

## 2.5 Determining $< Q >$ of RC by IFFT

Considering the Q factor is related to the speed of power loss as given in (2.16), $< Q >$ can be defined by another variable, namely chamber time constant $\tau$ [40, 43]:

$$< Q >= \omega\tau \tag{2.24}$$

$\tau$ is defined as the time for a RC to lose its stored energy to $\frac{1}{e} \times 100\%$ of its initial value. Equation (2.24) is derived from an ordinary differential equation which gives the speed of power loss in the RC. By assuming the EM energy is homogeneously distributed in the RC, the power loss speed should be proportional to the energy stored, therefore we have [40]:

$$< P_{\mathrm{d}} >= \frac{\mathrm{d}U}{\mathrm{d}t} = -\frac{U}{\tau} \tag{2.25}$$

where $|\tau| = \frac{U}{<P_d>}$. Solving (2.25) gives:

$$U = A\exp(-\frac{t}{\tau}) \tag{2.26}$$

where $A$ is a constant indicating the signal strength. (2.26) shows $U = A$ when $t = 0$; $U = A/e$ when $t = \tau$ which corresponds with the definition of chamber time constant $\tau$. $\tau$ can be obtained from the channel impulse response (CIR) in the RC. The CIR is obtained by inverse Fourier transforming (IFFT) the $S_{21}$ measured in the RC. According to Richardson's research, the CIR in a RC can be modelled as a summation of infinite sinusoidal signals with independent frequency and phase shift multiplied by a factor which decays exponentially [44]:

$$h(t) = \sum_i a_i \sin(\omega_i t + \theta_i) e^{-t/2\tau_i} \tag{2.27}$$

where $h(t)$ denotes CIR; $i$ is the index of each path; $a_i$ is the magnitude of each path; $\omega_i$ is the angular frequency; $\theta_i$ is the phase shift. Equation (2.27) is in fact a form of the Fourier series with random magnitude and phase shift, it is straightforward to assume the sampled CIR $h(t)$ should follow Gaussian random process, therefore the (2.27) can be written as:

$$h(t) = AN(t) \exp(-\frac{t}{2\tau}) \tag{2.28}$$

Where $N(t)$ is a complex Gaussian random process with zero mean and variance of one. This is an important formula since it would help building the non-linear curve fitting model which will be introduced in Sec. 2.8. Equation (2.28) shows the power response of CIR has an exponential form, which corresponds with (2.26). The power response of CIR is defined as the power delay profile (PDP) which is obtained form the IFFT of windowed $S_{21}$:

$$\text{PDP}(t) =< |h(t)|^2 >=< |\text{IFFT}\,(S_{21}(f) \cdot W(f))\,|^2 > \tag{2.29}$$

where $W(f)$ is the window function in frequency domain. Here as an example, the PDP at 10 GHz measured at one stirrer position in an RC is plotted in

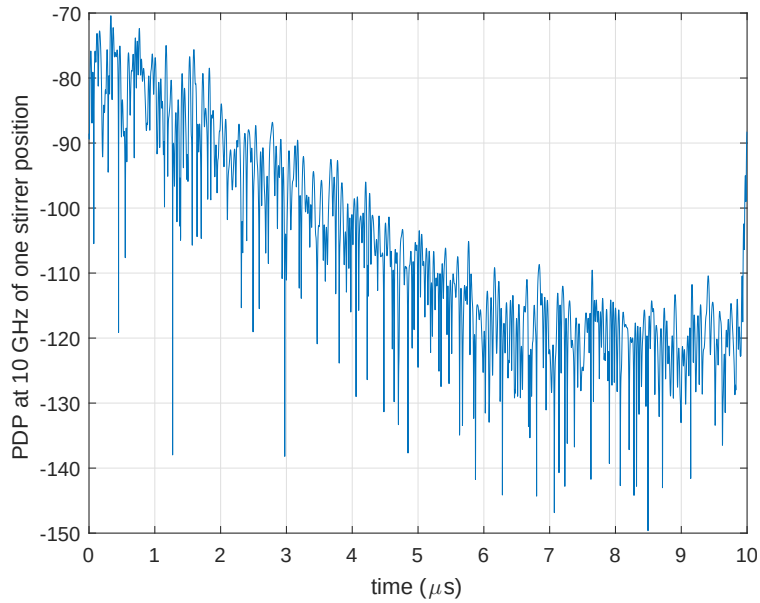


Figure 2.14: The measured PDP at one stirrer position in the RC

Fig. 2.14. The chamber time constant can be extracted from the slope of PDP in Fig. 2.14, but the accuracy of extracted chamber time constant would be low due to the high variance of PDP. Such variance can be reduced by averaging the PDP measured at different stirrer positions. The PDP averaged over 200 stirrer positions were demonstrated in Fig. 2.15. Comparing to the PDP in Fig. 2.14, the averaged PDP is much smoother. The chamber time constant can be extracted from the PDP in Fig. 2.15 with better accuracy than it does from the PDP in Fig. 2.14.

## 2.6 Advantages of determining averaged Q factor by IFFT

Comparing to determining chamber $< Q >$ by the G factor given in (2.22), the biggest advantage of determining Q by IFFT is the IFFT method is not

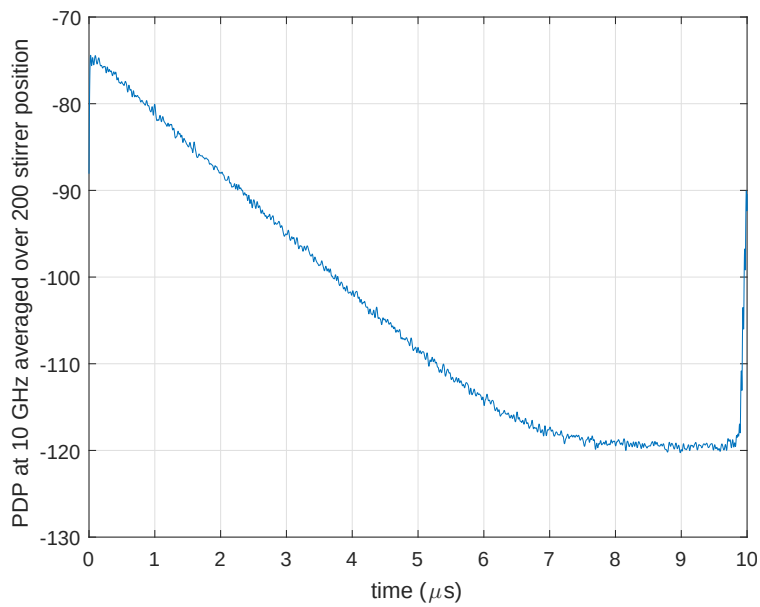


Figure 2.15: The measured PDP averaged over 200 stirrer positions in the RC

sensitive to antenna efficiency. The explanation is given as follow.

With respect ot Hill's research, the power loss in an RC can be broken down into four parts [41]:

$$< P_d >=< P_{d1} > + < P_{d2} > + < P_{d3} > + < P_{d4} > \tag{2.30}$$

where $< P_{d1} >$ is the power loss on RC walls; $< P_{d2} >$ is the power absorbed by loading objects; $< P_{d3} >$ is the power loss through aperture; $< P_{d4} >$ is the power loss on loaded antennas. Remembering the assumption that energy is distributed homogeneously in the RC, divide both sides of (2.30) by $U$ and then multiply with $\omega$ gives:

$$< Q >^{-1}=< Q_1 >^{-1} + < Q_2 >^{-1} + < Q_3 >^{-1} + < Q_4 >^{-1} \tag{2.31}$$

where $< Q >$ is the overall Q factor in the RC; $< Q_i >$ $(i \in [1, 4] \,\text{and}\, i \in N)$

are the averaged Q factors contributed by particular way of power loss. (2.31) shows the $< Q >$ of the RC is dominated by the biggest $< Q_i >^{-1}$. $< Q_4 >^{-1}$, which is determined by the power loss on the antenna, is usually the smallest one, therefore $< Q >$ is not sensitive to $< Q_4 >^{-1}$. Since the overall Q factor $< Q >$ can be accurately determined by the PDP, the insensitivity of $< Q >$ to $< Q_4 >$ has also been used in the determination of antenna efficiency by substituting $< Q >$ into (2.22) [45]. Such $< Q >$ obtained by IFFT can also be used to calculate the ACS using (2.21) [46, 40, 47].

## 2.7 Extracting chamber time constant by linear curve fitting and its inaccuracy

Since PDP is defined as the power response of $h(t)$ as given in (2.29), the explicit expression of PDP should follow

$$\mathrm{PDP}(t) = A^2 e^{-\frac{t}{\tau}} \tag{2.32}$$

In the logarithmic scale, the PDP should be a straight line because

$$\begin{aligned} \mathrm{PDP}(t)_{\mathrm{dB}} &= 10 \log_{10} \left( A^2 e^{-\frac{t}{\tau}} \right) \\ &= 20 \log_{10} (A) - \frac{10 \log_{10}(e)}{\tau} t \end{aligned} \tag{2.33}$$

And the PDP slope, which is the coefficient of $t$, gives the value of the chamber time constant $\tau$. The slope of PDP can be determined from linear curve fitting. But applying linear curve fitting on the PDP has following problems.

Firstly, a proper fitting range should be chosen. As can be seen from Fig. 2.15, the measured PDP is not a straight line but a combination of a decline

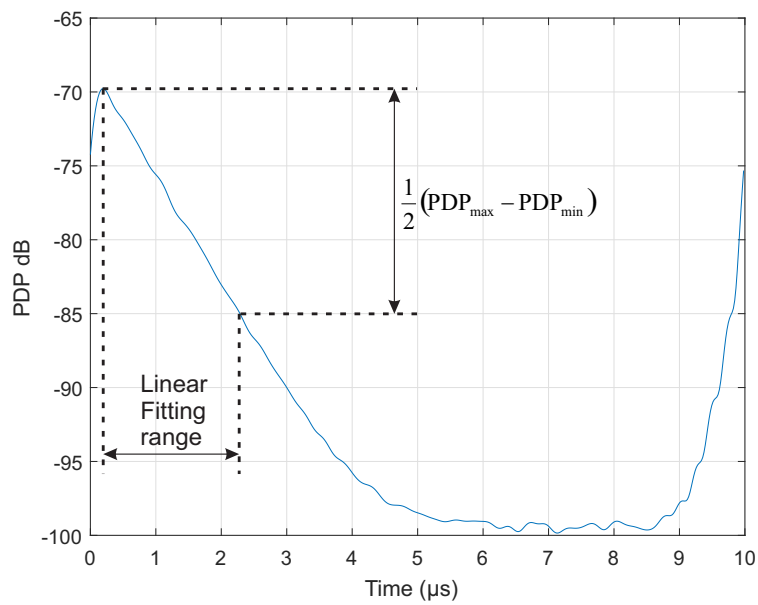


Figure 2.16: The linear fitting range is selected as the top half of PDP

slope and a flat noise floor, which is:

$$\mathrm{PDP}_{\mathrm{dB,noise}}(t) = 10\log_{10}\left(A^2 e^{-\frac{t}{\tau}} + B^2\right) \tag{2.34}$$

where $B$ is a coefficient which determines the level of noise floor. If the fitting range includes noise floor, the linear curve fitting would produce wrong results. A way of solving this problem is to choose a fitting range that gives the top 30 dB of PDP [48]:

$$\{t_{\mathrm{fit}}\} = \left\{t \middle| \max[\mathrm{PDP}_{\mathrm{dB}}(t)] - \mathrm{PDP}_{\mathrm{dB}}(t) < 30\mathrm{dB}\right\} \tag{2.35}$$

where $\{t_{\mathrm{fit}}\}$ denotes the fitting range. However, this method will not work in low signal noise ration (SNR) cases. Therefore in our research, the linear fitting range is chosen dynamically as the time range that gives the top half of PDP, as shown in Fig. 2.16.

Secondly, the linear curve fitting will not give the correct chamber time constant no matter which linear fitting range is selected. This problem can be demonstrated by calculating the derivative of the PDP respect to $t$ in logarithmic scale:

$$\frac{\mathrm{dPDP}_{\mathrm{dB,noise}}(t)}{\mathrm{d}(t)} = \left(-\frac{10\log_{10} e}{\tau}\right)\frac{\mathrm{SNR}e^{-\frac{t}{\tau}}}{\mathrm{SNR}e^{-\frac{t}{\tau}}+1} \tag{2.36}$$

where $\mathrm{SNR} = \frac{A^2}{B^2}$. Since the fitting range is always chosen close to $t = 0$ to give a better linearity of the PDP, substituting $t = 0$ into (2.36) gives:

$$\left.\frac{\mathrm{dPDP}_{\mathrm{dB,noise}}(t)}{\mathrm{d}(t)}\right|_{t=0} = \left(-\frac{10\log_{10} e}{\tau}\right)\frac{\mathrm{SNR}}{\mathrm{SNR}+1} \tag{2.37}$$

As it shown by (2.37), the derivative of PDP is affected by SNR. If SNR is a very large value, $\mathrm{SNR}/(\mathrm{SNR}+1)$ would be approximate to 1, thus the derivative of PDP would be equal to the term in the bracket of (2.37). This term is equal to the coefficient of $t$ in (2.33) which is the linear model of the PDP without noise floor. But if SNR is a small value then the derivative of the PDP would be dominated by the value of $\mathrm{SNR}/(\mathrm{SNR}+1)$. All these facts show extracting time constant by linear fitting is not accurate.

Thirdly, the window function can change the shape of PDP, which would eventually change the output of linear curve fitting. Since chamber time constant is a frequency dependent variable, the $S_{21}$ used to calculate PDP should be windowed at a particular frequency before calculating the IFFT. The window function's effect on the PDP is shown in Fig. 2.17. Three different window functions with different window widths were applied to the same $S_{21}$ to extract PDP. The central frequencies of all three windows were all at 15 GHz and they are all raised-cosine windows with rolling off factor $\beta = 0.25$ [50]. The lower graph of Fig. 2.17 shows the application of different

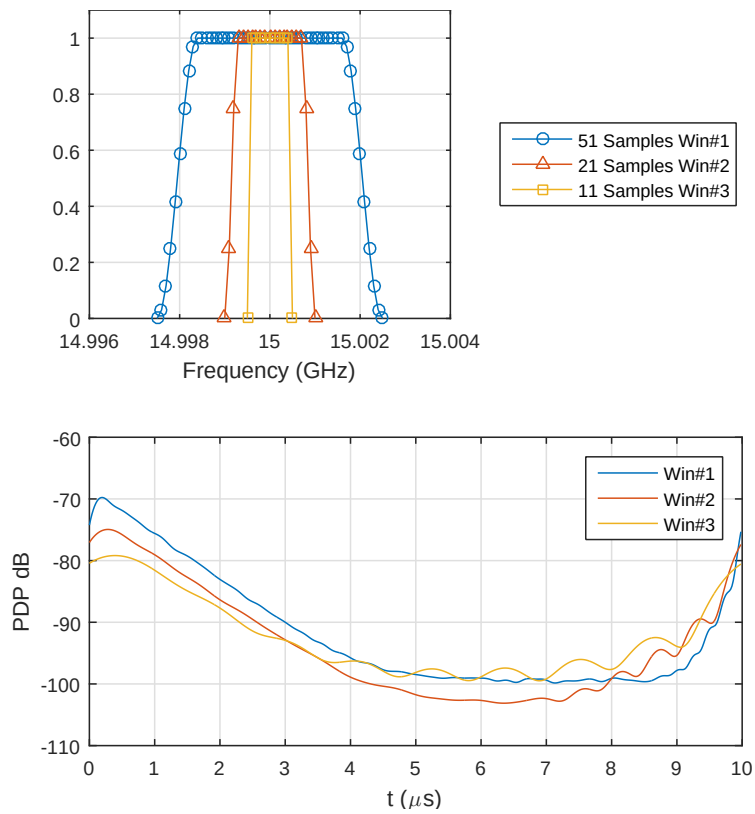


Figure 2.17: PDP extracted by applying different window functions at 15 GHz. Win #1: total width 5 MHz, 100 kHz frequency step, 51 samples; Win #2: total width 2 MHz, 100 kHz frequency step, 21 samples; Win #3: total width 1 MHz, 100 kHz frequency step, 11 samples. The filtered $S_{21}$ were all padded to zero frequency to show the ringing effect of piecewise window functions in full detail, because adding more zeros to the discrete spectrum of $S_{21}$ in frequency domain is equivalent to increasing the resolution of signal in time domain [49].

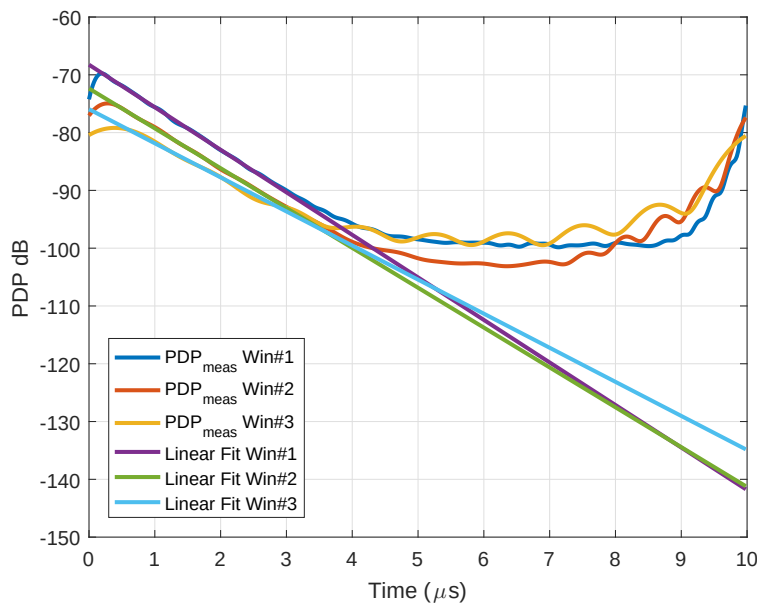


Figure 2.18: Linear curve fitting results of different PDP extracted by applying different window functions

window function gives very different PDP. If the linear fitting range is chosen in a way demonstrated in Fig. 2.16, the fitted straight lines are plotted in Fig. 2.18 Even though the three window functions share the same central frequency, the linear curve fitting results at this particular frequency are different. Since the chamber time constant is a property of RC, it should not change with different data processing method. Therefore the results given by linear curve fitting is unacceptable.

## 2.8 The nonlinear curve fitting

To address the three problems of linear curve fitting, the nonlinear curve fitting is introduced.

In terms of the model of CIR given in (2.28) and the PDP we observed

from measurement, the full statistical model of the PDP is:

$$h(t) = AN_1(t)\exp(-\frac{t}{2\tau}) + N_2(t) \tag{2.38}$$

written in a discrete form, (2.38) should be equal to:

$$h(n) = AN_1(n)\exp(-\frac{n\Delta t}{2\tau}) + BN_2(n) \tag{2.39}$$

where $\Delta t$ is the time step size. $N_1(t)$ and $N_2(t)$ are complex Gaussian process [51], with zero mean and a standard deviation of 1. $A$ and $B$ controls the levels of signal and noise floor.

Equation (2.39) shows the distribution of $h(n)$ at a particular moment $n_0$ should have the Gaussian distribution. Here as an example, the Quantile-Quantile plot is applied on a group of measured $h(n_0)$ to test whether the $h(n_0)$ follows the Gaussian distribution, as shown in Fig. 2.19 and Fig. 2.20[52]. The plotted of $h(n_0)$ was obtained from the IFFT of $S_{21}$ windowed at 10 GHz, $n_0\Delta\, t$ is equal to $5\,\mu s$.

Both the real part and the imaginary part of $h(n_0)$ are distributed closely to the reference line, which means the real part and imaginary part of $h(n_0)$ follow the Gaussian distribution.

The CIR model (2.39) is not complete since it does not include the effect of window function. Since the CIR is obtained from the IFFT of windowed $S_{21}$, the CIR in time domain should have the following relation to $S_{21}$ in frequency domain according to the convolution theorem [53]:

$$h(n) \otimes w(n) \overset{\text{FFT}}{\longleftrightarrow} S_{21}(n_f)W(n_f) \tag{2.40}$$

where $w(n)$ and $W(n_f)$ are the response of window function in time domain (TD) and frequency domain (FD). $n$ and $n_f$ are the indexes of samples in time domain and frequency domain, respectively. $S_{21}(n_f)W(n_f)$ denotes

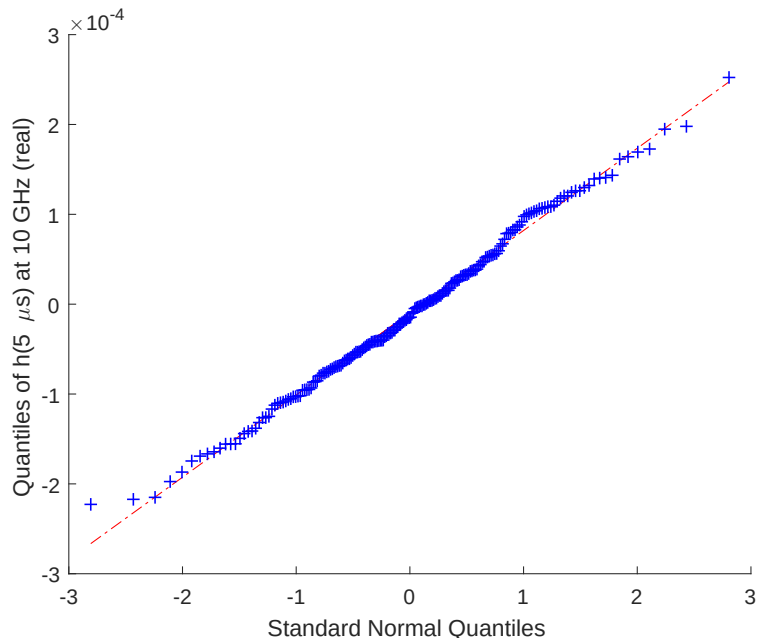


Figure 2.19: The Quantile-Quantile plot of the real part of CIR h($n_0\Delta t$) where $n_0\Delta t = 5\mu s$

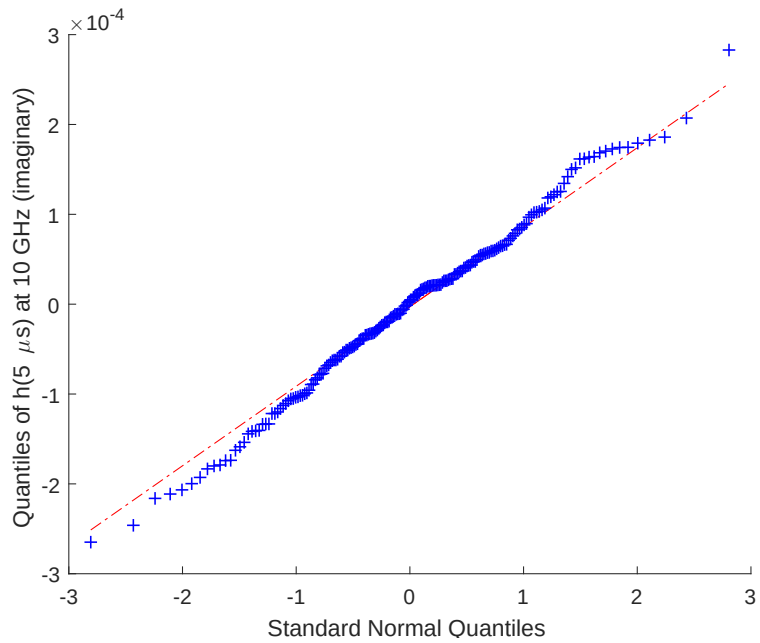


Figure 2.20: The Quantile-Quantile plot of the imaginary part of CIR h(5 $\mu s$)

the windowed $S_{21}$ for IFFT. $\otimes$ means circulated convolution.

Substitute (2.38) into (2.40) gives:

$$AN_1(n)\exp(-\frac{n\Delta t}{\tau}) \otimes w(n) + BN_2(n) \otimes w(n) \overset{\text{FFT}}{\longleftrightarrow} S_{21}(n_f)W(n_f) \quad (2.41)$$

According to the definition of PDP:

$$\text{PDP}(n) \quad = \quad \left\langle \left| AN_1(n)\exp(-\frac{n\Delta t}{2\tau}) \otimes w(n) + BN_2(n) \otimes w(n) \right|^2 \right\rangle \quad (2.42)$$

Expanding the right side of equation:

$$\begin{aligned}\text{PDP}(n) = \left\langle \left| AN_1(n)\exp(-\frac{n\Delta t}{2\tau}) \otimes w(n) \right|^2 \right\rangle + \left\langle |BN_2(n) \otimes w(n)|^2 \right\rangle + \\ \left\langle \overline{AN_1(n)\exp(-\frac{n\Delta t}{2\tau}) \otimes w(n)} \cdot BN_2(n) \otimes w(n) \right\rangle + \\ \left\langle AN_1(n)\exp(-\frac{n\Delta t}{2\tau}) \otimes w(n) \cdot \overline{BN_2(n) \otimes w(n)} \right\rangle \quad (2.43)\end{aligned}$$

Where the over bar $\overline{\alpha}$ denotes complex conjugation of $\alpha$. Because of the independence between $N_1$ and $N_2$, the expectation of the third term and the fourth term on the right side of the equation should be equal to zero. Here we use the symbol $E[\cdot]$ to replace the symbol $< \cdot >$. $E[\cdot]$ means the expected value of average. Therefore the expectation PDP will only include the first two terms.

$$\begin{aligned}\text{PDP}(n) = E\left[ \left| AN_1(n)\exp(-\frac{n\Delta t}{2\tau}) \otimes w(n) \right|^2 \right] + \\ E\left[ |BN_2(n) \otimes w(n)|^2 \right] \quad (2.44)\end{aligned}$$

Both of the first and second term can be simplified. Here we will use the

first term as an example. In terms of the definition of circular convolution, the first term can be written as:

$$E\left[\left|AN_1(n)\exp(-\frac{n\Delta t}{2\tau})\otimes w(n)\right|^2\right] = \\ E\left[\left|\sum_{i=0}^{N-1} AN_1(i)\exp(-\frac{i\Delta t}{2\tau})w(n-i)\right|^2\right] \quad (2.45)$$

The square operation on the right side can be expanded into quadratic form. Because $N_1$ is an Gaussian process, there is :

$$E[N_1(i)N_1(j)] = 0 \quad (i \neq j) \quad i,j \in \mathbb{N} \quad (2.46)$$

Therefore:

$$E\left[\left|\sum_{i=0}^{N-1} AN_1(i)\exp(-\frac{i\Delta t}{2\tau})w(n-i)\right|^2\right] = \\ \sum_{i=0}^{N-1} A^2\exp(-\frac{i\Delta t}{\tau})|w(n-i)|^2 \quad (2.47)$$

$$\mathrm{PDP}(n) = \left[A^2\exp(-\frac{n\Delta t}{\tau})\right]\otimes|w(n)|^2 \quad (2.48)$$

Same operation can be applied on the noise term of (2.44). Equation (2.44) can be written as:

$$\mathrm{PDP}(n) = \left[A^2\exp(-\frac{n\Delta t}{\tau}) + B^2\right]\otimes|w(n)|^2 \quad (2.49)$$

(2.49) is gives the nonlinear model for PDP. The model is controlled by 4 parameters: $A$, $B$, $\tau$, $w$, in which the window function $w(n)$ is known.

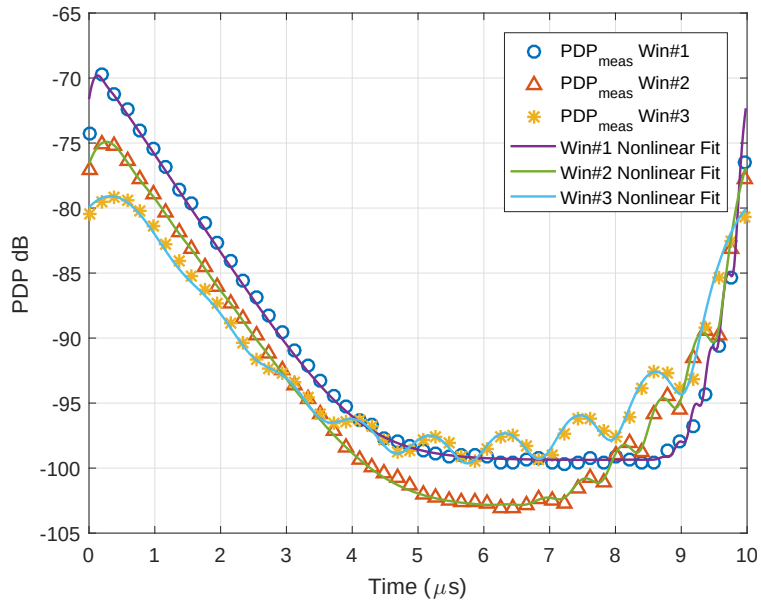


Figure 2.21: the nonlinear model matches well with the PDP

The optimized values of $A$, $B$, $\tau$ can be found by Levenberg-Marquardt method. Similar to the gradient descent method, the Levenberg-Marquardt method is an iteration algorithm which can find the minimum point of the cost function following its gradient, if a starting point and a step size are given. The Levenberg-Marquardt method would adjust its step size after each iteration with respect to its converging speed, which is more superior than the gradient descent method whose step size is a constant [54].

In order to demonstrate the effectiveness of nonlinear curve fitting, the PDP in Fig. 2.18 were all fitted to the nonlinear model. The results were shown in Fig. 2.21. It can be seen all the three PDP match well with the corresponding nonlinear model.

## 2.9 Estimating the starting value for nonlinear curve fitting

The PDP model (2.49) is a mono-exponential decay formula convoluted with window function, and accurate starting values must be given to the Levenberg-Marquardt algorithm for to guarantee the convergence of curve fitting with (2.49). In the practical measurement, we found even though the linear curve fitting was not able to give an accurate chamber time constant, but it is accurate enough to give a starting value for the nonlinear curve fitting. This section will present a method of estimating initial values of $A$, $B, \tau$ by linear curve fitting. The first step is to estimate the starting value of $\tau$. The starting value of $\tau$ was firstly evaluated by linear curve fitting whose fitting range is selected by the method presented in Fig. 2.16 [48].

After the value of $\tau$ has been determined, the next step is to determine the value of $A$. A reference signal with unit signal level was selected to help determining the value of $A$. The reference signal is a exponential function convoluted with the power response of window function in time domain.

$$\mathrm{PDP}_{\mathrm{ref}} = \left[\exp(-\frac{n\Delta t}{\tau_0})\right] \otimes |w(n)|^2 \tag{2.50}$$

where $\tau_0$ is the starting value of chamber time constant estimated in the first step. Comparing to the nonlinear model (2.49), (2.50) has a unit signal strength, therefore the ratio between measured PDP and reference signal should equal to:

$$\frac{\mathrm{PDP}_{\mathrm{meas}}(n)}{\mathrm{PDP}_{\mathrm{ref}}(n_0)} \approx \frac{\left[A^2\exp(-\frac{n\Delta t}{\tau_0}) + B^2\right] \otimes |w(n)|^2}{\left[\exp(-\frac{n\Delta t}{\tau_0})\right] \otimes |w(n)|^2} \tag{2.51}$$

If $B$ is a small value comparing to $A$, at a particular time $n = n_0$, (2.51)

changes into:

$$\frac{\mathrm{PDP}_{\mathrm{meas}}(n_0)}{\mathrm{PDP}_{\mathrm{ref}}(n_0)} \approx \frac{\left[A^2\exp(-\frac{n_0\Delta t}{\tau_0})\right] \otimes |w(n)|^2}{\left[\exp(-\frac{n_0\Delta t}{\tau_0})\right] \otimes |w(n)|^2} \approx A_0^2 \tag{2.52}$$

Here the value of $n_0$ was selected at the time when $\mathrm{PDP}_{\mathrm{meas}}$ reaches its maximum.

The last step is to estimate the starting value of $B$. Since the starting values of $A$ and $\tau$ have been evaluated, the first estimation of PDP can be given:

$$\mathrm{PDP}_{\mathrm{g1}}(n) = \left[A_0^2 \exp\left(-\frac{n\Delta t}{\tau_0}\right)\right] \otimes |w(n)|^2 \tag{2.53}$$

where the subscript g1 means the first estimation; $\mathrm{PDP}_{\mathrm{g1}}$ is a windowed PDP without noise floor. The value of $B$ can be obtained by subtracting the evaluated exponential term from the nonlinear model (2.49):

$$\begin{aligned} &\mathrm{PDP}_{\mathrm{meas}}(n) - \mathrm{PDP}_{\mathrm{g1}}(n) = \\ &\left[A^2\exp(-\frac{n\Delta t}{\tau}) + B^2\right] \otimes |w(n)|^2 - \left[A_0^2\exp(-\frac{n\Delta t}{\tau_0})\right] \otimes |w(n)|^2 \approx B^2[w(n)]^2 \end{aligned} \tag{2.54}$$

$B$ can be evaluated by choosing any value of $n$. In order to achieve a better estimation accuracy of $B$, it is better to select a an $n$ on which the PDP has the lowest SNR, as shown in Fig. 2.22. After the value of B has been determined, the final estimation of PDP can be obtained. Fig. 2.22 also shows the final estimation of the nonlinear PDP model already matches well with the measurement result. The techniques of estimating starting values were applied to the nonlinear curve fitting of PDP from 1 GHz to 18 GHz.

The goodness of the estimation is quantified by the cost function, which is the RMS difference between measured PDP in dB and estimated PDP in

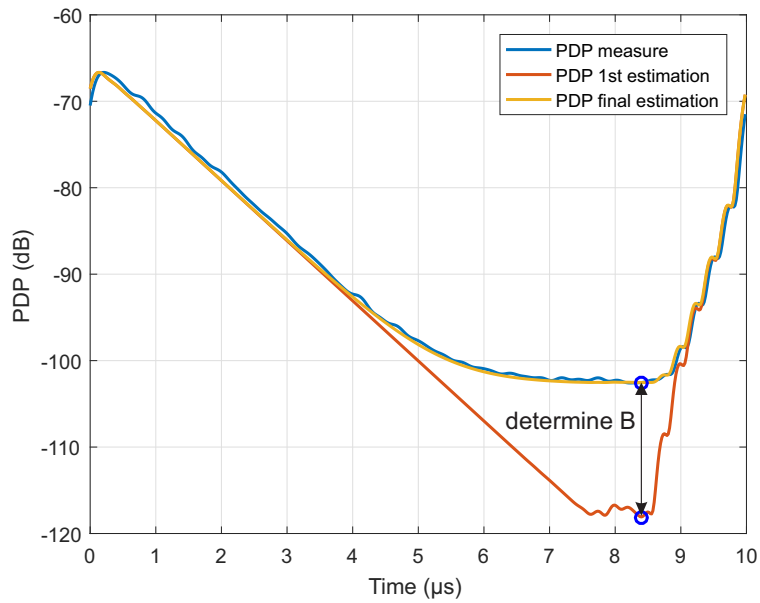


Figure 2.22: The first and final estimation of PDP

dB:

$$\delta = \mathrm{RMS}(|\mathrm{PDP}_{\mathrm{meas,dB}}(t) - \mathrm{PDP}_{\mathrm{model,dB}}(t)|) \tag{2.55}$$

This formula is chosen because it is also the cost function we used in the nonlinear curve fitting. The estimation quality over different frequencies is plotted in Fig. 2.23, which shows the estimated PDP in dB is within 1.2 RMS difference to the measured PDP in dB. Fig. 2.23 shows the estimation techniques works very well.

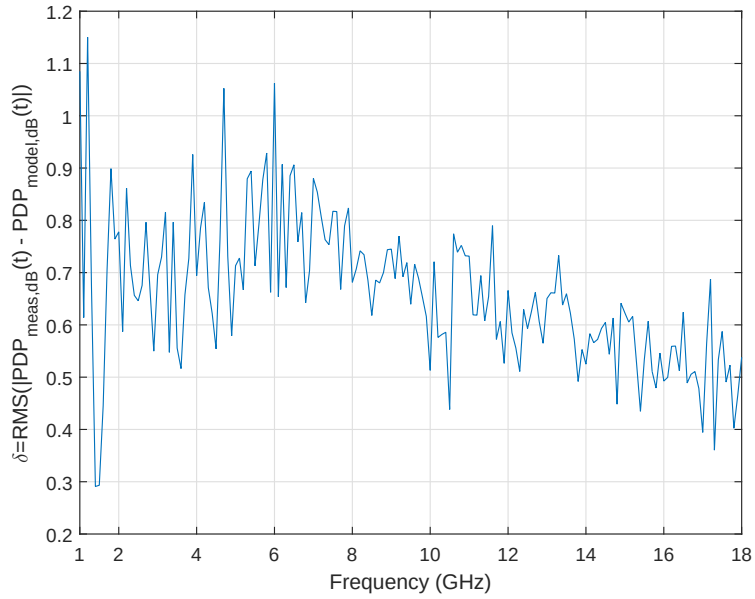


Figure 2.23: The RMS difference between estimated PDP and measured PDP

## 2.10 The early time behaviour of RC and the effect of zero padding in signal processing

The nonlinear model of PDP (2.49) generally matches very well with the signal in Fig. 2.21, but with a careful inspection, the figure shows the nonlinear model has a time offset at almost every point of $t$. This problem may looks trivial, but it will make a difference to the final output of chamber time constant, especially in the case when the chamber time constant needs to be extracted from very few number of $S_{21}$.

The power building up phase of PDP was studied by Holloway [55]. In his research, the PDP was modelled by a double-exponential model which

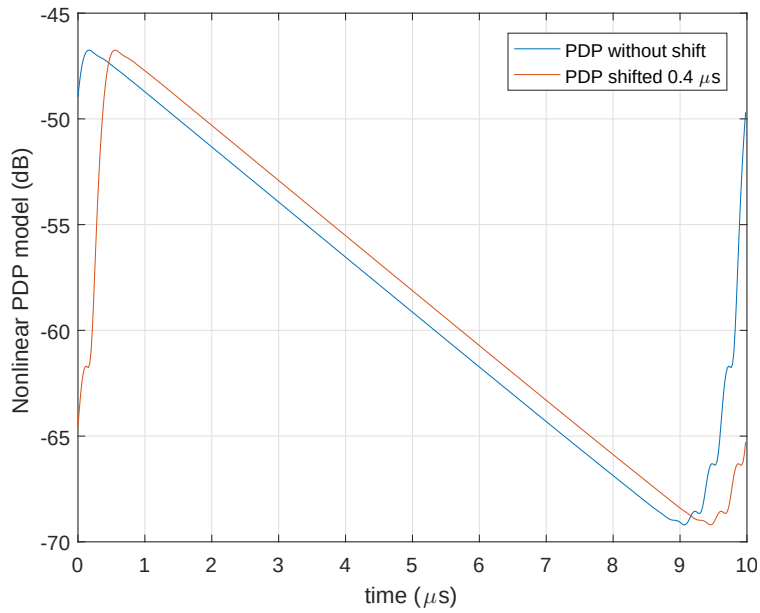


Figure 2.24: The PDP without shift and PDP shifted 0.4 $\mu$s

consisted by a power building up phase and a power decaying phase.

$$\mathrm{PDP}(t) = \begin{cases} P_0 \left[ e^{-t/\tau_{RC}} - e^{-t/\tau_e} \right] & t \geq 0 \\ 0 & t \leq 0 \end{cases} \tag{2.56}$$

Where $\tau_{RC}$ is the chamber time constant, $\tau_e$ is the chamber "ramp-up" time which gives how fast the stored energy build up. In Andersen's work [56], the measurement of PDP was conducted in a low reverberant environment. The first peak of PDP did not come immediately after $t = 0$ but after a certain time which depends upon the distance between transmitting antenna and receiving antenna. In our research the Anderson's idea was chosen to model the PDP since we don't want to introduce the extra argument $\tau_e$ in our model. In terms of the periodic property of the IFFT, the delay of the first peak of PDP can be modelled by circular shifting the PDP for a couple of time steps. The idea is shown in Fig. 2.24.

In the process of nonlinear curve fitting, the nonlinear model is circular shifted from 0 $\mu$s to 0.2 $\mu$s step by step, from which the optimizer will choose a shifted PDP that gives the best fitting quality. As it can be seen in Fig. 2.25. In Fig. 2.25, the measured PDP, the non-shifted PDP model and the shifted PDP model are all looked very similar, but the lower graph shows the shifted model fits better to the measured PDP than the non-shifted model. The maximum difference between the shifted model and the measured PDP is 1.15 dB, while the difference between non-shifted model and measured PDP is 2.63 dB.

Fig. 2.25 only demonstrates the accuracy of fitting with the shifted nonlinear model at a single frequency. The advantage of fitting with shifted PDP model can be shown by plotting cost function from 1 GHz to 18 GHz. The cost function is defined as the RMS difference between measured PDP in decibel and the nonlinear PDP model in decibel:

$$\delta = \mathrm{RMS}(|\mathrm{PDP}_{\mathrm{meas,dB}}(t) - \mathrm{PDP}_{\mathrm{model,dB}}(t)|) \tag{2.57}$$

The comparison results were plotted in Fig. 2.26.

Clearly the fitting quality of shifted PDP model is much better than the non-shifted PDP model over all frequencies from 1 GHz to 18 GHz. The delay of the first peak of the shifted PDP is also given in Fig. 2.27.

## 2.11 The variation coefficient of chamber time constant extracted by nonlinear curve fitting

Comparing to the Q factor determined from G factor in (2.22), the Q factor determined by the chamber time constant is more accurate and has lower

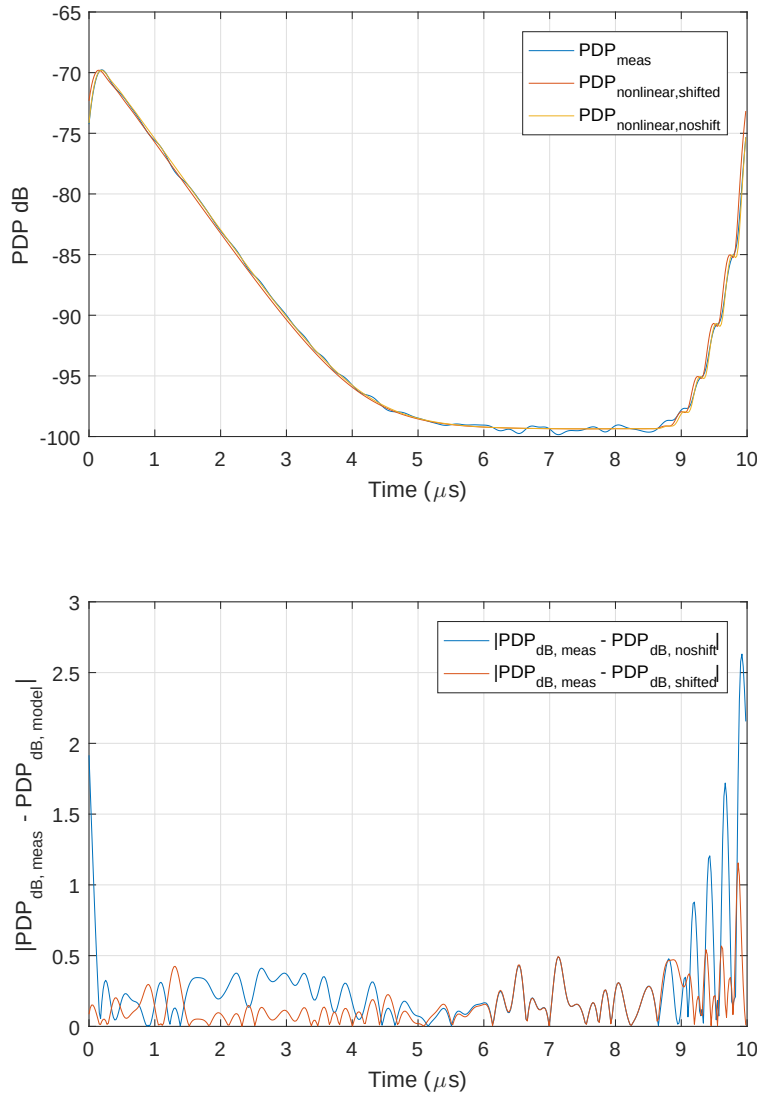


Figure 2.25: The benefit of including the delay of PDP's first peak in non-linear curve fitting

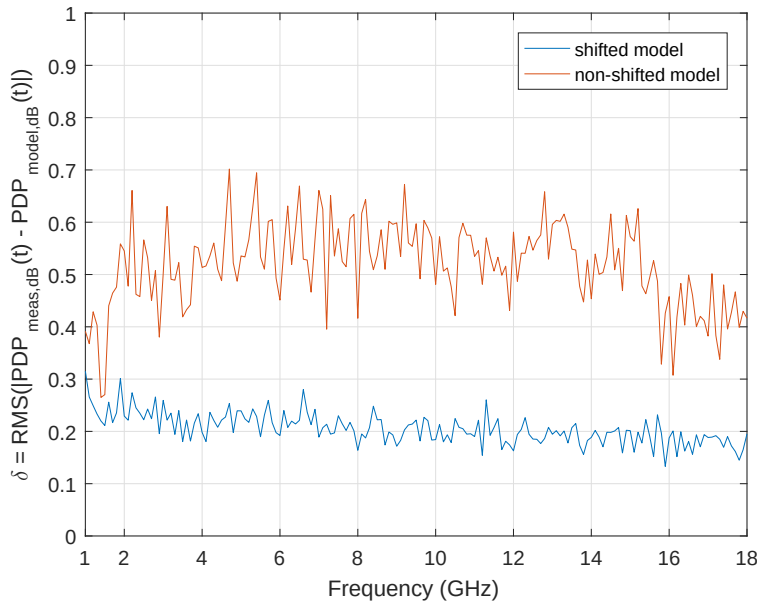


Figure 2.26: The fitting quality of nonlinear fit with shifted model and non-shifted model

variation coefficient [45]. The low variation coefficient will bring lots of benefits to the power related measurements in RC. Since extracting chamber time constant from $S_{21}$ by IFFT involves complex data processing, it is hard to give an analytical model for the variation coefficient of chamber time constant.

The Monte Carlo method is applied to study the distribution of extracted chamber time constant [57]. The Monte Carlo method is defined as the method of studying the distribution propagation by performing random sampling from known probability distributions. Here, the relation between the CIR in the RC and Gaussian process was given in (2.39). A sequence of the CIR can be obtained by choosing a set of values of $A$, $B$, $\tau$, then generating a sequence of $N_1(t)$ and a sequence of $N_2(t)$. Each generated CIR represents a CIR measured at an independent stirrer position in the RC. Thus the whole measurement performed at $N_{\text{ind}}$ independent stirrer positions can

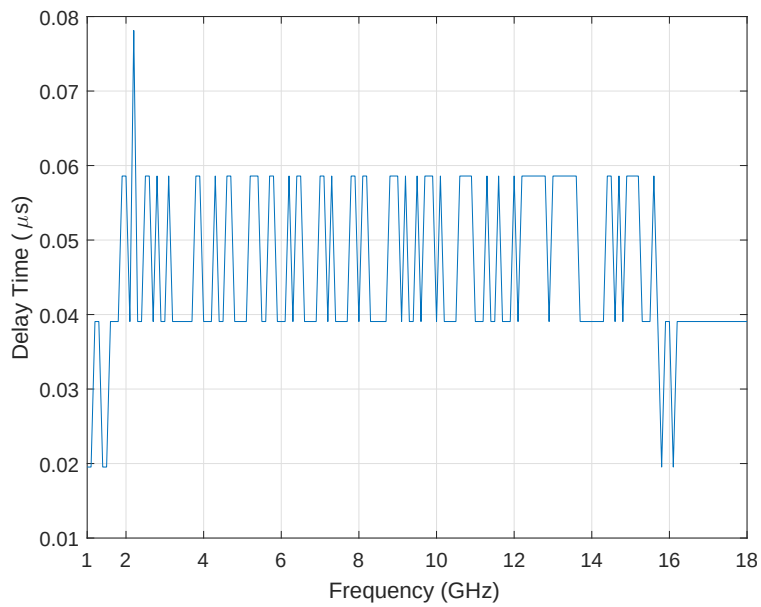


Figure 2.27: Delay of the first peak of PDP. The quantized level is due to the times step of PDP. The sample number of $S_{21}$ in IFFT is 512 (including the number of padded zeros), and the frequency step is $\Delta f = 100$kHz. So the time step can be calculated by $\Delta t = \frac{1}{512 \times \Delta f} \approx 0.02$ns

be simulated by generating the sequence of CIR for $N_{\text{ind}}$ times. All the generated CIR was filtered by a particular window function and then averaged to calculate the PDP. The nonlinear curve fitting was then performed on the averaged PDP to give a evaluation on the chamber time constant. $n$ samples of chamber time constant can be extracted by repeating the whole Monte Carlo process for $n$ times. The flow chart of Monte-Carlo method is illustrate in Fig. 2.28

## 2.12 Evaluating the variation coefficient of ACS from the variation coefficient of chamber time constant

Substituting (2.24) in to (2.21), the measured ACS can be calculated from the chamber time constant by:

$$< \sigma_a >= \frac{V}{c}\left(\frac{1}{\tau_{\text{wo}}} - \frac{1}{\tau_{\text{no}}}\right) \tag{2.58}$$

where $\tau_{\text{wo}}$ is the chamber time constant in the loaded RC; $\tau_{\text{no}}$ is the chamber time constant in the unloaded RC.

The variance of ACS can be evaluated by calculating the Taylor series of ACS about the point $(\tau_{wo}, \tau_{no})$ [58]:

$$< \sigma_a(\tau_{wo}, \tau_{no}) > \approx < \sigma_a(\tilde{\tau}_{wo}, \tilde{\tau}_{no}) > + \left.\frac{\partial < \sigma_a >}{\partial \tau_{wo}}\right|_{\tau_{wo}=\tilde{\tau}_{wo}} \Delta\tau_{wo} + \left.\frac{\partial < \sigma_a >}{\partial \tau_{no}}\right|_{\tau_{no}=\tilde{\tau}_{no}} \Delta\tau_{no} \tag{2.59}$$

where $\tau_{wo}$ and $\tau_{no}$ are the measurement value of chamber time constant;$\tilde{\tau}_{wo}$ and $\tilde{\tau}_{no}$ are the two fixed values of chamber time constant close to the corresponded measurement value; $\Delta\tau_{wo} = \tilde{\tau}_{wo} - \tau_{wo}$ and $\Delta\tau_{no} = \tilde{\tau}_{no} - \tau_{no}$.

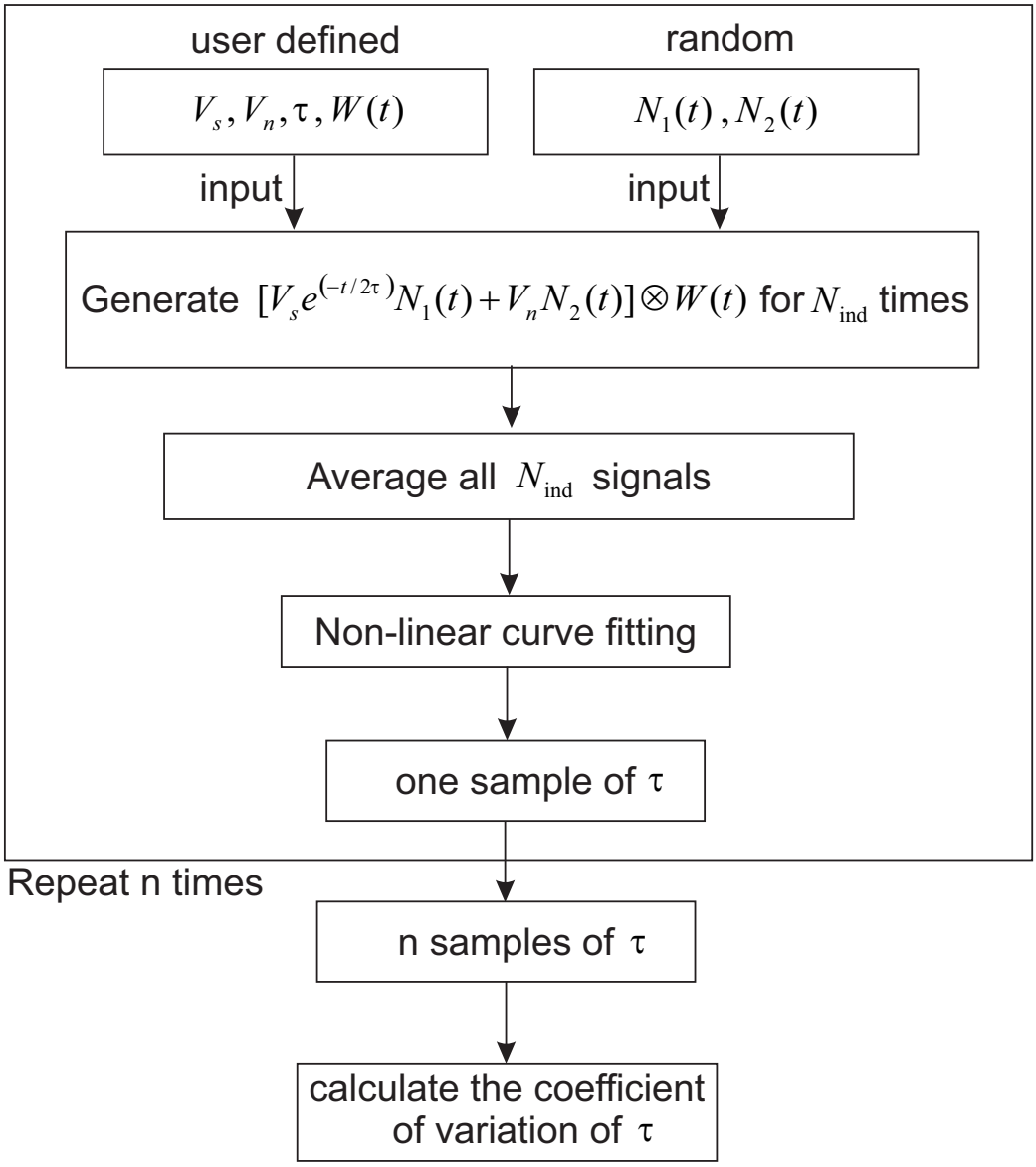


Figure 2.28: Monte Carlo method of evaluating uncertainty of chamber time constant measurement

Equation (2.59) is a linear formula of evaluating the variance of ACS from the variance of $\tau$.

Since $\tilde{\tau}_{wo}$ and $\tilde{\tau}_{no}$ are fixed values, and $\tau_{wo}$ and $\tau_{no}$ are random variables, the variation of $\sigma_a(\tau_{wo}, \tau_{no})$ can be calculated by:

$$\mathrm{Var}(<\sigma_a>) = \left[\frac{\partial <\sigma_a>}{\partial \tau_{wo}}\bigg|_{\tau_{wo}=\tilde{\tau}_{wo}}\right]^2 \mathrm{Var}(\tau_{wo}) + \left[\frac{\partial <\sigma_a>}{\partial \tau_{no}}\bigg|_{\tau_{no}=\tilde{\tau}_{no}}\right]^2 \mathrm{Var}(\tau_{no}) \tag{2.60}$$

Substitute (2.58) into (2.60) gives:

$$\mathrm{Var}(<\sigma_a>) = \left[\frac{V^2}{c^2\tilde{\tau}_{wo}^4}\right] \mathrm{Var}(\tau_{wo}) + \left[\frac{V^2}{c^2\tilde{\tau}_{no}^4}\right] \mathrm{Var}(\tau_{no}) \tag{2.61}$$

According to the definition of variation coefficient which is the ratio between standard deviation and mean value, Equation (2.61) can be rewritten as [59]:

$$\mathrm{Var}(<\sigma_a>) = \left[\frac{V^2}{c^2\tilde{\tau}_{wo}^2}\right] c_v^2(\tau_{wo}) + \left[\frac{V^2}{c^2\tilde{\tau}_{no}^2}\right] c_v^2(\tau_{no}) \tag{2.62}$$

where $c_v(\tau_{wo})$ and $c_v(\tau_{no})$ are the variation coefficient of $\tau_{wo}$ and $\tau_{no}$. So the variance of $\sigma_a$ becomes a function of $c_v(\tau_{wo})$ and $c_v(\tau_{wo})$. Since we assume the values of $\tilde{\tau}_{wo}$ and $\tilde{\tau}_{no}$ are very close to the values of $\tau_{wo}$ and $\tau_{no}$, the coefficient of variation of the measured ACS is approximate to:

$$c_v^2(<\sigma_a>) \approx \frac{\mathrm{Var}(<\sigma_a>)}{\sigma_a^2(\tilde{\tau}_{wo}, \tilde{\tau}_{no})} = \frac{\left[\frac{V^2}{c^2\tilde{\tau}_{wo}^2}\right] c_v^2(\tau_{wo}) + \left[\frac{V^2}{c^2\tilde{\tau}_{no}^2}\right] c_v^2(\tau_{no})}{\frac{V^2}{c^2}\left(\frac{1}{\tilde{\tau}_{wo}} - \frac{1}{\tilde{\tau}_{no}}\right)^2} \tag{2.63}$$

where $c_v(<\sigma_a>)$ is the variation coefficient of the measured ACS. After some simplification, (2.63) transform into:

$$c_v^2(<\sigma_a>) \approx \frac{c_v^2(\tau_{wo}) + t^2 c_v^2(\tau_{no})}{(1-t)^2}, \quad 0 \le t = \frac{\tilde{\tau}_{wo}}{\tilde{\tau}_{no}} \le 1 \tag{2.64}$$

Equation (2.64) is very important because it gives an analytical method of estimating $c_v(\sigma_a)$ from the value of $\tilde{\tau}_{no}$, $\tilde{\tau}_{wo}$, $c_v(\tau_{no})$ and $c_v(\tau_{wo})$. It is also important to point out that this equation has two singular point $t = 1$ and $t = 0$.

If $t = 1$, there is $\tilde{\tau}_{wo} = \tilde{\tau}_{no}$, which corresponds to the case where the object under test has a very small ACS. $t = 1$ will make the denominator on the right side of (2.64) close to zero, thus the variation coefficient of measured ACS will become very big. On the other hand, $t = 0$ corresponds to the case where $\tilde{\tau}_{wo} = 0$, which means the ACS of the object under test is infinitely big. $\tilde{\tau}_{wo} = 0$ also means the PDP measured in a loaded RC transform into a pulse function in time domain, and the extraction of $\tau_{wo}$ from the pulse function is impossible.

Since the Q factor is in proportional to the chamber time constant $\tau$, a similar conclusion can be given to the ACS evaluated from the Q factor by replacing $\tau$ in (2.64) by $Q$, which is:

$$c_v^2(<\sigma_a>) \approx \frac{c_v^2(Q_{wo}) + t^2 c_v^2(Q_{no})}{(1-t)^2}, \quad 0 \leq t = \frac{\tilde{Q}_{wo}}{\tilde{Q}_{no}} \leq 1 \tag{2.65}$$

where $c_v(Q_{wo})$ and $c_v(Q_{no})$ are the variation coefficient of measured Q factor in an RC, $\tilde{Q}_{wo}$ and $\tilde{Q}_{no}$ are the two fixed values of Q factor close to the measured Q factors.

## 2.13 The chamber time constants can give ACS with smaller variation coefficient than the G factors do

Equation (2.65) gives the relation between $c_v(\sigma_a)$ and Q factors. This equations shows measuring Q factor with lower variation coefficient will benefit

the measurement of ACS. As Q factor can be determined by both (2.23) and (2.24), it is worthwhile to show the Q factor determined by chamber time constant has lower variation coefficient than the Q factor determined by G factor, otherwise the development of nonlinear curve fitting techniques would lost its meaning since the determination of G factor is much easier to perform.

The advantage of determining ACS by chamber time constant is demonstrated by showing the variation coefficient of G factor is dominated by the variation coefficient of $< |S_{21}|^2 >$. It is reported in the previous research that the variation coefficient of $< |S_{21}|^2 >$ is usually much higher than the variation coefficient of $\tau$ extracted from PDP [45].

Here we give the analytical formula of the variation coefficient of $< |S_{21}|^2 >$. According to Hill's theory, the real and imaginary part of $S_{21}$ follows the Gaussian distribution [40]. Therefore, if the expectation of the real part and imaginary part are zero, the second moment of $S_{21}$ follows the Chi-squared distribution with a coefficient [60, 61]

$$< |S_{21}|^2 >= \frac{E(< |S_{21}|^2 >)}{2N_{\text{ind}}} \sum_{i=1}^{2N_{\text{ind}}} Y_i^2 \tag{2.66}$$

where $E(< |S_{21}|^2 >)$ is the expectation of $< |S_{21}|^2 >$. $N_{\text{ind}}$ is the number of independent $S_{21}$ samples in mode stirring; $Y_i$ follows normal distribution; $\sum_{i=1}^{2N_{\text{ind}}} Y_i^2$ follows the Chi-squared distribution with the degree of freedom $2N_{\text{ind}}$. Since the variance of the Chi-squared distribution is twice of its degrees of freedom, the variance of $< |S_{21}|^2 >$ is:

$$\text{Var}(< |S_{21}|^2 >) = \frac{< |S_{21}|^2 >^2}{4N_{\text{idp}}^2} 4N_{\text{idp}} = \frac{< |S_{21}|^2 >^2}{N_{\text{idp}}} \tag{2.67}$$

So the variation coefficient of $< |S_{21}|^2 >$ can be written as:

$$c_v\left(< |S_{21}|^2 >\right) = \frac{\sqrt{\mathrm{Var}(< |S_{21}|^2 >)}}{E\left(|S_{21}|^2\right)} = \frac{1}{\sqrt{N_{\mathrm{ind}}}} \tag{2.68}$$

Then we will give the analytical solution of the variation coefficient of ACS evaluated from G factor. Remembering the format of G factor in (2.23), if we assume the value of $| < S_{11} > |^2$, $| < S_{22} > |^2$, $\eta_{\mathrm{Tx}}$, $\eta_{\mathrm{Rx}}$ are all fixed, then:

$$c_v(G) = c_v(< |S_{21}|^2 >) \tag{2.69}$$

According to the relation amongst ACS, G factor, and Q factor, there is

$$c_v^2(< \sigma_a >) \approx \frac{c_v^2(G_{wo}) + t^2 c_v^2(G_{no})}{(1-t)^2}, \quad 0 \le t = \frac{\tilde{G}_{wo}}{\tilde{G}_{no}} \le 1 \tag{2.70}$$

Substitute (2.69) into (2.70), we have:

$$c_v^2(< \sigma_a >) \approx \frac{c_v^2(< |S_{21,wo}|^2 >) + t^2 c_v^2(< |S_{21,no}|^2 >)}{(1-t)^2},$$
$$0 \le t = \frac{< |\tilde{S}_{21,wo}|^2 >}{< |\tilde{S}_{21,no}|^2 >} \le 1 \tag{2.71}$$

Equation (2.71) shows the variation coefficient of ACS calculated by G factor is dominated by the variation coefficient of $< |S_{21}|^2 >$. In Sec. 3.8, we will show by experiment that the G factor gives the ACS with larger variation coefficient than the chamber time constant does.

## 2.14 Summary

In this chapter we firstly modelled the human body by a multilayer planar model and calculated its properties of absorbing EM power. The calculation

shows the fat layer acts as a matching layer between the skin layer and muscle. At one of resonant frequencies, the multilayer model is more lossy than the homogeneous muscle model; while at the other resonance frequency, the multilayer model is weaker in absorbing EM energy than the homogeneous muscle model. Both of the resonance frequencies decreases as the fat layer thickness increases.

Then we introduced the theories on extracting chamber time constant accurately from $S_{21}$. The theories are based on the nonlinear PDP model which includes the effects of window function and noise floor. The nonlinear PDP model matches very well with the measured PDP with RMS error smaller than 1.3 dB from 1 GHz to 18 GHz. The Monte Carlo method of evaluating the statistical uncertainty of chamber time constant is also given. Validation experiment will be conducted in the next chapter to demonstrate the effectiveness of the Monte Carlo method.

# Chapter 3

# Validation experiments of IFFT techniques

## 3.1 The selection of reference object

Just like the vector network analyzer (VNA) needs calibration kit for calibration, the effectiveness of a measurement technique requires an reference object for validation. Here the reference object has been selected as a spherical shell containing 28 litres of deionized water. The shape of the shell is very close to a sphere but not perfectly. It is expected that its ACS could be evaluated using analytical method. The picture of the sphere shell is shown in Fig. 3.8.

The reasons of selecting a sphere as a reference object are two folds. First, the sphere is an isotropic object, which means there is no need of averaging ACS over different directions. Second, the ACS of sphere can be calculated by analytical methods, such as Mie series.

The outer radius of the sphere is 19.4 cm which is obtained by measuring the circumference. The shell thickness is 4 mm measured by a calliper close to the rim of the sphere. The complex permittivity of deionized water is

calculated by Kaatze's formula, in which the water temperature is equal to 20 °C [62]. The sphere shell is made by high density polyethylene (HDPE) and its permittivity is extracted from documented data. There are many researches on HDPE's permittivity but very few of the research had given the wide band permittivity of HDPE. Riddle's research gave the permittivity of HDPE as 2.35 at 11.5 GHz at 21 °C [63]. Seeger's research is done by fitting a sample HDPE into a high frequency wave guide and then curve fitting the spectrum of transmission coefficient to get the permittivity [64]. It gives the result of 2.34 from 26.5 GHz to 40 GHz and no relaxation was found, which means HDPE has no loss. Seeger's measurement is conducted at 26.85 °C (300 K). Seeger also mentioned that the permittivity is 2.34 at 1 MHz and there is no loss of HDPE from 1 MHz to 40 GHz. In general, the permittivity of HDPE is a complicated function of temperature and frequency. Since exhaustively determining the dielectric properties of HDPE in all cases is not the major task of this research, we just use the real constant 2.35 as an approximation to the relative permittivity of HDPE from 1 GHz to 18 GHz.

## 3.2 The University of York reverberation chamber

The University of York reverberation chamber is a shielded room with dimension 4.7 m × 3 m × 2.37 m, loaded with a stirrer whose shape is optimized by GA to minimize the total variation of the field [65]. The field uniformity in the reverberation chamber is verified in the work of Armstrong [66]. Both sides of the chamber wall are galvanized with zinc. There is also a small brass chamber nested in the big chamber, as shown in Fig. 3.2 and Fig. 3.1 The small chamber's size is 0.6 m × 0.7 m × 0.8 m which will be subtracted from the big chamber's volume in the calculation of ACS.

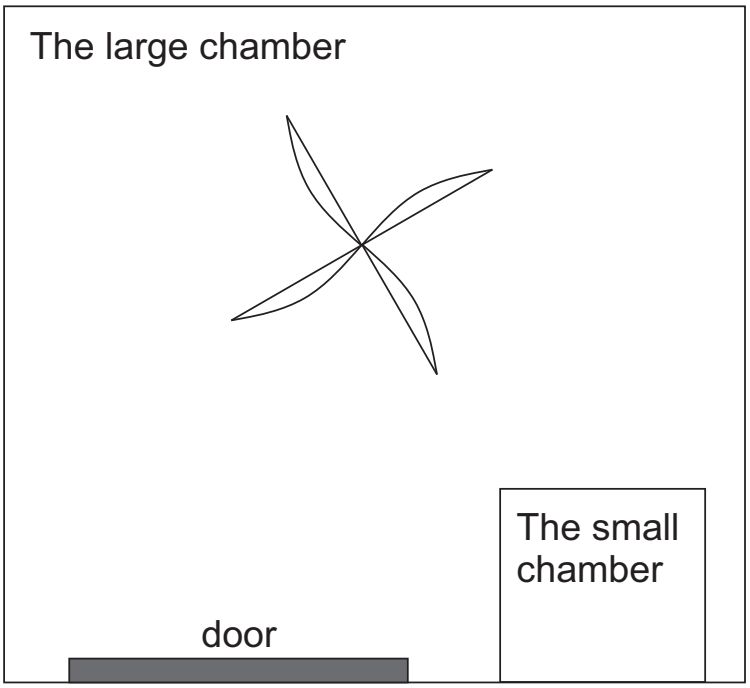


Figure 3.1: Top View of the University of York RC

Figure 3.2: The small RC

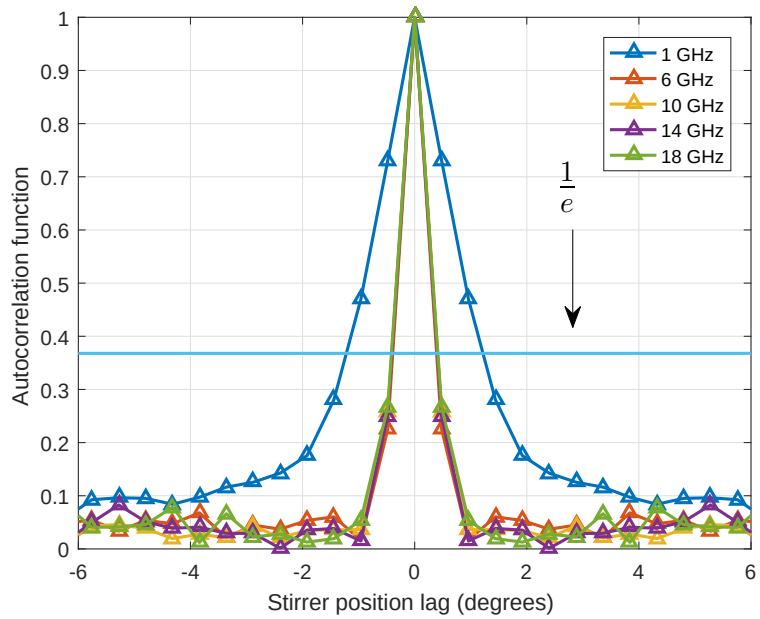


Figure 3.3: Correlation coefficient of $S_{21}$ vs stirrer position lag

## 3.3 Calculating the independent number of $S_{21}$ samples

As stated in Sec. 2.5 and Sec. 2.13, the variation coefficient of PDP, G factor and $< |S_{21}|^2 >$ will all decrease with the number of independent stirrer positions. The number of independent stirrer positions are quantified by calculating the auto correlation function of $S_{21}$ measured at a particular frequency, as demonstrated in Fig. 3.3. The number of markers over the line $\frac{1}{e}$ give the number of correlated stirrer positions measured at the specific frequency. For example in Fig. 3.3, the number of correlated stirrer positions at 1 GHz is 5; the number of correlated stirrer positions at other frequencies is 1. Therefore, the number of independent stirrer positions can be calculated

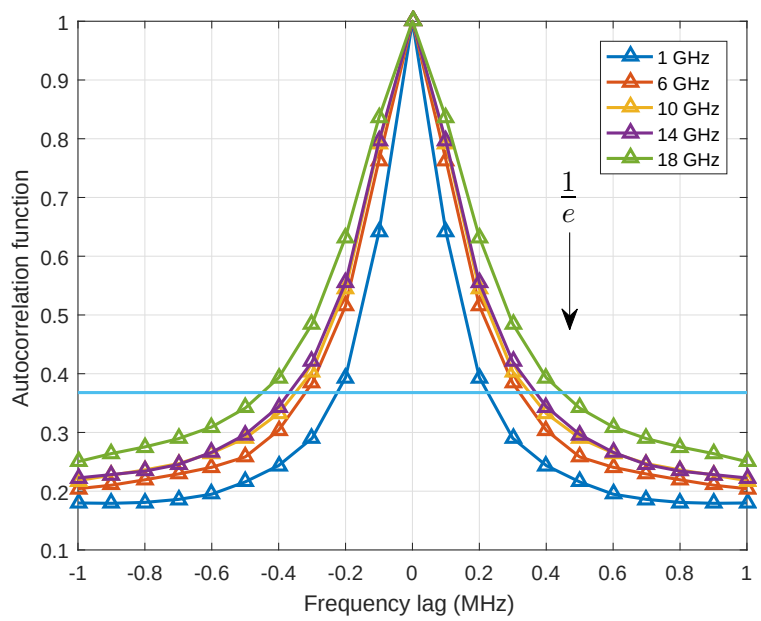


Figure 3.4: correlation coefficient of s21 vs frequency lag

by:

$$N_{\mathrm{s,ind}}(f_0) = \frac{N_{\mathrm{s,tot}}(f_0)}{N_{\mathrm{s,corr}}(f_0)} \tag{3.1}$$

where $N_{\mathrm{s,ind}}$ is the number of independent stirrer positions; $N_{\mathrm{s,tot}}(f_0)$ is the total number of $S_{21}$ measured at a particular frequency $f_0$; $N_{\mathrm{s,corr}}(f_0)$ is the number of correlated $S_{21}$ at $f_0$. Therefore if no frequency stirring is applied, the $N_{\mathrm{s,ind}}$ can be substitute into (2.68) to calculate the variation coefficient of $< |S_{21}|^2 >$.

But in the cases where frequency stirring is applied, the number of independent frequencies $N_{\mathrm{f,ind}}$ should also be considered in $N_{\mathrm{ind}}$ [67]. $N_{\mathrm{f,ind}}$ can be calculated in the similar way as $N_{\mathrm{s,ind}}$ is. Firstly, the correlated frequencies can be obtained by calculating the auto correlation function of a band-limited $S_{21}$ spectrum, as shown in Fig. 3.4 The number of markers over the line $\frac{1}{e}$ gives the number of correlated frequencies. The number of

independent frequencies $N_{\mathrm{f,ind}}$ can be got by:

$$N_{\mathrm{f,ind}}(f_0) = \frac{N_{\mathrm{f,tot}}(f_0)}{N_{\mathrm{f,corr}}(f_0)} \tag{3.2}$$

where $N_{\mathrm{f,tot}}(f_0)$ denotes the total number of frequency points within the band-limited $S_{21}$ spectrum; $N_{\mathrm{f,corr}}(f_0)$ is the number of correlated frequencies.

In the case where both mode stirring and frequency stirring were applied, the independent number of $S_{21}$ can be calculated by:

$$N_{\mathrm{ind}}(f_0) = N_{\mathrm{s,ind}}(f_0) N_{\mathrm{f,ind}}(f_0) \tag{3.3}$$

## 3.4 Choosing the stirrer speed

Since the University of York RC is a single stirrer RC, the $S_{21}$ samples collected at two consecutive rounds of stirring show very strong correlations, as illustrated in Fig. 3.5 and 3.6. Two peaks of auto correlation function can be observed at low frequencies, one at zero degree of stirrer lag; the other at 360 degrees. Therefore, the key to a good ACS measurement is to obtain as many independent number of $S_{21}$ in one round of stirring as possible.

In order to improve the measurement speed, continuous stirring techniques were used. The VNA was working at the maximum sampling rate, which means the total number of $S_{21}$ samples collected in one round of stirring can be adjusted by changing the stirring speed. Slower stirring speed would allow more samples of $S_{21}$ to be measured but the measurement time is longer. In order to find out the best stirring speed, the reference object mentioned in Sec. 3.1 were measured with different stirring speeds, and the measurement results were compared to the theoretical calculations. The details of measurement settings are given in Tab. 3.1. Here the measurement speeds are chosen as 10 steps/sec, 20 steps/sec, and 30 steps/sec; and 6400

| Method number | #1 | #2 | #3 | #4 |
|---|---|---|---|---|
| Stirring method | Continuous | Continuous | Continuous | Stepped |
| Stirrer speed (steps/sec) | 10 | 20 | 30 | N/A |
| Stirrer speed (deg/sec) | 0.5625 | 1.1250 | 1.6875 | N/A |
| Repeats of frequency sweeping | 800 | 400 | 300 | 200 |
| Measurement time | 11 m 23 s | 5 m 38 s | 4 m 17 s | 24 m 21 s |
| Stirrer moved | 384° | 380° | 434° | 360° |
| Results MAPE | 3.593% | 3.881% | 3.885% | 3.696% |

Table 3.1: The setups of sphere measurement. The 'Repeats of frequency sweeping' means the times of frequency sweeping from 1 GHz to 18 GHz during the 'Measurement time'. Techniques of segmented frequency sweeping were applied in all the measurements, which is introduced in Sec. 3.5. The total number of frequency samples from 1 GHz to 18 GHz is 8721.

steps of stirrer moving is idential to the turning of 360 degrees. After the stirrer moves at a particular speed, the frequency sweeping repeats for a specific times which makes the stirrer turning slightly over 360°. The mean absolute percentage error (MAPE) of the measured ACS is defined as [68]:

$$\mathrm{MAPE}(<\sigma_{a,\mathrm{meas}}>) = \mathrm{mean}\left(\left|\frac{<\sigma_{a,\mathrm{meas}}(f)> - <\sigma_{a,\mathrm{sim}}(f)>}{<\sigma_{a,\mathrm{sim}>}(f)}\right|\right) * 100\% \tag{3.4}$$

where $<\sigma_{a,\mathrm{meas}}>$ is measured ACS of the sphere model; $<\sigma_{a,\mathrm{sim}}>$ is the theoretical value of ACS; mean($\cdot$) denotes averaging over frequencies. Tab. 3.1 shows the measurement setup #1 (continuous stirring) gives ACS with smaller MAPE than the stepped stirring does, and the measurement with setup #1 also finishes about 12 minutes quicker than the stepped stirring. Since the measurement accuracy of setup #2 and setup #3 is worse than setup #1, we applied setup #1 in the measurement of human body ACS.

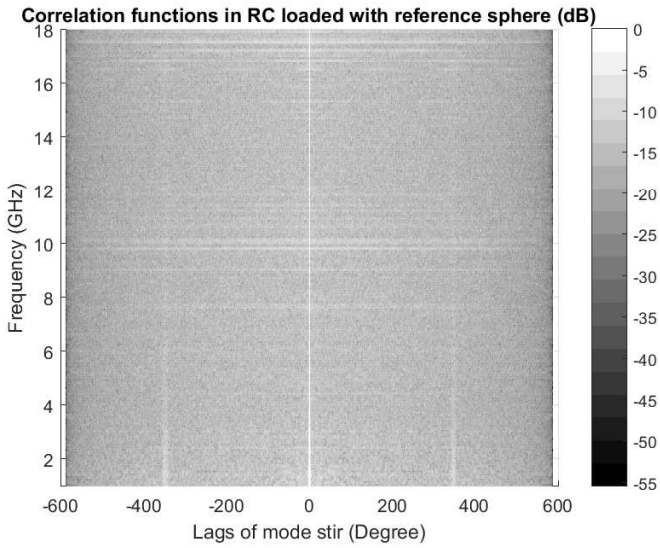


Figure 3.5: Correlation functions in the RC loaded with reference sphere

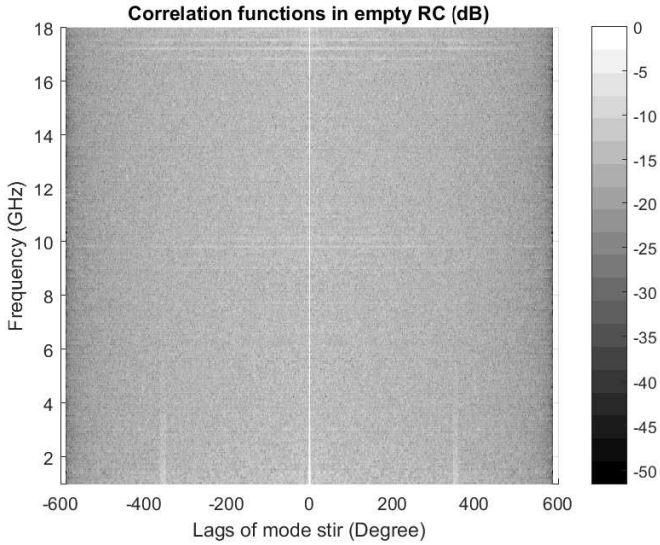


Figure 3.6: Correlation functions in the empty RC

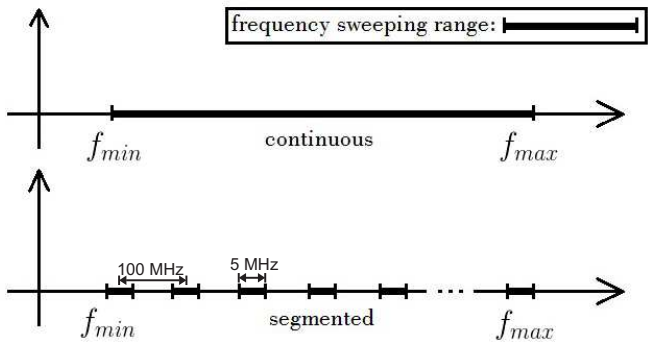


Figure 3.7: The segmented frequency sweeping setups

## 3.5 Segmented sweeping

As shown in Fig. 2.21, the nonlinear curve fitting works fine with arbitrary window functions. Therefore, we are free to choose narrow window functions to extract PDP. To improve the measurement speed, the $S_{21}$ samples which were not included in the IFFT are skipped in the measurement. Only small segments distributed at desired frequencies were measured. Many of today's VNA have such a function of segmented frequency sweeping. The central frequencies of each segment were linearly stepped from 1 GHz to 18 GHz with a step size of 100 MHz. The bandwidth of each segment is 5 MHz and the frequency step of each segment is 100 kHz. Therefore, every segment have 51 $S_{21}$ samples. The whole frequency sweep from 1 GHz to 18 GHz will be performed 800 times in 11 minutes as given in Table 3.1. The setup of segmented frequencies were illustrated in Fig. 3.7.

Figure 3.8: The measurement setups of the sphere model

## 3.6 Measurement results: Non-shifted model and shifted model

The measurement setups are shown in Fig. 3.8. The reverberation chamber was loaded with an ETS 3115 horn antenna and an ETS 3117 horn antenna that both operate from 1 GHz to 18 GHz. Both of the antennas were connected to the VNA through the bulk head on the chamber walls. The stirring setup is chosen as setup #1 in Table 3.1. The frequency sweeping setups were given in Sec. 3.5. Win #1 illustrated in Fig. 2.17 was applied to each frequency segment from 1 GHz to 18 GHz to extract the PDP. The PDP were then fitted by both the shifted model and non-shifted model to extract the

chamber time constant, and the chamber time constant were then used to calculate the ACS of the sphere model. The ACS results given by the non-shifted model and shifted model were compared in Fig. 3.9. The shifted model gave ACS results closer to the Mie series from 11 GHz to 16 GHz than non-shifted model does.

Considering the advantage of the shifted PDP model shown in Fig. 3.9 and Fig. 2.25, it was used in the extraction of ACS in the remainder of this thesis.

## 3.7 Measurement results: application of different window functions

As shown in Fig. 2.21, the nonlinear PDP model fits well with the PDP filtered by arbitrary window functions. In this section we will show experimentally that the nonlinear curve fitting technique can give more accurate chamber time constant value than the linear curve fitting by applying both techniques to the same group of $S_{21}$.

Firstly, the $S_{21}$ of a RC loaded with the sphere model was measured. The three different window functions shown in Fig. 2.17 were applied on the $S_{21}$. All the PDP extracted by three different window functions were fitted by both the linear model and nonlinear model to extract the chamber time constants. The chamber time constant were then used to calculate the sphere ACS.

All the ACS extracted by linear curve fitting with different window functions was shown in Fig. 3.10.

The figure shows the linear curve fitting lost its accuracy when the narrowist window (Win #3) is applied. The mean absolute percentage error (MAPE) of ACS extracted by Win #1, Win #2, Win #3 are 3.6%, 7.5%,

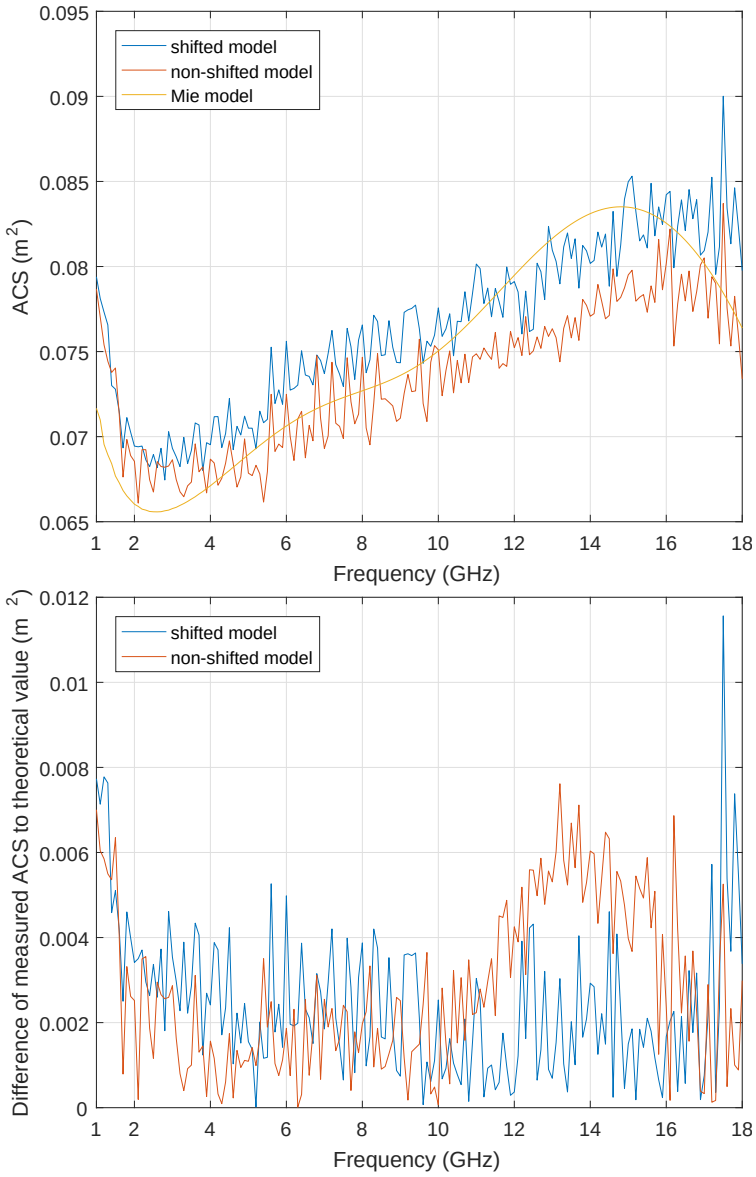


Figure 3.9: Benefit of fitting with shifted PDP model on ACS measurement

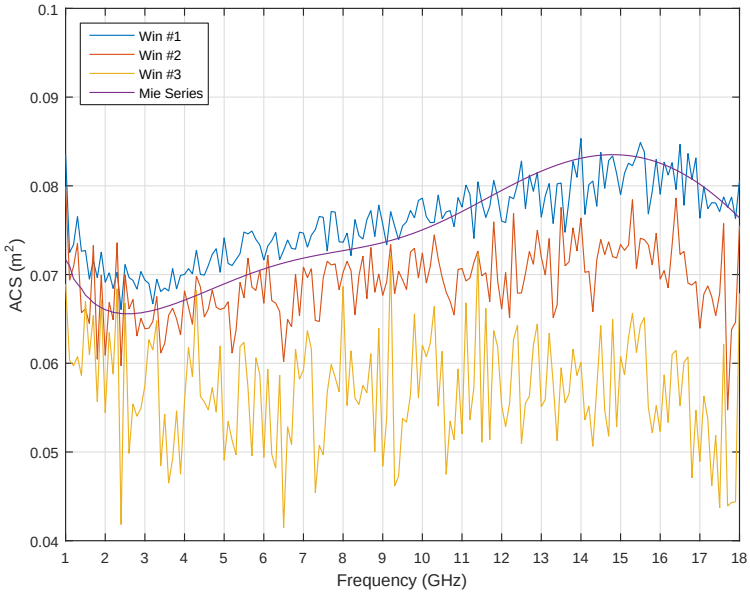


Figure 3.10: The ACS extracted by linear curve fitting

22.7%, respectively.

In contrast with the ACS extracted by linear curve fitting, the ACS extracted by nonlinear curve fitting achieves a much better accuracy, as shown in Fig. 3.11. The MAPE of ACS extracted by nonlinear curve fitting with Win #1, Win #2, Win #3 are 3.4%, 3.5%, 5.4%, respectively.

Generally, the ACS extracted by the application of smaller window functions tend to have larger MAPE and the nonlinear curve fitting is less sensitive to the window width than linear curve fitting. In the case where the window function is only 1 MHz wide, the nonlinear curve fitting can reduce the MAPE of extracted ACS by 17.3%.

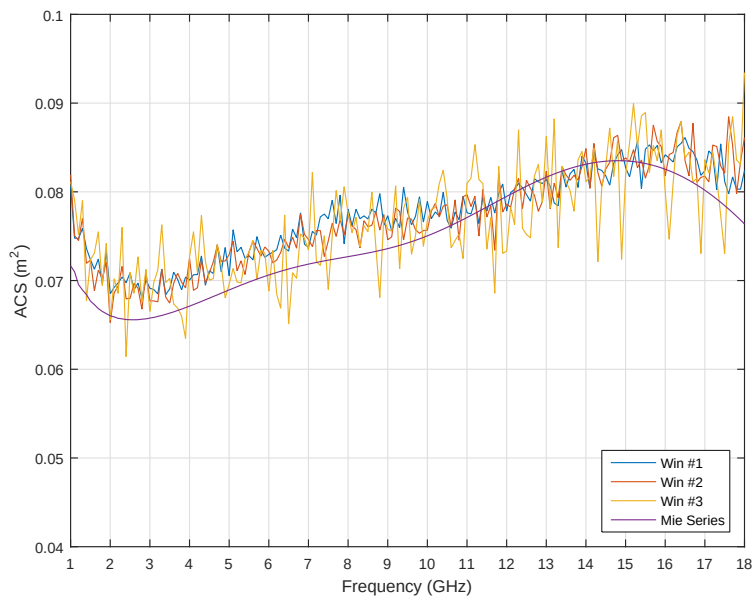


Figure 3.11: The ACS extracted by nonlinear curve fitting

## 3.8 Measurement results: IFFT method vs. G factor method

As pointed out in Sec. 2.13, the ACS of the object under test in the RC can be extracted from the G factor and chamber time constant. The averaged ACS extracted from chamber time constant have both the better accuracy and smaller uncertainty than the ACS calculated from G factor. This conclusion will be proved experimentally in this section.

Due to the homogeneous property of the diffuse field in the RC, the object under test is free to be placed at any position within the working volume of the RC and similar averaged ACS measurement results were expected. Therefore, we chose 16 independent measurement setups and the distribution of measured ACS were studied. The measurement setups were shown in Fig. 3.12. The sphere model was moved to 4 different positions which were at

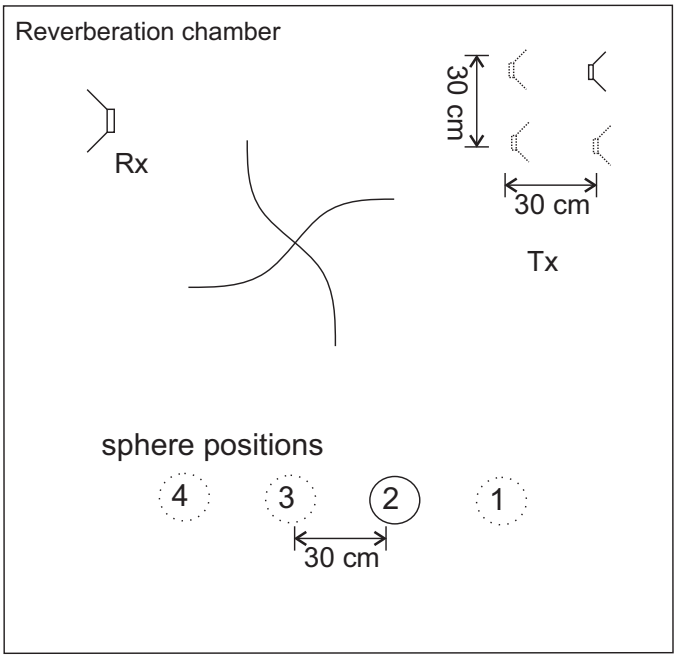


Figure 3.12: The measurement setups for evaluating ACS measurement uncertainty

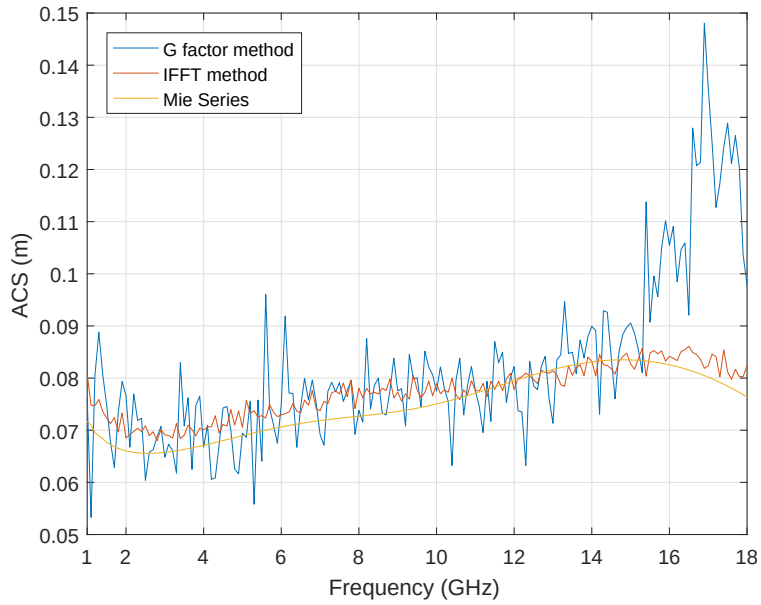


Figure 3.13: The ACS extracted by G factor method and the ACS extracted by IFFT method

least one wave length apart from each other. For each sphere position the transmitting antenna was moved to 4 different positions as well. Therefore the whole measurement included $4 \times 4 = 16$ different setups. The ACS of the sphere model was measured in all 16 different setups and the variation coefficient of measured ACS was then calculated.

Fig. 3.13 compares the ACS extracted by the G factor and the ACS extracted by the chamber time constant. In the evaluation of G factor, the radiation antenna efficiencies of both receiving antenna and transmitting antenna were assumed to be 0.9 [69]. The figure shows ACS extracted by G factor method has higher variance than the ACS extracted by the chamber time constant. The big error of G factor method above 16 GHz because of the power leakage through the ventilation panel. The picture and structure of the ventilation window is shown in Fig. 3.14 and Fig. 3.15, respectively. The edge length of each cell of the ventilation window is 9 mm. Since each

Figure 3.14: The picture of the ventilation panel in the University of York RC

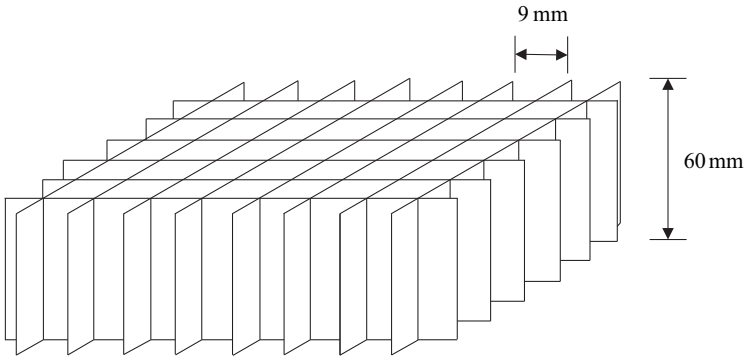


Figure 3.15: The structure of the ventilation panel in the University of York RC

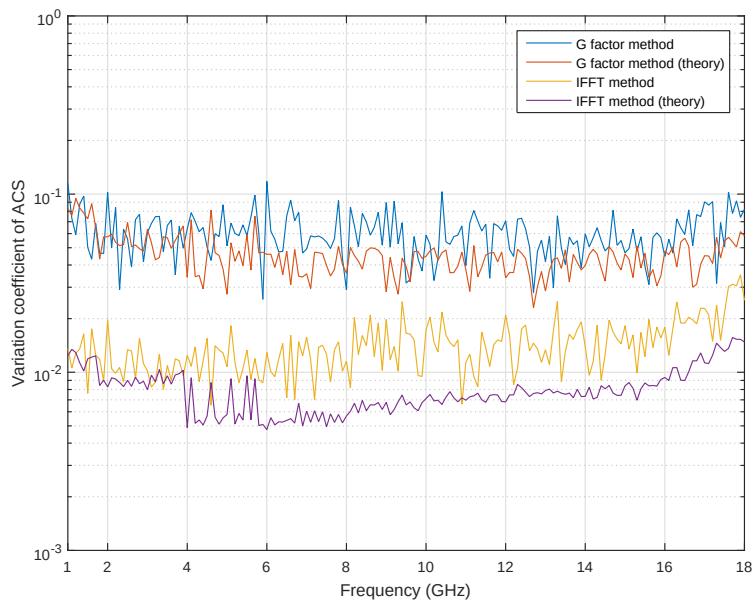


Figure 3.16: The coefficient of variation of measured ACS

cell of the ventilation window can be considered as a small wave guide, the cut off frequency of each cell can be evaluated by:

$$f_c = \frac{c_0}{2\Delta x} \tag{3.5}$$

where $f_c$ is the cut off frequency; $c_0$ is the speed of light in free space; $\Delta x$ is the edge length of each cell. Here we have $f_c = \frac{3.0\times10^8\,\mathrm{m/s}}{2\times9\times10^{-3}\,\mathrm{m}} = 16.7\,\mathrm{GHz}$, which is close to the frequency above which the G factor method lose its accuracy. Below 16 GHz, the MAPE of the ACS given by G factor is 7.50%, while MAPE of ACS given by the chamber time constant is only 3.52%, which is 3.98% less. The variation coefficient of the ACS extracted by both methods were compared in Fig. 3.16. The theoretical value of the variation coefficient is calculated by (2.70) and (2.64), where the $N_{ind}$ for calculating $c_v(G)$ is obtained by the method introduced in Sec. 3.3. The value of $c_v(\tau)$ is obtained by the Monte-Carlo method introduced in Sec. 2.11. Fig. 3.16

shows both (2.70) and (2.64) can predict the variation coefficient of measured ACS effectively. Fig. 3.16 also shows the ACS calculated from chamber time constant has lower variation coefficient than the ACS calculated from the G factor, which proves the idea given in Sec. 2.13. In general, the G factor are more sensitive to the slight non-uniformity of the fields in the RC than the chamber time constant, because the G-factor is evaluated from the S-parameters measured at a single position in the chamber; while the chamber time constant shows the overall power level change in the whole chamber, so that the non-uniform feature of the fields is averaged out.

## 3.9 Measurement results: Measurement range of ACS

As mentioned in Sec. 2.12, the IFFT technique of extracting ACS from $S_{21}$ tend to have larger uncertainty if the object under test has very small ACS. To validate this theory, a series of cuboid absorbers were measured in the RC.

The cuboid sizes were listed in Tab. 3.2 and the picture of all cuboids were in Fig. 3.17. The cuboid were made by LS22 absorber whose complex permittivity was fitted to a three-pole Debye dispersion model [61, 70]:

$$\hat{\epsilon}_r = \epsilon_\infty + \sum_{k=1}^{3} \frac{\Delta\epsilon_k}{1 + j\omega\tau_k} + \frac{\sigma_{\mathrm{DC}}}{j\omega\epsilon_0} \tag{3.6}$$

where $\epsilon_\infty = 1.1725$, $\Delta\epsilon_1 = 1.04\times10^{-3}$, $\Delta\epsilon_2 = 17.9$, $\Delta\epsilon_3 = 0.490$, $\tau_1 = 55.3$ms, $\tau_2 = 0.188$ns, $\tau_3 = 6.20$ps, $\sigma_{\mathrm{DC}} = 0.1$mS/m.

The theoretical value of all cuboids' ACS was calculated by Mie series. The radius of the Mie models were chosen as the volume-equivalent radius of each cuboid. The ACS of 5 cuboids extracted by nonlinear curve fitting

Table 3.2: Mean absolute percentage error (MAPE) of cube ACS measurement

| cube/cuboid size | Win #1 | | Win #2 | | Win #3 | |
|---|---|---|---|---|---|---|
| | linear | nonlinear | linear | nonlinear | linear | nonlinear |
| 40*40*33 $mm^3$ | 41% | 28% | 75% | 42% | 144% | 75% |
| $(50mm)^3$ | 27% | 20% | 39% | 26% | 69% | 54% |
| $(70mm)^3$ | 22% | 20% | 27% | 21% | 54% | 30% |
| $(90mm)^3$ | 16% | 13% | 19% | 15% | 32% | 21% |
| $(115mm)^3$ | 7% | 5% | 12% | 7% | 24% | 12% |

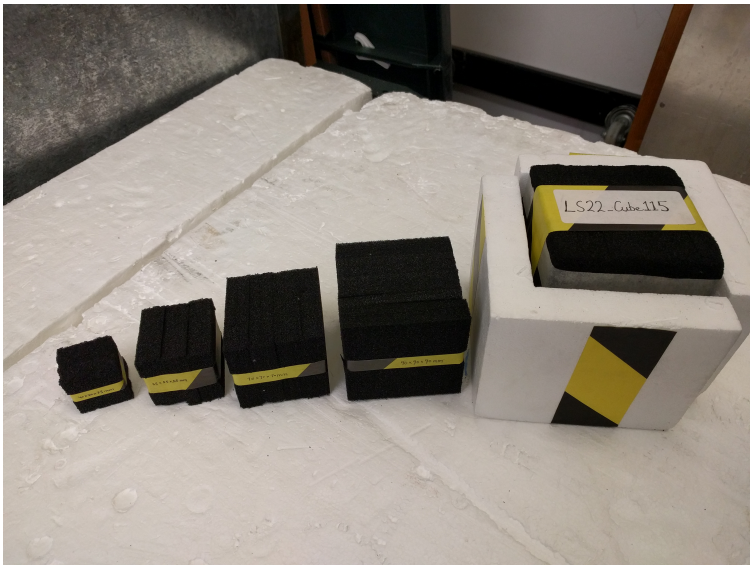


Figure 3.17: The series of absorber cuboids, made from carbon-loaded foam

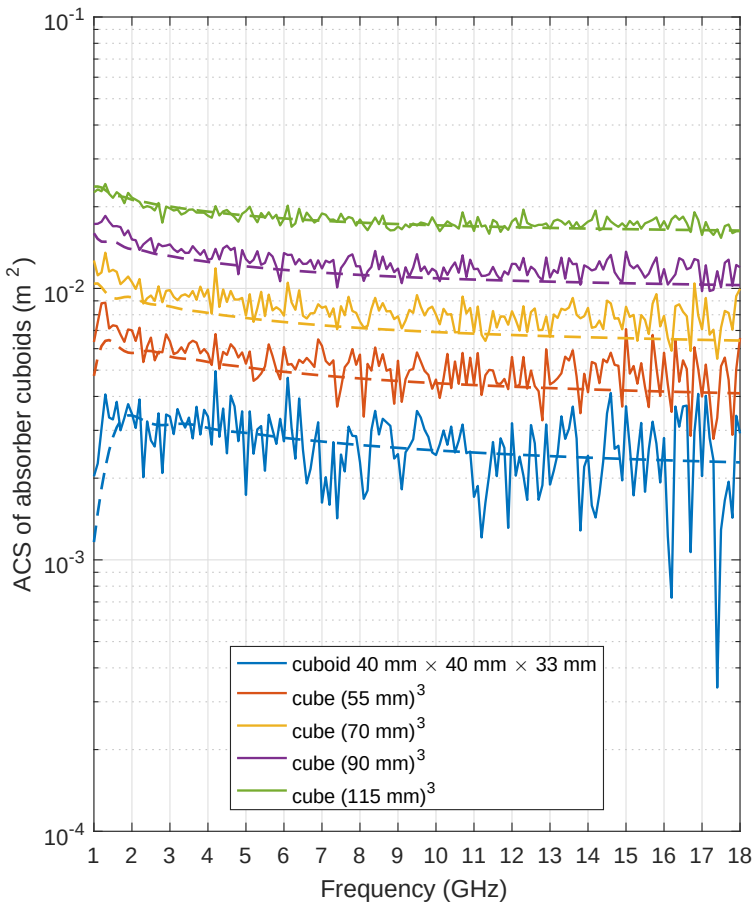


Figure 3.18: The ACS of the absorber cuboids extracted by Win #1. The dashed line is the results calculated by Mie series.

with Win #1 were demonstrated in Fig. 3.18, which shows the measurement result of all cuboids matches well with the Mie predictions. Win #2, Win #3 were also applied to extract the ACS of the cuboids. The MAPE of ACS extracted by different techniques is listed in Table 3.2. The nonlinear curve fitting always gives the ACS with higher accuracy than the linear curve fitting does in the application of any one of the three window functions. The ACS of the smallest cuboid has the maximum MAPE, which proves the point given in Sec. 2.12. The MAPE decreased as the cuboid size increases.

## 3.10 The polystyrene sheets to support human subjects

Since the tangential electric field on the conducting wall of a cavity needs to be zero, the total field close to the boundaries of a reverberation chamber can not maintain its statistical isotropy and homogeneity [71]. Therefore, the subject should be placed far away from the walls of the RC (including the floor) to make sure it is exposed under a isotropic diffuse electromagnetic fields. On the other hand, the morphological study requires the surface of human body to be fully exposed in the electromagnetic fields, therefore the human subjects should spread theirs limbs during the measurement. However, spreading the limbs without support during the whole measurement can be hard because the measurement would last 11 minutes and 23 seconds.

In our research, 16 layers of polystyrene sheets were purchased to support the human subjects. The size of each polystyrene sheet is $1200\,\mathrm{mm} \times 2400\,\mathrm{mm} \times 25\,\mathrm{mm}$. Therefore, the stacked sheets are of $25\,\mathrm{mm} \times 16 = 400\,\mathrm{mm}$ height, which is larger than the wavelength of lowest frequency at 1 GHz. The human subjects would be able to lie down on the polystyrene sheets and spread their limbs without problem.

The polystyrene sheets should not have high ACS since the PDP would transform to a impulse-like function. The ACS of the polystyrene sheets have been extracted by shifted PDP model, which is introduced in Sec. 2.10 and the measurement results is compared to the ACS of sphere model in Fig. 3.19. The figure shows the ACS of polystyrene sheets increase with frequencies, but still quite small comparing to the ACS of sphere. According to Hill's theory, the Q factor of a reverberation chamber will be dominated by the major power loss mechanism [41], the effect of polystyrene blocks can be neglected.

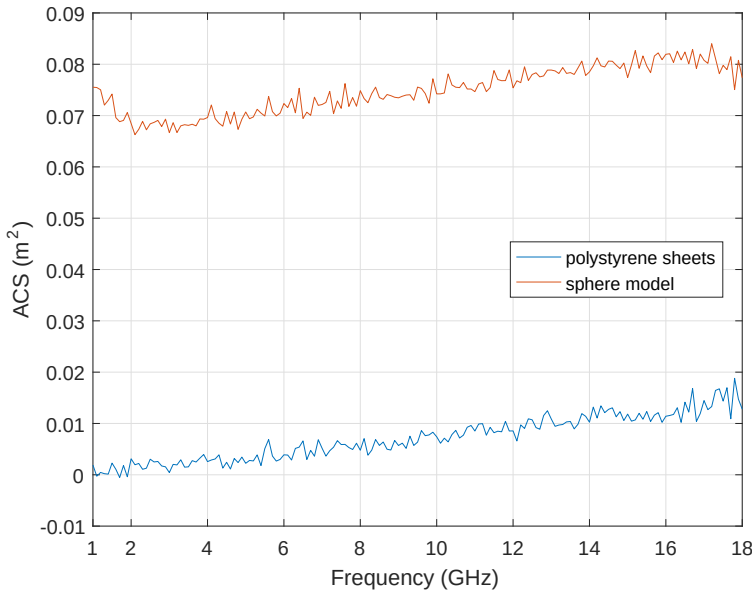


Figure 3.19: ACS of polystyrene sheets

## 3.11 Determining the structure of the sphere model by genetic algorithm

As demonstrated in Fig. 3.11, the sphere ACS extracted by nonlinear curve fitting corresponds very well with the theoretical value, which makes it possible to map the measured ACS to the structure of the spherical model.

The genetic algorithm (GA) is applied to extract the structure of the spherical model from the measured ACS. GA is an optimization technique which can be used for both constrained and unconstrained problems. Unlike classical optimization methods which finds the optimized value by iteration, the GA finds optimized value by random sampling and selection. Therefore, the GA is very good at dealing with multidimensional problems in which the cost function have complicated landscapes [72].

Since GA is a randomized method of optimization, it does not give a fixed

| Optimization method | GA |
|---|---|
| bound of $r$ | [0.1 m, 0.3 m] |
| bound of $d$ | [1 mm, 10 mm] |
| bound of $\epsilon$ | [1, 4] |
| Population Size | 10 |
| Generation Size | 50 |

Table 3.3: Setups for GA optimization

result but a random variable. Therefore, the output given by GA was then input to the Levenberg-Marquardt optimization method to get a fixed result.

The optimization problem is as follow:

Given the measured ACS of a deionized water sphere covered by a lossless dielectric shell, determine the outer radius, shell thickness and the permittivity of the shell.

The cost function is defined as the MAPE of measured ACS to optimised model:

$$\delta\left(r, d, \epsilon\right) = \text{mean}\left(\left| < \sigma_{\text{meas}} > - < \sigma_{\text{opt}}(r, d, \epsilon) > \right|\right) \times 100\% \tag{3.7}$$

where $r$ is radius. $d$ is the thickness of shell. $\epsilon$ is the relative permittivity of shell. $< \sigma_{\text{opt}}(r, d, \epsilon) >$ is the ACS of sphere model under optimization. The goal is to find the values of $r$, $d$, and $\epsilon$ which minimize the cost function $\delta$.

The setups of the GA optimization were listed in Table 3.3. The GA will give optimized values of $r$, $d$, and $\epsilon$, which will then be used as the starting values for Levenberg- Marquardt method to obtain fixed solutions. The fitted results were plotted in Fig. 3.20.

The figure shows the GA gives a very good fit to the measurement data, and the value of optimized cost function (3.7) is only 0.12%. The optimized value of $r, d, \epsilon$ were compared to the measurement data in Table 3.4. It can be seen the GA outputs are very close to the measurement data.

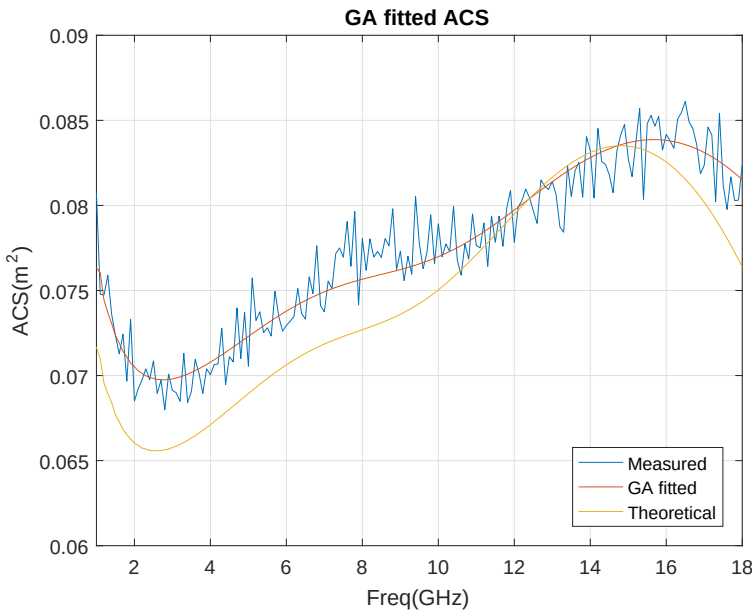


Figure 3.20: The ACS of Sphere: comparison between measurement value and Mie results

| | GA optimized value | measured value |
|---|---|---|
| r | 19.8 cm | 19.4 cm |
| d | 4.0 mm | 4.0 mm |
| $\epsilon$ | 2.07 | 2.35 |

Table 3.4: A comparison of GA optimized sphere parameters and measured parameters

## 3.12 Summary

A series of experiments were performed to validate the theories of extracting ACS from $S_{21}$ by IFFT techniques. Experiments have shown the IFFT techniques give ACS results with 3.98% less MAPE than the G factor method does. Different window functions were applied to filter the PDP, and the chamber time constant given by nonlinear curve fitting is not sensitive to the applied window functions. The result shows the nonlinear curve fitting typically requires 60% fewer of $S_{21}$ than linear curve fitting to extract the ACS with the same accuracy. Thanks to the accuracy of ACS extracted by nonlinear curve fitting, the structures of the object under test can be extracted from the measured ACS by the GA optimizer, which provided a new way of determining the inner structures of a lossy object.

# Chapter 4

# Human body ACS measurement

## 4.1 The ACS of human body with different postures

As mentioned in the earlier research, the posture of human body can make a lot of difference to its ACS or WBSAR. In the computational research of Uusitupa [73], one model with with six different postures were put under simulation. The result shows seated pose would have about 10% less WBSAR comparing to standing straight over 2 GHz if a plane wave with vertically polarized E-field is incident from the front. This conclusion also stands if the E-field of incident wave is horizontally polarized. Findlay's research on the NORMAN model with 4 different poses shows sitting down can decrease the WBSAR by at least 20% at the resonant frequencies below 300 MHz [74]. The ACS measurement of a sitting posture in the RC shown a 4-17% of decrease comparing to the both-hands-up posture from 1 GHz to 15 GHz [75, 76].

Since the new IFFT technique was introduced, the posture effect on human body ACS can be determined more accurately than before. Here five postures shown in Fig. 4.1 were studied. The measurement setups were the same as the setups we used in the sphere model measurement. The measured ACS of 5 different postures were compared in Fig. 4.2.

Same as the conclusion given in [75], the physically more stretched posture tend to give higher ACS, therefore the Supine-X posture gives the overall highest ACS from 1 GHz to 18 GHz. The Seated-1 posture gives the least ACS. Fig. 4.2 also shows the posture change will not change the shape of ACS but simply shift the ACS curve up and down. This can be demonstrated by normalizing the measured ACS of different postures by the ACS of 'Supine-Normal' pose, which is

$$< \sigma_{a,\text{norm}} >= \frac{< \sigma_a >}{< \sigma_{a,\text{Supine-Normal}} >} \tag{4.1}$$

The results of $< \sigma_{a,\text{norm}} >$ were plotted in Fig. 4.3. In the remainder sections we will show the morphological parameters will change the shape human body ACS curve, not simply shift the curve up and down.

In our research the 'Supine-Star' pose was selected in the human body ACS measurement. 'Supine-X pose' was not chosen because it is uncomfortable to hold for 11 minutes.

## 4.2 Populations under study

The ethics approval for the experiment is obtained from the Physical Sciences Ethics Committee of the University of York. The subjects under study are mainly recruited from the faculty and students of the Department of Electronic Engineering of the University. The following parameters of the subjects were recorded: age, ethnicity (asian or non-asian), gender, height,

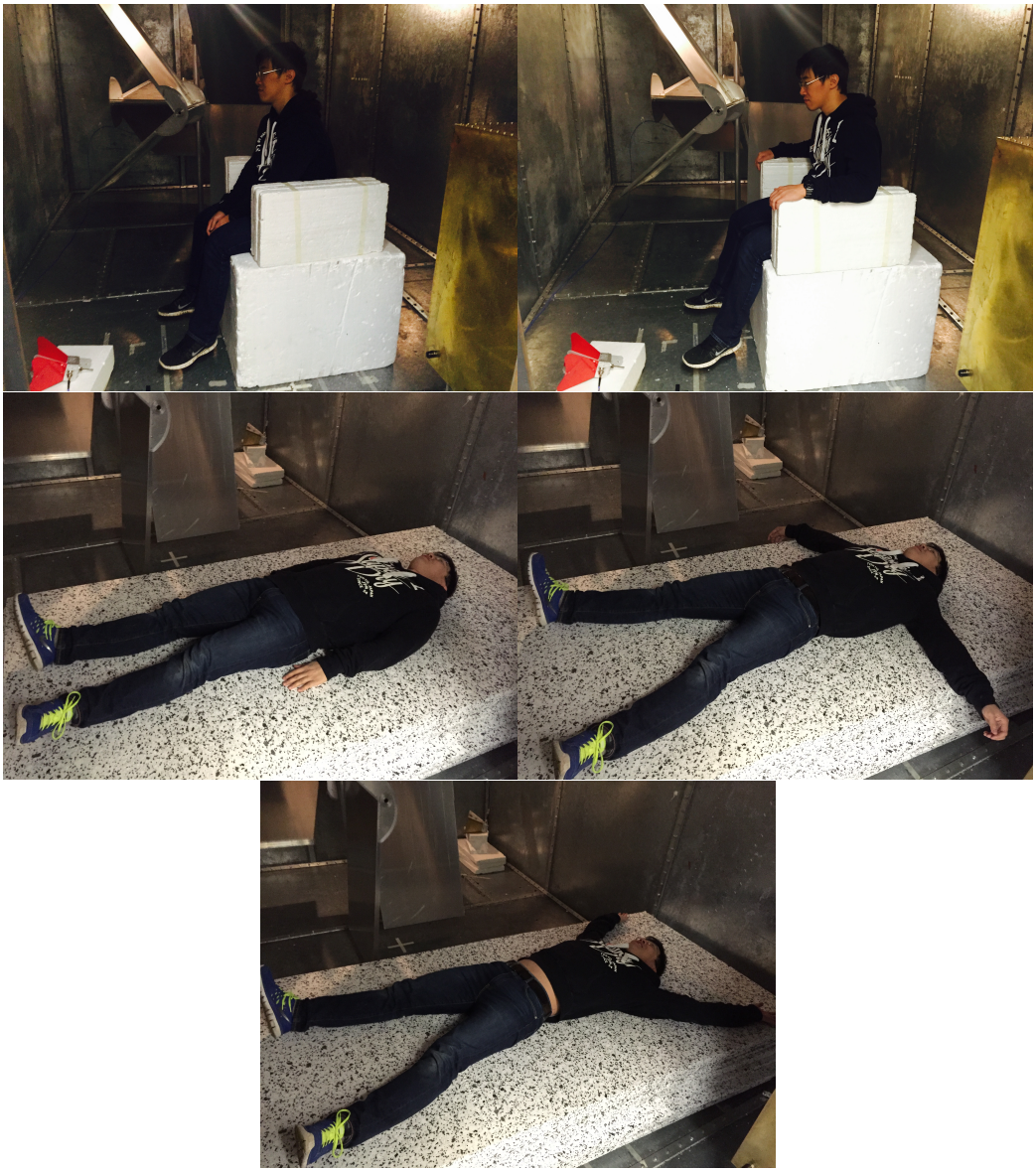

Figure 4.1: The five different postures measured in the RC. The names of the all poses are (left to right, top to bottom): Seated-1, Seated-2, Supine-Normal, Supine-Star, Supine-X

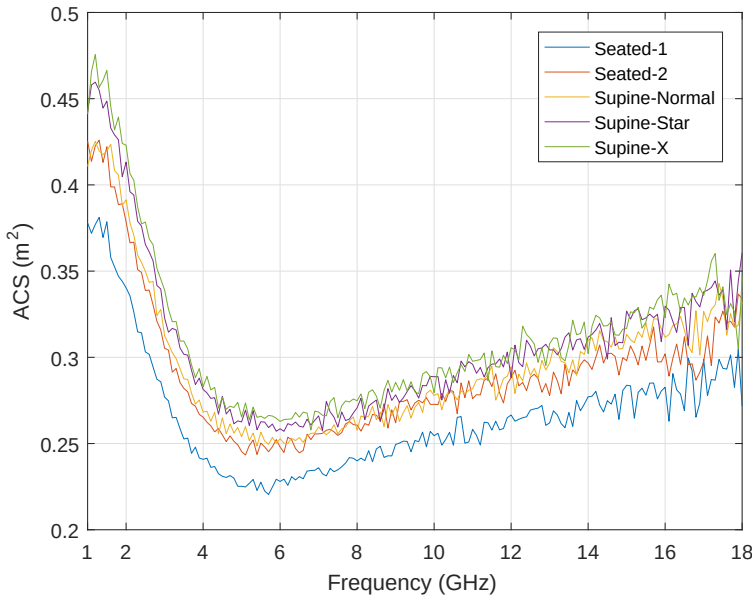


Figure 4.2: The human body ACS of the subject in Fig. 4.1 in five different postures

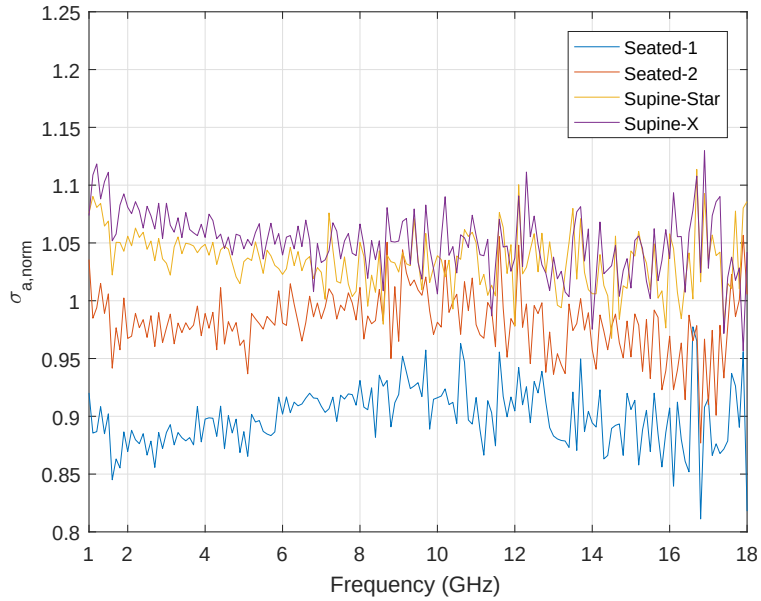


Figure 4.3: The normalized human body ACS the subject in Fig. 4.1 in four different postures

weight, and skin fold thickness. The histograms of all the parameters are plotted in Fig. 4.4. Due to the specific identity of the subjects (teachers and students), the general population composition of the subjects were different from the population composition in ordinary society. 69% of the subjects were below 25 years old and 70% of the subjects are male.

## 4.3 The skin fold thickness formula for evaluating body fat percentage

Different from previous researches on the human body ACS, we take the skin fold measurement into account. In general anthropometric studies, the skin fold thickness is a variable that had often been investigated. The skin fold thickness (SFT) was found to be correlated to the body density (BD) from which the body fat percentage (BFP) can be extracted.

One of the most famous study was conducted by Jackson and Pollock who measured the body density of 403 male subjects between 18 and 61 years old [77]. Form the 403 subjects, 308 subjects were selected for inducting the skin fold equation of predicting body density, while the rest of 95 subjects were used for the cross validation of the inducted equation. The body density is measured by under water weighting method in which the body volume is extracted by weighting the subject's body submerged in a water tank [78]. Similar study was conducted by Jackson and Pollock on 283 female subjects and a skin fold equation for estimating the female body density was given [79]. Finally, the BD can be converted to the BFP by Siri's equation [80]:

$$\mathrm{BFP}(\%) = \frac{495}{\mathrm{BD}} - 450; \tag{4.2}$$

The unit of BD is grams/cc.

Jackson and Pollock have pointed out in their research that the SFT

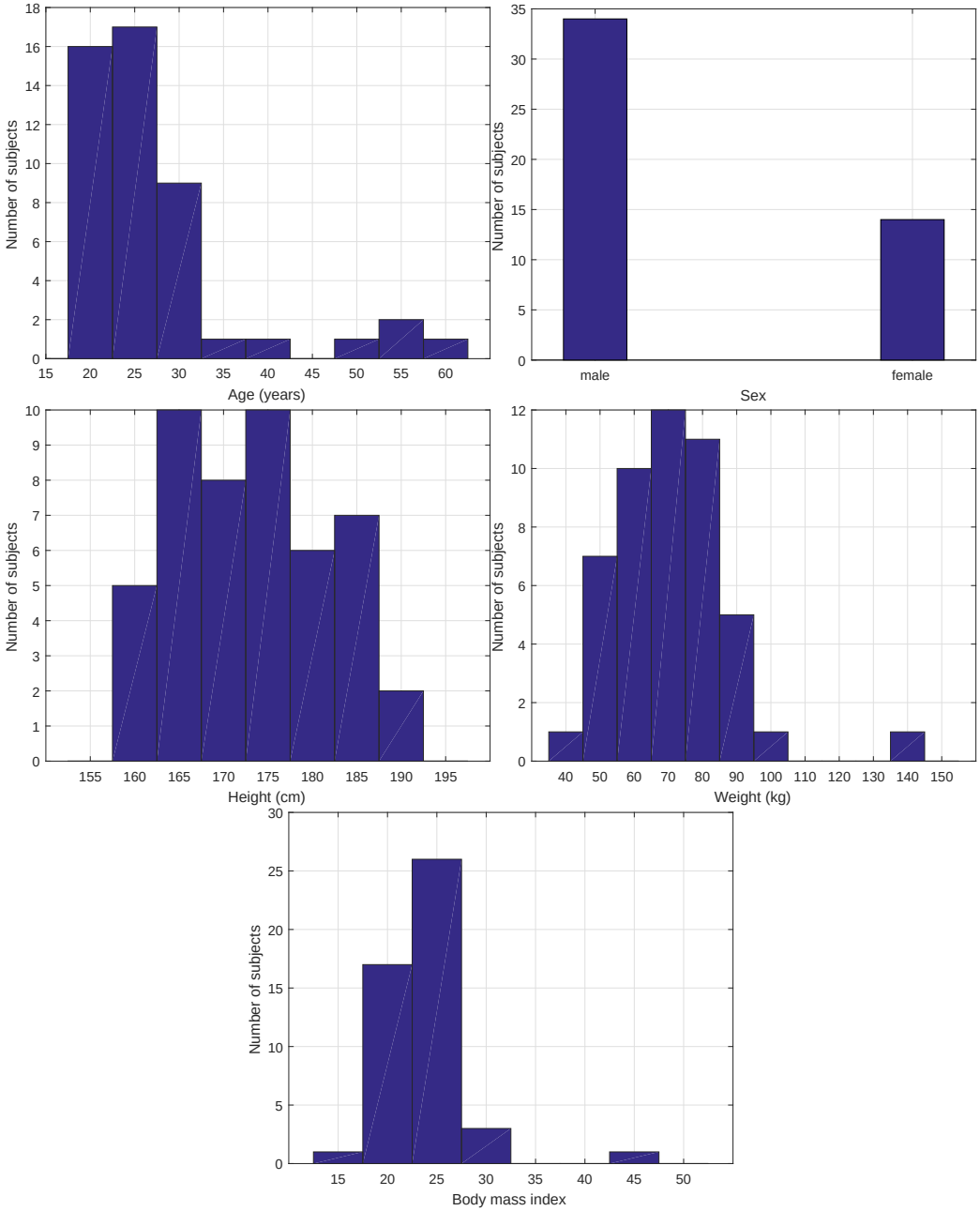


Figure 4.4: The population composition of 48 subjects under test

| | Equation name | Equation | Skin fold sites |
|---|---|---|---|
| #1 | 2 Site (M) [82] | $\text{BD} = c_1 - m_1 \log_{10} S$ | Triceps, Suprailium |
| #2 | 2 Site (F) [82] | $\text{BD} = c_2 - m_2 \log_{10} S$ | Triceps, Suprailium |
| #3 | 4 Site (M) [83] | $\text{BFP}(\%) = 0.29288S - 0.0005S^2 + 0.1585Y - 5.76377$ | Triceps,Suprailium, Abdominal, Thigh |
| #4 | 4 Site (F) [83] | $\text{BFP}(\%) = 0.29669S - 0.00043S^2 + 0.02963Y + 1.4072$ | Triceps,Suprailium, Abdominal, Thigh |

Table 4.1: The SFT equations for estimating BFP and BD. $S$ denotes the sum of all skin folds in mm. $Y$ is age in years. BD is body density in grams/cc. $(M)$ means male. $(F)$ means female. The parameters of SFT equation #1 and #2 were listed in Table 4.2 and Table 4.3

tend to give more accurate estimation on the BD than the height-weight ratio, but they also mention the empirical SFT equations were population specified. False using SFT equations to estimate BD of wrong population groups would cause error [78]. Such points have been proved by Nevill who had given an empirical SFT formula specially for obese subject, while Jackson and Pollock's formula tend to underestimate the BFP by 1% [81].

The SFT equations used in this thesis were given in Table 4.1. The two site SFT equations is for those subjects whose skin over thighs are too tight to pinch .

| Age | 17 to 19 | 20 to 29 | 30 to 39 | 40 to 49 | $\geq 50$ |
|---|---|---|---|---|---|
| $c_1$ | 1.1370 | 1.1362 | 1.1273 | 1.1383 | 1.1415 |
| $m_1$ | 0.0545 | 0.0538 | 0.0531 | 0.0660 | 0.0718 |

Table 4.2: the $c_1$ and $m_1$ value for male subjects

| Age | 17 to 19 | 20 to 29 | 30 to 39 | 40 to 49 | $\geq 50$ |
|---|---|---|---|---|---|
| $c_2$ | 1.1311 | 1.1377 | 1.1281 | 1.1198 | 1.1158 |
| $m_2$ | 0.0624 | 0.0684 | 0.0644 | 0.0630 | 0.0635 |

Table 4.3: the $c_1$ and $m_1$ value for female subjects

## 4.4 The skin fold measurement techniques

In our research, we use the skin fold techniques introduced in the international standard of anthropometric assessment [84]. The caliper we used is the slim guide calliper whose measurement range is 0-80 mm. The pinch sites were chosen at triceps, abdominal wall, suprailium, and mid thigh. One skin fold reading at each site was obtained consecutively, and the four readings was repeated for three rounds. This order of measurement reduces the measurement error introduced by repeatedly pinching at an inaccurate position.

Here is a brief on how the pinching sites were selected [84].

1. Triceps: The subject was standing with right arm relaxed. The mid point was marked between the Acromiale and the Radiale. The pinching site is at the most posterior point of right arm and the site has the same height as the mid mark. The skin is pinched vertically.

2. Abdominal: The subject is standing facing towards the experimenter. The pinching site is at 5 cm to the right side of the navel. The skin is pinched vertically.

3. Suprailium: The subject was standing with the right arm slightly raised. The site is right above the iliocristale. The pinching is done by grasping the skin with sufficiently opened the thumb and index, and the pinching direction follows the natural fold of the skin.

4. Thigh: The subject is seated on a stool with the right feet rest on the ground. The mid point between the Inguinal fold and anterior patella is selected as the pinching site. The skin is pinched along the mid line of the thigh.

The anthropometric result of 48 subjects is listed in Table 4.4.

To validate the skin fold techniques, the BFP calculated by SFT were compared to the BFP calculated by the body mass index (BMI) [85]. The

| N | G | E | Y | H | W | SF1 | SF2 | SF3 | SF4 |
|---|---|---|---|---|---|---|---|---|---|
| 1 | M | Non-Asian | 49 | 160 | 70.3 | 23.3 | 21.0 | N/A | 15.3 |
| 2 | M | Non-Asian | 58 | 175 | 76.5 | 29.0 | 19.3 | 13.0 | 22.7 |
| 3 | M | Non-Asian | 53 | 188 | 99.4 | 27.7 | 18.0 | 21.7 | 24.0 |
| 4 | M | Asian | 28 | 183 | 79.6 | 29.3 | 19.7 | N/A | 22.3 |
| 5 | F | Non-Asian | 55 | 165 | 61.6 | 18.0 | 15.0 | N/A | 18.0 |
| 6 | F | Non-Asian | 29 | 166 | 55.3 | 19.0 | 16.0 | 24.0 | 27.7 |
| 7 | F | Asian | 28 | 166 | 56.6 | 24.0 | 14.7 | 19.7 | 25.3 |
| 8 | F | Asian | 28 | 166 | 54.9 | 20.7 | 14.3 | 18.7 | 19.7 |
| 9 | M | Asian | 26 | 178 | 64.3 | 21.3 | 14.0 | 18.3 | 23.0 |
| 10 | M | Asian | 29 | 180 | 84.5 | 28.0 | 16.3 | 17.3 | 24.3 |
| 11 | M | Non-Asian | 24 | 190 | 91.6 | 27.0 | 16.0 | 23.3 | 21.0 |
| 12 | M | Asian | 22 | 168 | 66.4 | 19.0 | 12.3 | 18.0 | 19.7 |
| 13 | M | Non-Asian | 20 | 173 | 70.3 | 23.0 | 13.0 | 13.7 | 28.3 |
| 14 | M | Non-Asian | 21 | 185 | 64.6 | 9.3 | 7.3 | 9.0 | 12.7 |
| 15 | M | Asian | 22 | 183 | 81.4 | 27.7 | 22.7 | 24.7 | 39.3 |
| 16 | M | Asian | 24 | 181 | 84.5 | 30.7 | 15.7 | 27.0 | 29.3 |
| 17 | M | Asian | 24 | 169 | 63.2 | 26.0 | 18.0 | 17.0 | 28.7 |
| 18 | M | Asian | 28 | 166 | 68.5 | 15.7 | 11.7 | 12.7 | 13.7 |
| 19 | M | Asian | 35 | 169 | 52.6 | 8.3 | 6.0 | 11.0 | 12.0 |
| 20 | F | Non-Asian | 23 | 160 | 43.5 | 6.8 | 12.0 | 20.2 | 6.3 |
| 21 | M | Asian | 24 | 186.4 | 86.5 | 18.3 | 16.0 | 13.3 | 15.3 |
| 22 | M | Non-Asian | 24 | 176 | 70.2 | 9.0 | 5.7 | 6.7 | 7.7 |
| 23 | M | Non-Asian | 19 | 171 | 57.7 | 10.3 | 10.3 | 13.0 | 12.3 |
| 24 | M | Non-Asian | 24 | 180 | 73.6 | 16.0 | 9.3 | 8.7 | 11.7 |
| 25 | M | Asian | 25 | 175 | 81.5 | 14.3 | 11.7 | 13.7 | 16.0 |
| 26 | M | Non-Asian | 28 | 173 | 69.7 | 23.0 | 15.3 | 15.7 | 20.7 |
| 27 | M | Non-Asian | 20 | 164 | 68.7 | 18.0 | 9.3 | 17.0 | 17.3 |
| 28 | M | Non-Asian | 20 | 185 | 86.2 | 24.3 | 16.3 | 14.0 | 23.7 |
| 29 | M | Asian | 28 | 180 | 81.4 | 25.7 | 17.0 | 25.7 | 28.0 |
| 30 | F | Non-Asian | 22 | 168 | 63.3 | 13.0 | 26.7 | N/A | 16.7 |
| 31 | M | Non-Asian | 22 | 164 | 54.2 | 7.7 | 5.0 | 4.0 | 9.0 |
| 32 | M | Non-Asian | 23 | 170 | 79.6 | 31.0 | 16.7 | 27.0 | 34.0 |
| 33 | M | Non-Asian | 25 | 177 | 71.9 | 11.7 | 7.0 | 6.0 | 14.3 |
| 34 | M | Non-Asian | 21 | 174 | 142.4 | 46.0 | 38.0 | 54.7 | 70.0 |
| 35 | M | Non-Asian | 21 | 186 | 75.9 | 18.3 | 15.7 | 16.3 | 16.7 |
| 36 | F | Non-Asian | 19 | 164 | 72.3 | 30.7 | 30.3 | 45.3 | 34.3 |

| N | G | E | Y | H | W | SF1 | SF2 | SF3 | SF4 |
|---|---|---|---|---|---|---|---|---|---|
| 37 | F | Asian | 20 | 158 | 48 | 13.0 | 15.7 | 16.3 | 14.3 |
| 38 | M | Non-Asian | 22 | 178 | 69.6 | 9.3 | 6.0 | 7.7 | 10.7 |
| 39 | M | Asian | 24 | 176 | 72.2 | 23.3 | 9.7 | 11.7 | 21.3 |
| 40 | M | Non-Asian | 19 | 176 | 87.3 | 25.7 | 16.0 | 22.0 | 25.7 |
| 41 | F | Asian | 25 | 169 | 54.2 | 8.7 | 19.0 | 16.7 | 15.0 |
| 42 | M | Asian | 24 | 176 | 80.5 | 30.0 | 13.7 | 15.7 | 33.0 |
| 43 | F | Asian | 23 | 161 | 53.3 | 13.3 | 20.0 | N/A | 17.0 |
| 44 | M | Non-Asian | 42 | 187 | 91.9 | 28.3 | 16.3 | 15.0 | 26.7 |
| 45 | F | Non-Asian | 24 | 167 | 53.3 | 21.7 | 21.0 | N/A | 25.7 |
| 46 | F | Asian | 28 | 163 | 60.7 | 15.3 | 21.0 | 32.0 | 29.7 |
| 47 | F | Asian | 19 | 160 | 47.7 | 6.0 | 14.7 | 21.0 | 7.7 |
| 48 | F | Non-Asian | 27 | 170 | 78.9 | 29.7 | 34.0 | 53.7 | 41.0 |

Table 4.4: The morphological parameters of 48 subjects. 'N': Subject number, 'G': Gender, 'F': Female, 'M': Male, 'E': Ethics, 'Y': Age in years, 'H': Height in cm, 'W': Weight in kg, 'SF1': Skin fold at abdominal site in mm, 'SF2': Skin fold at tricep site in mm, 'SF3': Skin fold at thigh site in mm, 'SF4': Skin fold at supraillium site in mm, 'N/A': the skin over thigh is too tight to measure the skin fold.

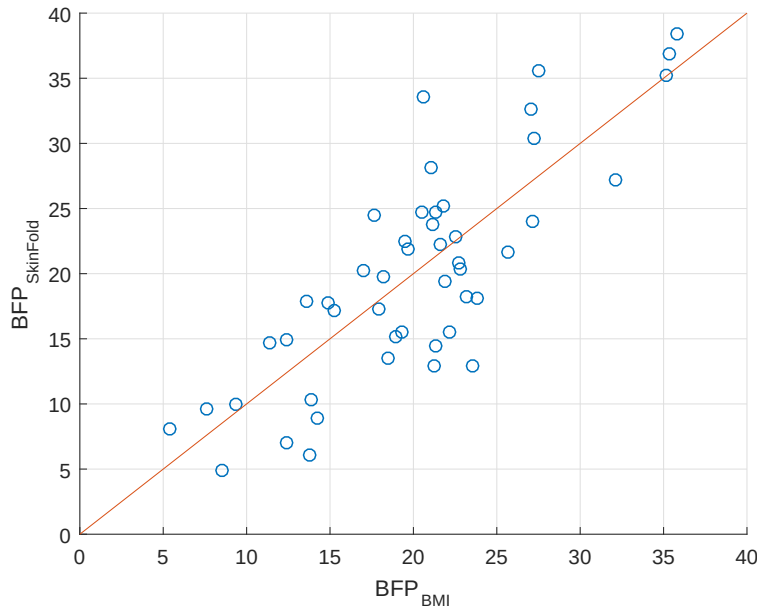


Figure 4.5: BFP calculated by empirical SFT equation vs. BFP calculate by BMI

following is the formulae for BFP calculated by BMI:

$$\mathrm{BFP} = 76.0 - \frac{1097.8}{\mathrm{BMI}} - 20.6G + 0.053Y + \frac{95.0E}{\mathrm{BMI}} - 0.044EY + \frac{154G}{\mathrm{BMI}} + 0.034GY \quad (4.3)$$

where 'G' is gender (1 for male, 0 for female), 'E' is ethnicity (1 for Asian, 0 for non-Asian), 'Y' is age in years, BMI is the body mass index which is defined as the ratio between body weight and height squared.

The BFP calculated by SFT equation and the BFP calculated by BMI is compared in Fig. 4.5 in which a strong linear correlation can be found. The correlation coefficient is 0.81.

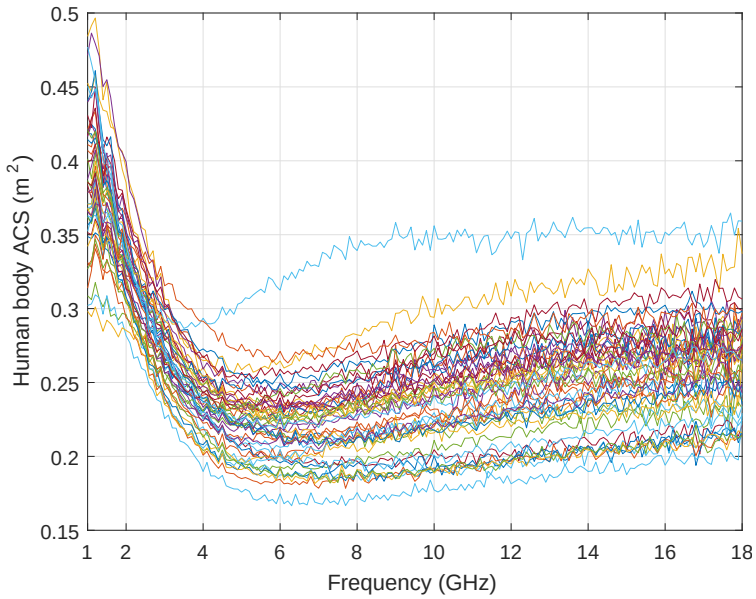


Figure 4.6: The overview of the ACS of human body. The outlier belongs to the subject with very high BMI, which is 47.0kg/m$^2$, while the average BMI of the rest of the subjects is 23.2kg/m$^2$

## 4.5 The human ACS measurement result

The measurement setups demonstrated in Sec. 4.1 were used for the measurement of all 48 human body ACS. Win #1 were used to extract the human body ACS from $S_{21}$. An overview of all ACS results were plotted in Fig. 4.6. The measured human ACS of this research are very close to the human body ACS measured by Melia [76], but with more detail. The highest ACS of each subject is at about 1 GHz, and the minimum value of each subject's ACS is between 4 - 6 GHz, then the ACS of each subject slightly goes up as the frequency raises over 6 GHz.

As shown in Fig. 4.2, the less stretched posture tend to give smaller ACS and the ACS curve shifts up and down as the posture changes. However, the effect of morphological parameters on ACS is more complicated. To

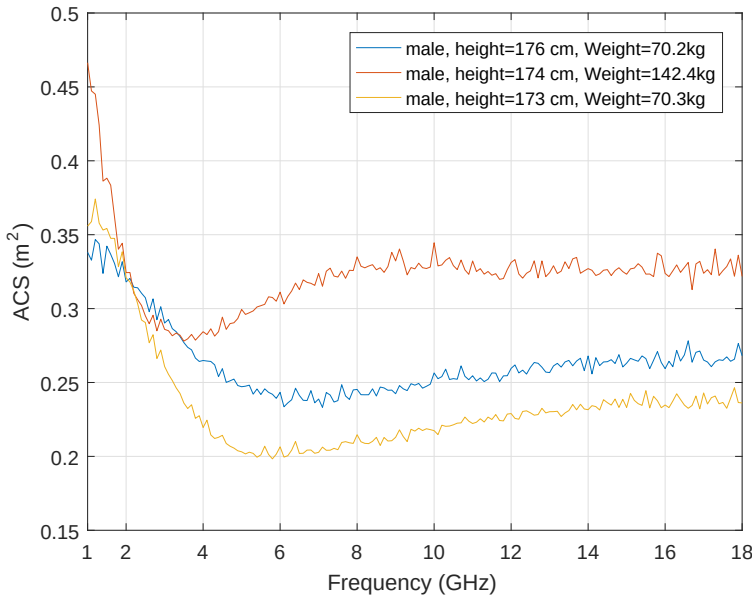


Figure 4.7: the ACS of subjects with maximum, mean, and minimum skin fold readings

demonstrate the problem, the ACS of three subjects with maximum, mean and minimum SFT is plotted in Fig. 4.7. The figure shows the effect of SFT is not simply shifting the ACS up and down. The shape of the ACS curve changes as the SFT changes.

According to Melia's research , the body surface area (BSA) is a morphological parameter that correlates well with the ACS over most of the frequencies, therefore BSA was also put into study in our research on ACS [76]. The BSA is evaluated by the empirical formula [86, 76]:

$$\begin{cases} \text{BSA} = 128.1W^{0.44}H^{0.60} & \text{(men)} \\ \text{BSA} = 147.1W^{0.47}H^{0.55} & \text{(women)} \end{cases} \tag{4.4}$$

Where $W$ is body weight in kg. $H$ is height in cm. This formula is given by Tikuisis who conducted BSA measurements on 641 adults by laser scanning

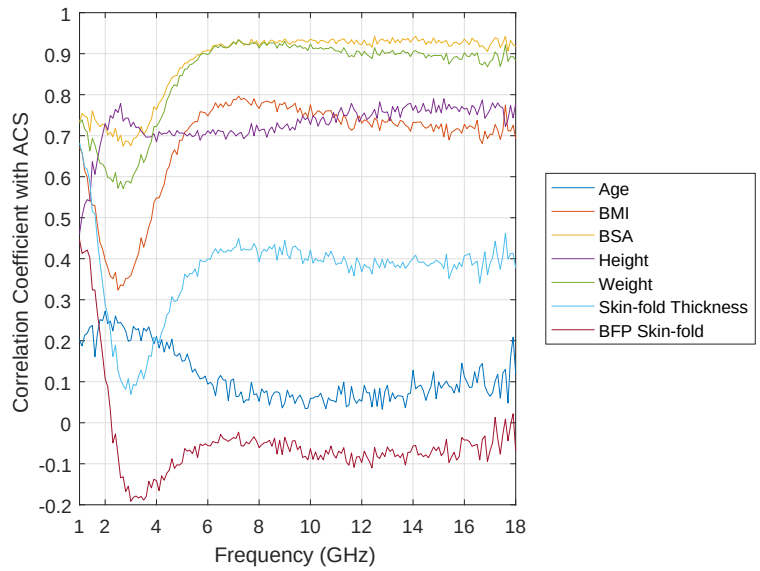


Figure 4.8: The correlation coefficient between human body ACS and morphological parameters at different frequencies

[86]. Equation 4.4 has an overall RMS error of 1.26%.

The correlation coefficient between measured ACS and all morphological parameters over different frequencies were plotted in Fig. 4.8. A very strong correlation between ACS and BSA can be observed above 6 GHz in Fig. 4.8, which can be explained by the study of power distribution in each layer of the planar model shown in Sec. 2.2. The study of planar model in Sec. 2.2 shows the skin layer absorbs the most percentage of power above 5 GHz no matter how thick the fat layer is. Fig. 4.8 shows the correlation coefficient between the ACS and the BSA reaches above 0.9 from 6 GHz to 18 GHz. Therefore the ACS above 6 GHz can be modelled by a linear function of BSA:

$$< \sigma_a(f) >= C_1(f)\text{BSA} + C_2(f) \tag{4.5}$$

Where $C_1$ and $C_2$ are the frequency dependent coefficients. BSA is in $m^2$. The linear regressions were performed at different frequencies and the value

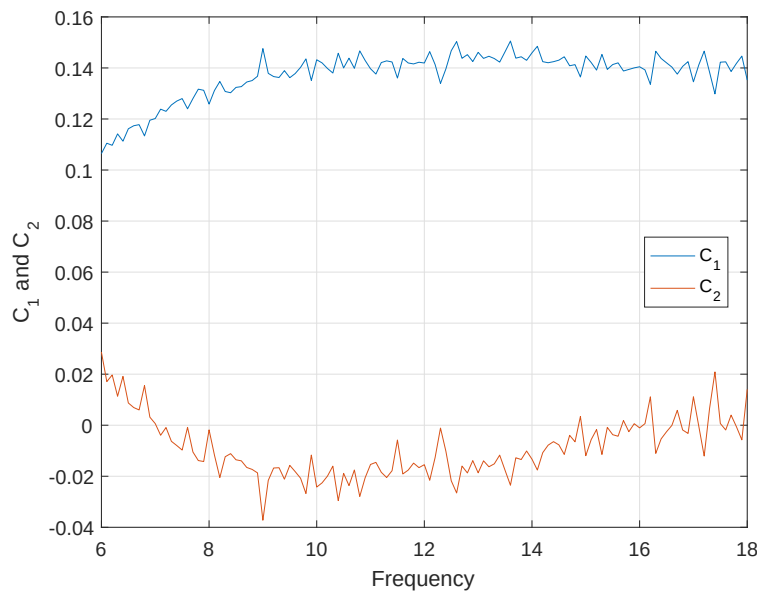


Figure 4.9: The coefficient of linear ACS model from 6 GHz to 18 GHz

of $C_1(f)$ and $C_2(f)$ were plotted in Fig. 4.9. The quality of regression is quantified by $R^2$ which is plotted in Fig. 4.10 [87].

Fig. 4.9 proves the skin absorbs most of the power by showing the values of $C_2$ are close to zero from 6 GHz to 18 GHz. This corresponds with the physical concept that a lossy object with zero surface area have zero ACS. On the other hand, the $R^2 > 0.8$ from 6 GHz to 18 GHz shows the linear model gives a good evaluation on the ACS.

Considering the BSA dominates the ACS at high frequency, the ACS is normalized by the BSA to study the effect of other morphological parameters on non-ionizing dosimetry:

$$< \xi >= \frac{< \sigma_a >}{A_s} = \frac{\sigma_a}{0.25\text{BSA}} \tag{4.6}$$

where $< \xi >$ denotes the averaged absorption coefficient of human body. $A_s$ is the averaged silhouette area of human body. Here the value of $A_s$ was

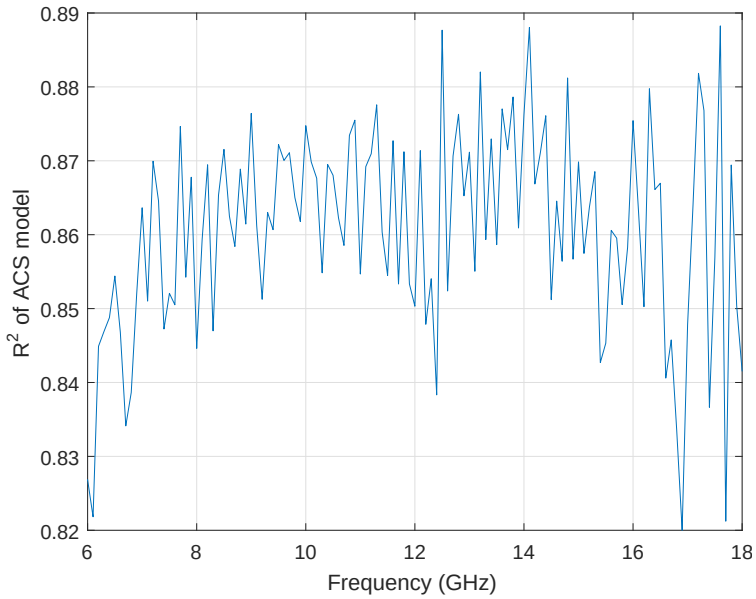


Figure 4.10: $R^2$ of linear ACS model

chosen as 0.25BSA by assuming the human body is a perfect convex object. An overview of the $< \xi >$ of all human subjects are shown in Fig. 4.11.

The $< \xi >$ value is around 0.8 - 0.9 at 1 GHz. The $< \xi >$ quickly decrease as the frequency rises until at around 6 GHz its value start to increase very gently with frequency. The value of $< \xi >$ above 6 GHz is distributed between 0.45 - 0.65 for all subjects, which is slightly higher than the values reported in [76]. The reason might be the different selection of poses in our study. We chose the 'Layed-Star' pose in Fig. 4.1 for all the ACS measurements while in [76] the 'Sitted 1' pose was chosen.

The correlation coefficients between $< \xi >$ and all morphological parameters was also calculated. The results are shown in Fig. 4.12. It can be seen that almost every morphological parameters lose the correlation with the $< \xi >$. The value of correlation coefficients are all between -0.5 and 0.25 above 6 GHz. Below 6 GHz, all the correlation coefficients seem to be unpredictable, but there are two frequencies that worth special notice.

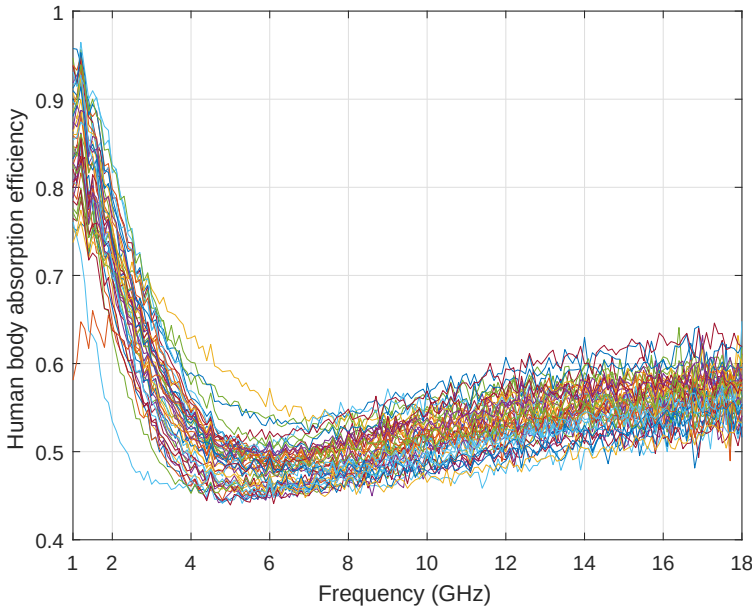


Figure 4.11: The overview of the absorption coefficient of human body

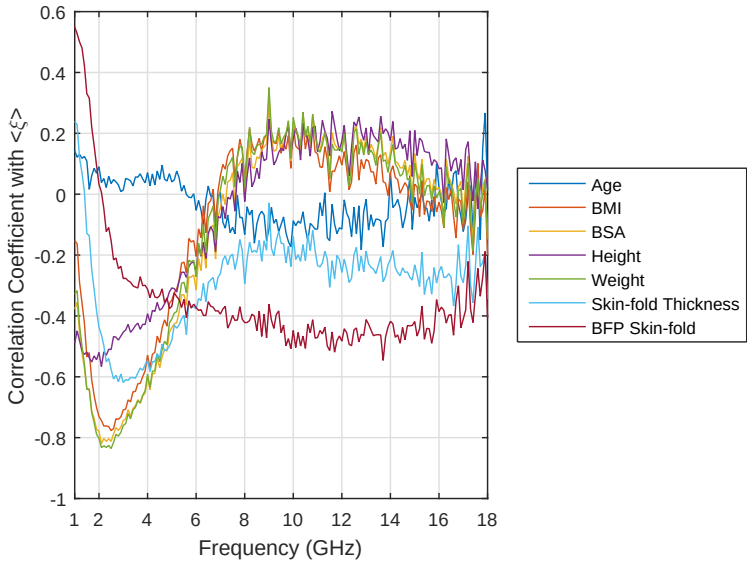


Figure 4.12: The correlation coefficient between human body absorption coefficient and morphological parameters at different frequencies

| Morphological Parameters | $C_3$ | $C_4$ | R |
|---|---|---|---|
| BMI (kg/m$^2$) | $-9.192 \times 10^{-3}$ | 0.8758 | $-0.7767$ |
| Weight (kg) | $-7.473 \times 10^{-3}$ | 0.7156 | $-0.8357$ |
| SFT (mm) | $-2.674 \times 10^{-3}$ | 0.8492 | $-0.5755$ |
| BSA (m$^2$) | $-0.198$ | 1.02 | $-0.8122$ |

Table 4.5: Linear relations between $\xi$ and morphological parameters at 2.5 GHz

The first frequency is 2.5 GHz. The $< \xi >$ shows a very strong negative linear correlation with BMI, Weight, BSA, and BFP. Similar results were also reported by Melia [76], but in Melia's research, the correlation coefficient is only calculated at 3 GHz. This negative correlation of $< \xi >$ to the morphological parameters might be explained by the resonant effect of fat layer shown in Sec. 2.2. $< \xi >$ is correlated to the morphological parameter by the following equation:

$$< \xi(2.5\text{GHz}) >= C_3\text{Morph} + C_4 \tag{4.7}$$

where 'Morph' means morphological parameters. It can be BMI, weight, SFT, BSA in this equation; $C_3$ and $C_4$ are constants which will vary with different morphological parameters. The values of $C_3$ and $C_4$ are given in Tab. 4.5.

The second frequency worth noticing is 1 GHz. At 1 GHz in Fig. 4.12, the $< \xi >$ shows almost no correlations with any morphological parameters except the BFP calculated from skin fold. This may also be the effect of resonance due to the average fat layer thickness of human body.

In general, the modelling of non-ionizing dosimetry can be separated into two different regions. The first region is from 1 GHz to 6 GHz, in which both the ACS and $< \xi >$ show very vague linear correlation with all morphological parameters, as can be seen from Fig. 4.8 and Fig. 4.12. The second region

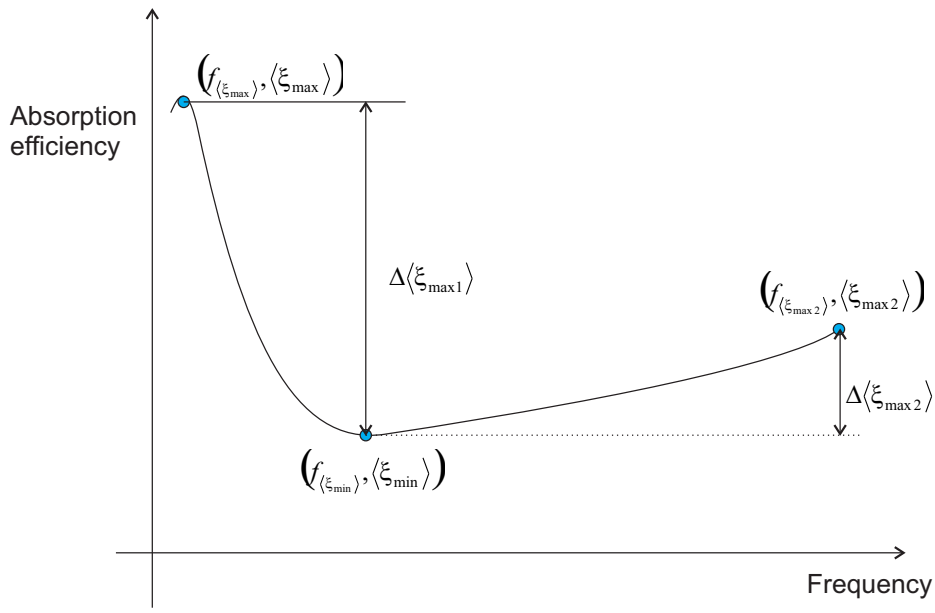


Figure 4.13: Features of absorption coefficient

is from 6 GHz to 18 GHz, in which the BSA have the most prevailing effect on the ACS, which is shown in Fig. 4.8.

## 4.6 Simple predictors of human body ACS

According to Fig. 4.11, the absorption coefficient $< \xi >$ of Human body generally follows a shape demonstrated in Fig. 4.13.

In the figure, the feature of the absorption coefficient is described by several simple predictors on it. The meaning of these simple predictors are:

$(f_{<\xi_{max}>}, < \xi_{max} >)$: The coordinate of the maximum absorption coefficient point. Since the measured absorption coefficient is not a smoothed curve, the polynomial fit of order 5 was conducted from 1 GHz to 2 GHz, and the maximum point was picked up from the polynomial model.

$(f_{<\xi_{min}>}, < \xi_{min} >)$: The coordinate of the minimum absorption coefficient point. Polynomial fit of order 5 was performed on the measured absorption

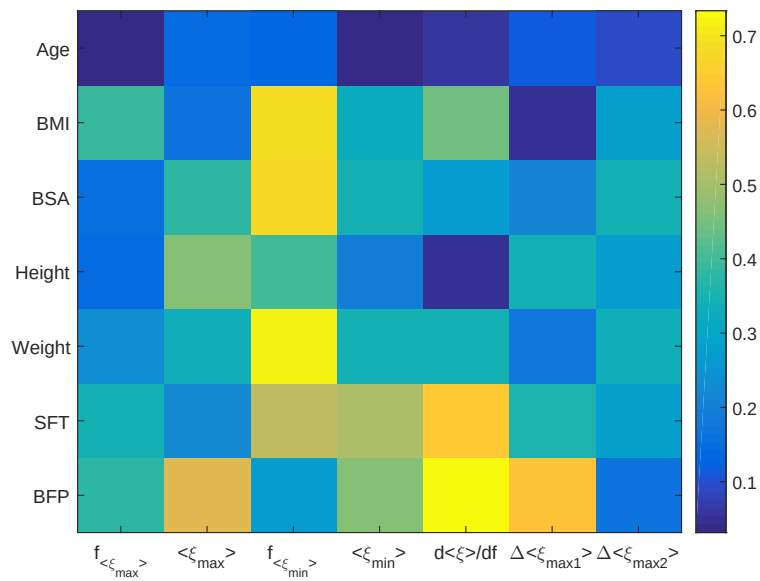


Figure 4.14: The absolute value of correlation coefficient between simple predictors and morphological parameters

coefficient from 1 GHz to 12 GHz, and the minimum point was extracted from the polynomial model.

$\Delta < \xi_{\text{max1}} >$ and $\Delta < \xi_{\text{max2}} >$: As shown in Fig. 4.13.

$\left.\frac{\mathrm{d}<\xi>}{\mathrm{d}f}\right|_{<\xi>=0.5(<\xi_{\text{max}}>+<\xi_{\text{min}}>)}$: Derivative of absorption coefficient at point where $< \xi >= 0.5(< \xi_{\text{max}} > + < \xi_{\text{min}} >)$. The derivative was calculated from the polynomial model which is obtained from the 5th order polynomial fitting $< \xi >$ from $< f_{\text{min}} >$ to $< f_{\text{min}} >$

After all the simple predictors on $< \xi(f) >$ had been defined, the linear correlation between simple predictors and morphological parameters were calculated. The results were shown in Fig. 4.14 and Table 4.6.

In Table 4.6, we consider the 'highly correlated parameters' as the pair of parameters whose correlation coefficient higher than 0.5, then there are nine pairs of highly correlated parameters. They are: 1. BMI v.s. $f_{<\xi_{\text{min}}>}$, 2. BSA v.s. $f_{<\xi_{\text{min}}>}$, 3. Weight v.s. $f_{<\xi_{\text{min}}>}$, 4. Fat thickness v.s. $f_{<\xi_{\text{min}}>}$, 5. SFT v.s.

| / | $f_{<\xi_{max}>}$ | $<\xi_{max}>$ | $f_{<\xi_{min}>}$ | $<\xi_{min}>$ | $\frac{d<\xi>}{df}$ | $\Delta<\xi_{max1}>$ | $\Delta<\xi_{max2}>$ |
|---|---|---|---|---|---|---|---|
| Age | -0.0346 | 0.1428 | 0.1406 | 0.0316 | -0.0638 | 0.1131 | 0.0947 |
| BMI | -0.3842 | -0.1731 | **-0.6804** | -0.3277 | -0.4399 | 0.0487 | 0.2765 |
| BSA | -0.1605 | -0.3717 | **-0.6762** | -0.3452 | -0.2683 | -0.2141 | 0.3388 |
| Height | 0.1475 | -0.4651 | -0.3991 | -0.1897 | 0.0488 | -0.3419 | 0.2629 |
| Weight | -0.2350 | -0.3304 | **-0.7165** | -0.3493 | -0.3405 | -0.1774 | 0.3372 |
| SFT | -0.3472 | 0.2281 | **-0.5312** | **-0.5061** | **-0.6386** | 0.3507 | 0.2736 |
| BFP | -0.2220 | **0.5610** | -0.1722 | -0.4363 | **-0.6394** | **0.6156** | 0.1038 |

Table 4.6: Correlation coefficient between simple predictors and morphological parameters, the parameters in bold font are the correlation coefficients whose absolute value higher than 0.5

$<\xi_{min}>$, 6. SFT vs $\frac{d<\xi>}{df}$, 7. BFP v.s. $<\xi_{max}>$, 8. BFP v.s. $\frac{d<\xi>}{df}$, 9.BFP v.s. $\Delta<\xi_{max1}>$. However, among these 9 pairs of parameters, there is not a single pair whose absolute value of correlation coefficient exceeds 0.7.

The nine pairs of parameters can be divided into 3 groups. The first group includes the parameter pairs involving BMI, BSA and weight. The second group includes the parameter pairs involving BFP. The third group includes parameter pairs involving fat layer thickness. The reasons are as follows.

As discussed in Sec. 4.2, the morphological parameters of subjects are not totally randomized. For instance in group one, BMI, BSA are all evaluated from empirical functions of weight therefore the correlation coefficients in group one are likely to give similar conclusion. The rest of the six pairs of parameters was divided into two groups because the relation between the BFP and the SFT is not linear.

The 9 linear regressions of simple predictors against morphological parameters are plotted in Fig. 4.15, Fig. 4.16 and Fig. 4.17.

The coefficients of 9 linear regressions are given in the legend of each figure. The formulas of evaluating simple predictors are:

$$y = ax + b \tag{4.8}$$

where $y$ denotes the simple predictors. $x$ denotes the morphological parameters. $a$ and $b$ are constants given in the legend.

Firstly, a negative correlation was observed between $f_{<\xi_{\min}>}$ and the body weight dominated parameters such as BMI, BSA. Such a negative correlation was also observed between $f_{<\xi_{\min}>}$ and SFT. Both of these two facts correspond with the properties of the three layer spherical model whose resonant frequencies shift to lower frequencies as the fat layer thickness increases.

On the other hand, $< \xi_{\min} >$ is also decreasing along with the increase of SFT. $< \xi_{\max} >$ and $\Delta < \xi_{\max 1} >$ are slightly increasing as the BFP goes up. This fact can be observed in the change of the spherical models' $< \xi_{\max} >$ and $\Delta < \xi_{\max 1} >$ as the fat layer thickness of the sphere model goes up, which is shown in Fig. 2.13.

Generally, the linear model of simple predictor only serves as a quantified indicator of abortion efficiency. Even though the absorption coefficient from 1 GHz to 6 GHz is very unpredictable, such a method is still useful in the quick evaluation of absorption coefficient of human body. The weak point of the simple predictors is there is no physical explanation for the model.

## 4.7 Expansion of human body absorption coefficient into series of models absorption coefficient

In this section, we will demonstrate the method of mapping human body absorption coefficient $< \xi >$ to the surface layer thickness of human body.

The surface layer thickness of human body is defined as the summation of fat layer thickness and skin layer thickness.

As shown in Sec. 3.11, the shell thickness can be extracted from the measured ACS of the sphere model by the GA. Since similarities are observed

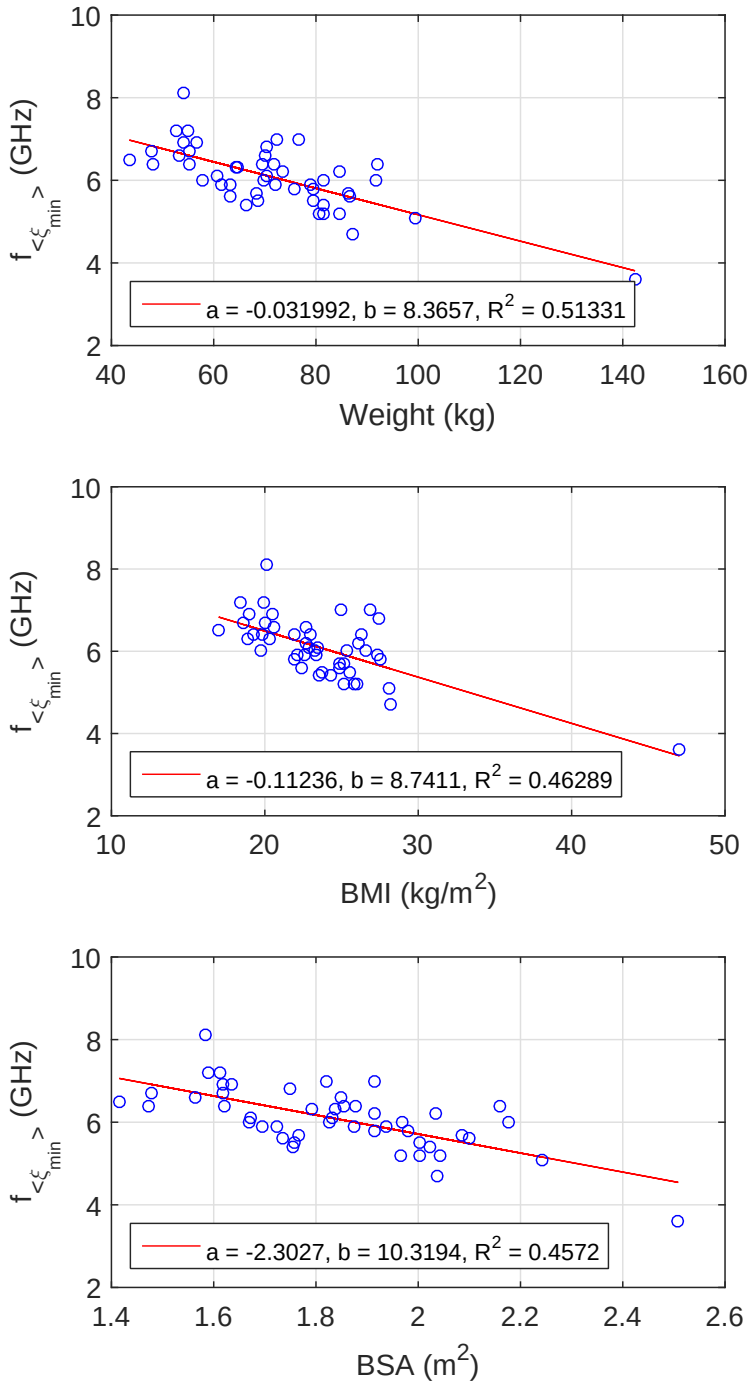


Figure 4.15: The linear regression of simple predictors

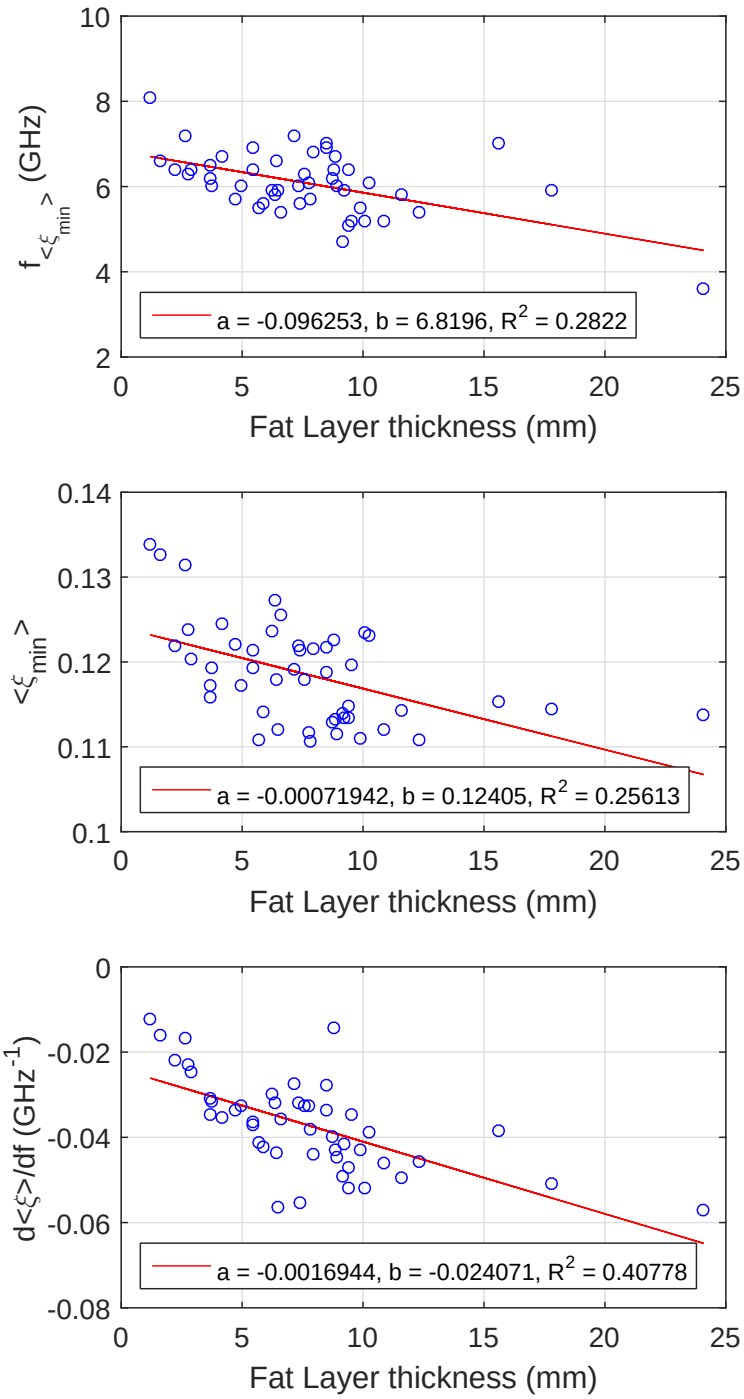


Figure 4.16: The linear regression of simple predictors

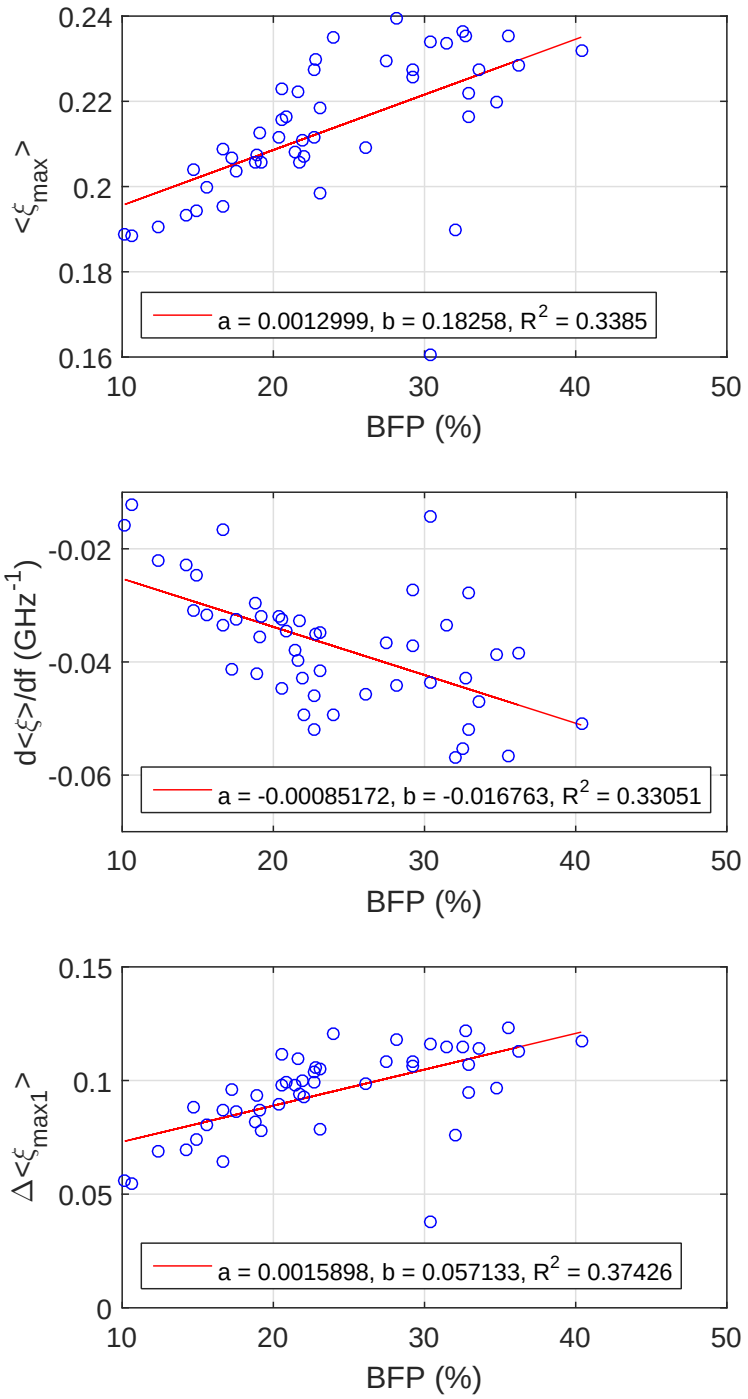


Figure 4.17: The linear regression of simple predictors

between the measured human bodies' absorption coefficient '$< \xi_{\text{body}} >$' and the absorption coefficient of the multilayer spherical model '$< \xi_{\text{sphere}} >$' in Sec. 4.6, especially at 1 GHz, both '$< \xi_{\text{body}} >$' and '$< \xi_{\text{sphere}} >$' are high. We can try to expand the $< \xi_{\text{body}} >$ into a series of $< \xi_{\text{sphere}} >$ with different fat layer thickness and skin layer thickness.

To demonstrate the method of inverse mapping $< \xi_{\text{body}}(f) >$ to surface layer thickness, the following assumptions were made:

Firstly, the human body surface is divided into $N$ different partitions, and the area of each partition is $\alpha_i$. Therefore, the summation of all $\alpha_i$ is equal to the BSA:

$$\text{BSA} = \sum_{i=1}^{N} \alpha_i \tag{4.9}$$

In (4.6), the averaged silhouette area of human body is obtained by multiplying BSA with 0.25, so that:

$$S_{\text{silhouette}} = 0.25\text{BSA} = \sum_{i=1}^{N} 0.25\alpha_i \tag{4.10}$$

Where $S_{\text{silhouette}}$ is the averaged silhouette area of human body; $0.25\alpha_i$ is considered as the averaged silhouette area of the $i$th partition.

According to the definition of absorption coefficient given by (2.14) , the ACS of human body equals to the multiplication of absorption coefficient and the averaged total silhouette area:

$$< \sigma_{a,\text{body}} >= \sum_{i=1}^{N} 0.25\alpha_i < \xi_{\text{sphere},i} > \tag{4.11}$$

where $< \xi_{\text{sphere},i} >$ is the the absorption coefficient of the sphere model representing $i$th partition of human body surface. We assume the skin layer thickness and fat layer thickness of $i$th sphere model is equal to that of the

$i$th partition of human body surface.

Dividing both sides of (4.11) by BSA gives the absorption coefficient of human body:

$$< \xi_{\text{body}} >= \sum_{i=1}^{N} 0.25 \frac{\alpha_i}{\text{BSA}} < \xi_{\text{sphere},i} >= \sum_{i=1}^{N} \beta_i < \xi_{\text{sphere},i} > \tag{4.12}$$

where $\beta_i = 0.25 \frac{\alpha_i}{\text{BSA}}$. There might be other factors that would affect the value of $< \xi_{\text{body}} >$, such as the light clothes wearing by subjects, the small posture difference among the subjects, etc. We use one term 'c' as a rough representation of the effect of all those factors and add into (4.12), which gives the final form of the model of human body absorption coefficient:

$$< \xi_{\text{body}} >= \sum_{i=1}^{N} \beta_i < \xi_{\text{sphere},i} > +c \tag{4.13}$$

In this approach, we will use GA to find the values of $(\beta_1, \beta_2, ..., c)$ such that (4.13) is as close to the measured absorption coefficient as possible. The cost function of GA optimization is defined as the RMS difference between (4.13) and the measured absorption coefficient over different frequencies, which is

$$\text{minimize} \quad \text{RMS}\left(< \xi_{\text{body,meas}}(f) > - < \xi_{\text{body}}(f) > -c\right) \tag{4.14}$$

where $< \xi_{\text{body,meas}}(f) >$ is the measured absorption coefficient of a human subject.

According to the definition of $\beta_i$ in the (4.12), $\beta_i$ is proportional to the percentage of $\alpha_i$ in the BSA. Therefore, the averaged skin fold thickness can be evaluated from

$$\text{SFT} = \frac{2 \sum_{i=1}^{N} \beta_i (d_{\text{skin}_i} + d_{\text{fat}_i})}{\sum_{i=1}^{N} \beta_i} \tag{4.15}$$

where $d_{\text{skin}_i}$ and $d_{\text{fat}_i}$ are the skin layer thickness and fat layer thickness of the $i$th spherical model. The coefficient '2' in front of (4.15) is because the SFT is measured by pinching two layers of fat and skin. Equation (4.15) is twice the numerical average of surface layer thickness with weight $\alpha_i$.

The value of each $< \xi_{\text{sphere},i}(f) >$ should be evaluated from specific choices of fat layer thickness and skin layer thickness. The choices of fat layer thickness and skin layer thickness should not exceed the reasonable range. In our research, the range of fat layer thickness was chosen as $[0.5\,\text{mm}, 30.5\,\text{mm}]$ to make sure it covers all the results of skin fold measurements. The range of skin layer thickness was chosen from documented data. In Lee's research, biopsy techniques were applied on 452 Asian subjects over different body parts and the skin layer thickness is measured under a microscope [88]. The measurement shows the skin layer thickness range from 521 $\mu$m to 1977 $\mu$m around human body. Therefore the range of skin layer thickness chosen as $[0.5\,\text{mm}, 1.9\,\text{mm}]$. The radius of all spherical models in (4.13) was chosen to give the circumference equal to the waist size of the human subject under test. Since the waist size was not measured in the experiment, the waist size of each subject is calculated by the empirical formula [89]:

$$\begin{cases} d_{\text{circ}} = (\text{BMI} + 2.6)/0.307 \quad (\text{cm}) \quad \text{men} \\ d_{\text{circ}} = (\text{BMI} + 6.0)/0.394 \quad (\text{cm}) \quad \text{women} \end{cases} \tag{4.16}$$

where $d_{\text{circ}}$ is the waist size.

In summary, the optimization problem can be expressed as follow:

Determine the values of $\beta_i$ and $c$, which

$$\text{minimize} \quad \text{RMS}\left( < \xi_{\text{body,meas}}(f) > - \sum_{i=1}^{N} \beta_i < \xi_{\text{sphere},i}(f) > - c \right) \tag{4.17}$$

where $< \xi_{\text{body,meas}}(f) >$ is the measured averaged absorption coefficient of a

human subject. The optimized $\beta_i$ will be substitute into (4.15) to calculate the averaged skin fold thickness. Consider the definition of $\beta_i$, its value should be less than 1. The boundaries of $\beta_i$ and $c$ in GA optimization were set to be:

$$\begin{cases} \beta_i \in [0, 0.2] \\ c \in [0, 1] \end{cases} \tag{4.18}$$

The population size of GA optimization is 100, and the maximum generation size is set to be 50.

The value of $< \xi_{\text{sphere},i} >$ is calculated by choosing a particular set of values of ($d_{\text{skin},i}$, $d_{\text{fat},i}$, $\text{rad}_i$) from the following domain:

$$\begin{cases} d_{\text{skin,i}} \in \{[0.5,\ 1.9]\,\text{mm} \quad \text{step} \quad 0.2\,\text{mm}\} \\ d_{\text{fat,i}} \in \{[0.5,\ 30.5]\,\text{mm} \quad \text{step} \quad 5\,\text{mm}\} \\ \text{rad}_\text{i} = d_{\text{circ}}/2\pi \end{cases} \tag{4.19}$$

For instance in (4.19), $d_{\text{skin,i}}$ has 8 available choices; $d_{\text{fat,i}}$ has 6 available choices; $\text{rad}_i$ has 1 choice. $d_{\text{skin,i}}$, $d_{\text{fat,i}}$ and $\text{rad}_i$ have $8 \times 6 \times 1 = 48$ combinations from which 48 different $< \xi_{\text{sphere},i}(f) >$ can be obtained.

Here as an example, all the $< \xi_{\text{sphere},i}(f) >$ used for evaluating the surface layer thickness of subject No.1 is plotted in Fig. 4.18. The fitted absorption coefficient is shown in Fig. 4.19 It can be seen that the GA gives a very good fit. The RMS difference between the fitted curve and measurement data is 0.012.

The optimizations were then performed on the other 47 subjects. The SFT evaluated by GA were compared to the SFT measured by the calliper in Fig. 4.20. The values of minimized (4.17) is given in Fig. 4.21 which shows the fitted curves of all 48 subjects have less than 0.025 RMS difference to the corresponded measured absorption coefficient.

Since GA is a randomized optimization method, the output of GA is not

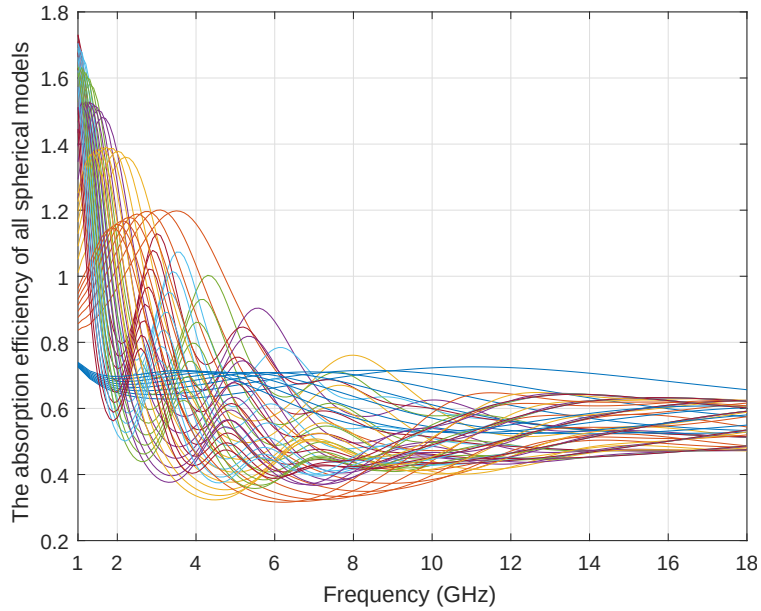


Figure 4.18: The basis functions for expanding absorption coefficient of Subject No. 1

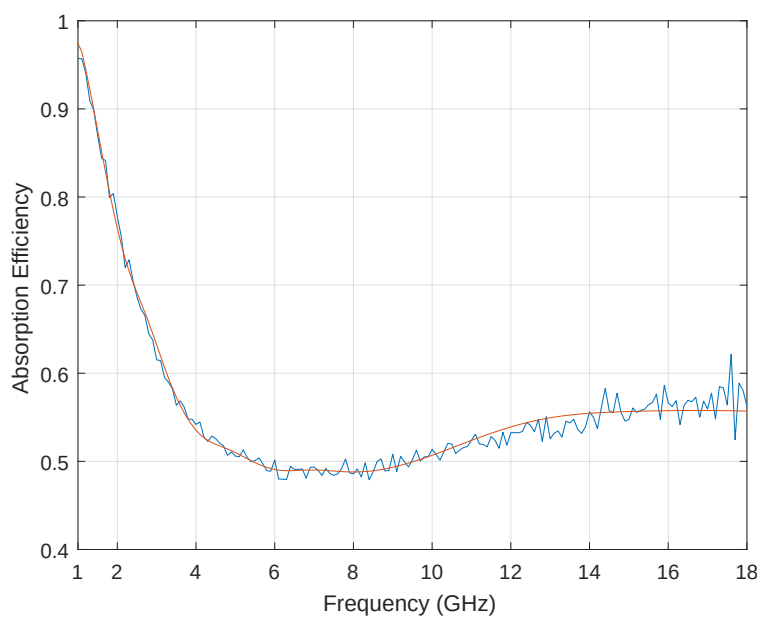


Figure 4.19: Fitting the absorption coefficient of Subject No.1 by genetic algorithm

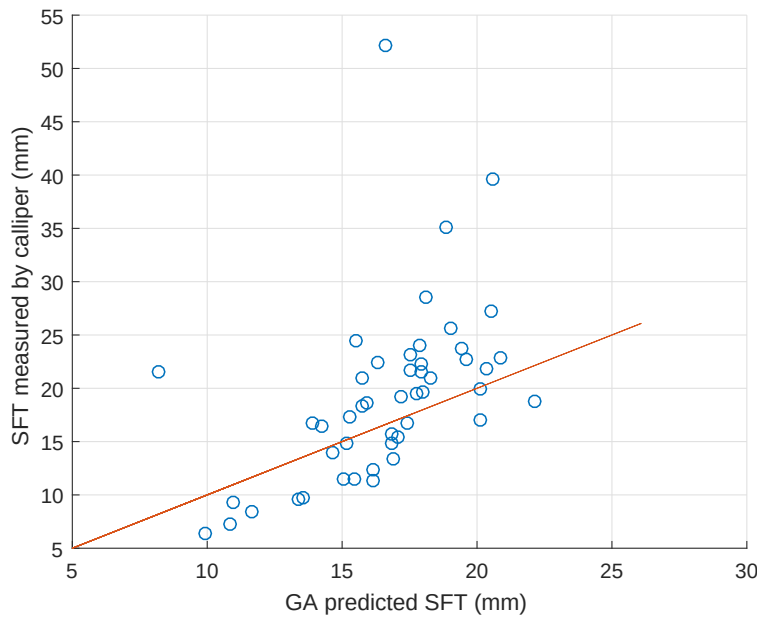


Figure 4.20: The GA predicted SFT vs. SFT measured by calliper, the red line is the reference line. The more accurate the GA prediction, the closer the dots to the reference line

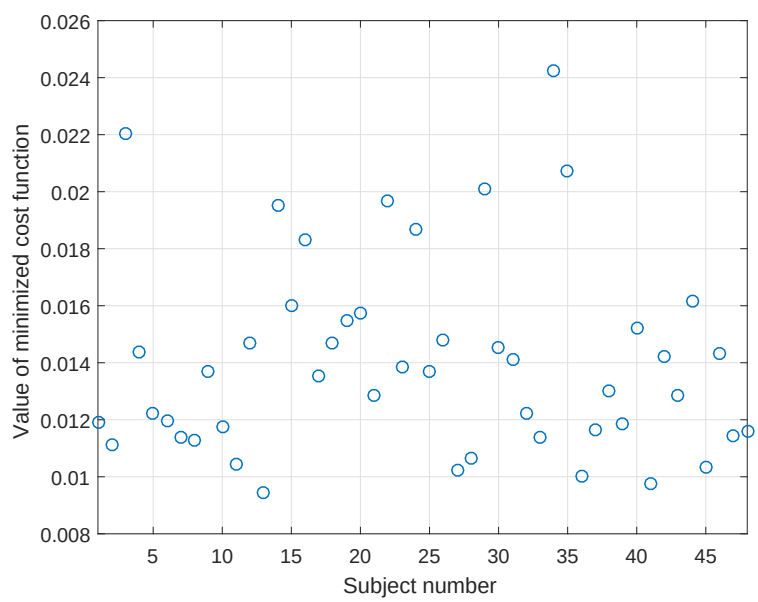


Figure 4.21: The value of minimized cost function

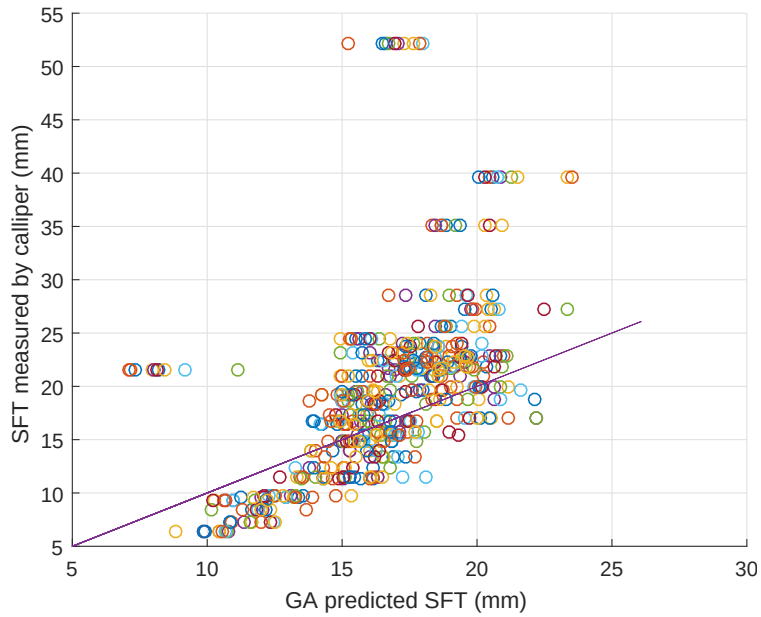


Figure 4.22: The GA predicted SFT of 10 times of optimization

fixed but a random variable. To check the stability of the GA optimization, the optimization problem (4.17) has been optimized by the GA with the same options for 10 times, and the GA predicted SFT is plotted in Fig. 4.22. The values of minimized cost functions of 10 times of optimization is plotted in Fig. 4.23.

Fig. 4.22 and Fig. 4.23 show the output of 10 times of optimization is very close, therefore the optimization problem (4.17) is not ill conditioned.

## 4.8 Impedance patching on the surface

The previous chapter shows a method of evaluating the surface layer thickness of human body by the multisphere model. But this method is not rigorous enough since it does not take the detailed shape of human body into account. In this chapter we will show a efficient method of calculating the scattering

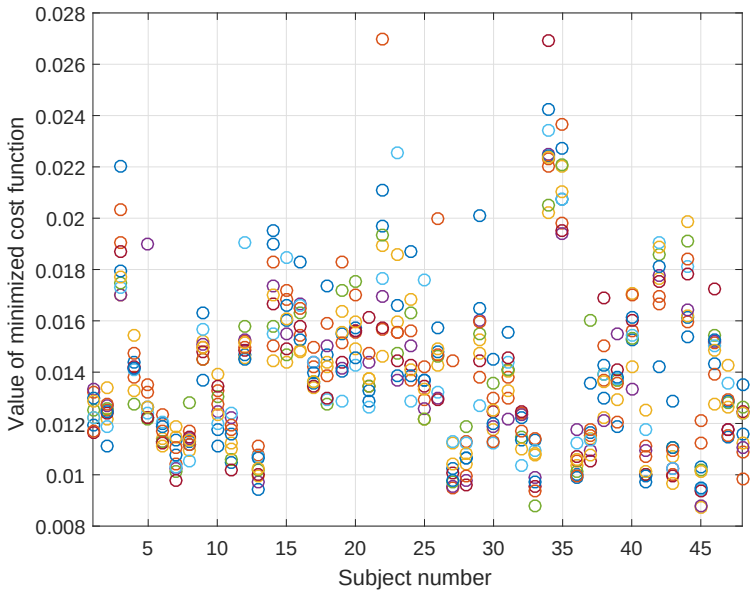


Figure 4.23: The value of cost functions of 10 times of optimization

properties of a multilayer object with arbitrary shape. The basic idea is to use an ABCD matrix to describe the coupling between the field in the inner most layer and the field in free space.

As presented in Fig. 4.8, the ACS of human body above 6 GHz is dominated by the surface area, while the ACS below 6 GHz does not show strong linear correlations to any of the morphological parameters. Therefore, higher order model is required in accurate modelling human body ACS from morphological parameters.

As the basic rule of electromagnetics, Maxwell equations are consisted by two curl equations and two divergence equations which give the relationship between four variables $\vec{E}$, $\vec{D}$, $\vec{H}$, $\vec{B}$.

The Maxwell equations can be solved analytically only if the problem can be fitted into the grid of the three basic types of orthogonal coordinate system (Cartesian, cylindrical, and spherical). But when the problem involves solving objects with complex shape such as human body, the analytical tech-

nique would lose its effect because the boundary condition is not separable by variables. To accurately calculate the ACS of human body, the numerical techniques are unavoidable.

Even though the FDTD has been widely used as a method of calculating the WBSAR, it is not a very efficient method of calculating the absorption cross section of human body in diffuse environments. The reason is the diffuse field is modelled as a expansion of plane wave incident from all different directions and the independent calculation of ACS at different directions can take a very long time [40].

The remainder part of this section will present a method of effective modelling the surface layer's effect on lossy object. The method is basically an application of ABCD matrix on the surface integral equation (SIE). There are three advantages of this method, firstly, comparing to the volume integral equation, this method is more efficient in memory usage. Secondly, the coupling between the inner most layer and external region is simplified by an ABCD matrix at a particular position on the surface, therefore the coupling between each layer do not need to be modelled independently [90]. Thirdly, the scattering field is mapped to the incident field by a impedance matrix, and the impedance matrix is only determined by the shape and material of the scattering object. so that scattered fields under different incident wave can be obtained by solving impedance matrix for only once, which is time efficient [91].

Our problem is about efficient modelling a homogeneous object covered by thin layers. Similar problem of scattering by thin layer media is studied by Richmond [92], Harrington [93], Chiang [94], who used the technique of solving volume integral equation (VIE). Such a technique has been used by Livesay [95] to solve the non-ionizing dosimetry problems. The idea of VIE is simple. After an incident wave is scattered by a object, the total field can

be expressed by the summation of scattering field and incident field:

$$\begin{cases} \vec{E} = \vec{E}_{\text{inc}} + \vec{E}_s \\ \vec{H} = \vec{H}_{\text{inc}} + \vec{H}_s \end{cases} \tag{4.20}$$

where $\vec{E}$, $\vec{H}$ are the total electric field and magnetic field out side the scattering object; $\vec{E}_{\text{inc}}$, $\vec{H}_{\text{inc}}$ are incident electric field and magnetic field; $\vec{E}_s$, $\vec{H}_s$ are the scattered electric field and magnetic field. Of course $\vec{E}$, $\vec{H}$ should satisfy the Maxwell's equations in source free region:

$$\begin{cases} \nabla \times \vec{H} = j\omega\epsilon\vec{E} \\ \nabla \times \vec{E} = -j\omega\mu\vec{H} \end{cases} \tag{4.21}$$

On the other hand, the incident wave $\vec{E}_{\text{inc}}$, $\vec{H}_{\text{inc}}$ satisfies the Maxwell's equations in free space:

$$\begin{cases} \nabla \times \vec{H}_{\text{inc}} = j\omega\epsilon_0\vec{E}_{\text{inc}} \\ \nabla \times \vec{E}_{\text{inc}} = -j\omega\mu_0\vec{H}_{\text{inc}} \end{cases} \tag{4.22}$$

Due to the linearity of Maxwell's equations, (4.21) - (4.22) gives:

$$\begin{cases} \nabla \times \left(\vec{H} - \vec{H}_{\text{inc}}\right) = j\omega\left(\epsilon\vec{E} - \epsilon_0\vec{E}_{\text{inc}}\right) \\ \nabla \times \left(\vec{E} - \vec{E}_{\text{inc}}\right) = -j\omega\left(\mu\vec{H} - \mu_0\vec{H}_{\text{inc}}\right) \end{cases} \tag{4.23}$$

Then substituting (4.20) into (4.23) gives:

$$\begin{cases} \nabla \times \vec{H}_s = j\omega(\epsilon - \epsilon_0)(\vec{E}_{\text{inc}} + \vec{E}_s) + j\omega\epsilon_0\vec{E}_s \\ \nabla \times \vec{E}_s = -j\omega(\mu - \mu_0)(\vec{H}_{\text{inc}} + \vec{H}_s) - j\omega\mu_0\vec{H}_s \end{cases} \tag{4.24}$$

If the scattering object is formed by non-ferrite material, $\mu$ would be equal

to $\mu_0$. So (4.24) changes into:

$$\begin{cases} \nabla \times \vec{H}_s = j\omega(\epsilon - \epsilon_0)(\vec{E}_{\text{inc}} + \vec{E}_s) + j\omega\epsilon_0\vec{E}_s \\ \nabla \times \vec{E}_s = -j\omega\mu_0\vec{H}_s \end{cases} \tag{4.25}$$

where $\vec{J}_p = j\omega(\epsilon - \epsilon_0)(\vec{E}_{\text{inc}} + \vec{E}_s)$ in the first equation is the polarized current. (4.25) shows the scattered field $E_s$ can be considered as the field generated by polarized currents in free space. The advantage of solving (4.25) by VIE is that the permittivity $\epsilon$ is only included in the $\vec{J}_p$, which means only the Green's function in free space is involved in the whole calculation. Solving (4.25) would be good in dealing with inhomogeneous scatterers.

But the shortcoming of solving (4.25) by VIE is obvious too. It needs the region occupied by $\vec{J}_p$ to be discretized. Therefore the number of unknown variables of solving VIE is increased with the volume of the scatterer, while the number of unknown variables in solving SIE is increased with the surface area of the scatterer.

Chiang's approach was to discrete only the surface layer of a scatterer into small patches. When the problem goes to multi-layer surface structure, each layer would be discretized separately [96], so the unknowns still increases with the increasing number of surface layers.

To reduce the number of unknown variables introduced by multilayer structure, a little bit more simplification can be made. Here we use ABCD matrix, also known as transfer matrix, to model the relationship between the internal field within the homogeneous core and the scattered field on the outer surface of the scattering object

The ABCD matrix is defined by:

$$\begin{bmatrix} E_{\text{ext}} \\ H_{\text{ext}} \end{bmatrix} = \begin{bmatrix} A & B \\ C & D \end{bmatrix} \begin{bmatrix} E_{\text{int}} \\ H_{\text{int}} \end{bmatrix} \tag{4.26}$$

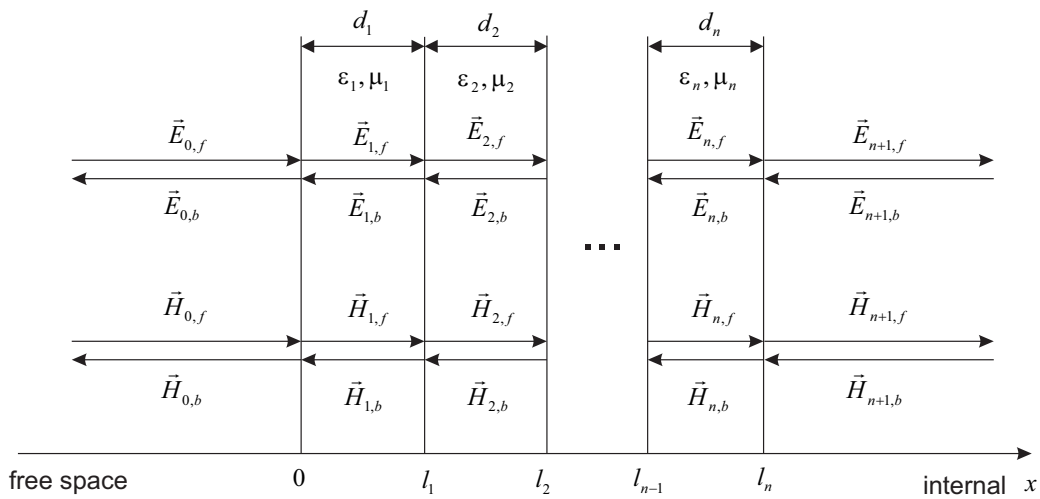


Figure 4.24: Field transmission through multilayer structure

where $E_{\text{ext}}$, $H_{\text{ext}}$ are the external E field and external H field; $E_{\text{int}}$, $H_{\text{int}}$ are the internal E field and internal H field.

Assuming the coupling between internal field and external field at a particular position of a scatterer's surface is dominated by the superficial layer structure, the ABCD matrix can be calculated from a multilayer planar model, as shown in Fig. 4.24, where all layers are numbered consecutively from the outermost layer to innermost layer. layer 0 is free space. layer n+1 is the homogeneous core of scatterer. layer 1 to layer n are the surface layers around the scatterer. $d_i$ denotes the thickness of $i$th layer. $l_i$ is the coordinate of interface between $i$th layer and $i+1$th layer. $l_i$ equals to $\sum_{k=1}^{i} d_k$. $\vec{E}_{i,f}$ denotes the electric field transmitting forwardly along the positive direction of x axis in $i$th layer. Similarly $\vec{E}_{i,b}$ is the E field transmitting backward in $i$th layer. $\vec{H}_{i,f}$ and $\vec{H}_{i,b}$ are the corresponding H field transmitting forward and backward in $i$th layer.

Assuming $\vec{E}_{i,f}$ and $\vec{E}_{i,b}$ are both pointing to $\hat{y}$ direction, the coupling

between the $\vec{E}$ field and the $\vec{H}$ field in each layer can be written as:

$$\begin{cases} \vec{E}_{i,f} = E_{i,f}\exp(-jk_i x)\hat{y} \\ \vec{E}_{i,b} = E_{i,b}\exp(jk_i x)\hat{y} \\ \vec{H}_{i,f} = \frac{k_i}{\omega\mu 0}E_{i,f}\exp(-jk_i x)\hat{z} \\ \vec{H}_{i,b} = -\frac{k_i}{\omega\mu 0}E_{i,b}\exp(jk_i x)\hat{z} \end{cases} \tag{4.27}$$

Where $E_{i,f}$ and $E_{i,b}$ are the only two independent variables determining the field distribution in $i$th layer.

Since the E field and H field should be continuous on every interface, on the interface $l_i$ there is relation:

$$\begin{cases} E_{i,f}\exp(-jk_i d_i) + E_{i,b}\exp(jk_i d_i) = E_{i+1,f} + E_{i+1,b} \\ \frac{k_i}{\omega\mu 0}E_{i,f}\exp(-jk_i d_i) - \frac{k_i}{\omega\mu 0}E_{i,b}\exp(jk_i d_i) = \frac{k_{i+1}}{\omega\mu 0}E_{i+1,f} - \frac{k_{i+1}}{\omega\mu 0}E_{i+1,b} \end{cases} \tag{4.28}$$

The permittivity of $\mu_0$ can be cancelled on both sides of the equations, which gives:

$$\begin{cases} E_{i,f}\exp(-jk_i d_i) + E_{i,b}\exp(jk_i d_i) = E_{i+1,f} + E_{i+1,b} \\ \sqrt{\epsilon_i}E_{i,f}\exp(-jk_i d_i) - \sqrt{\epsilon_i}E_{i,b}\exp(jk_i d_i) = \sqrt{\epsilon_{i+1}}E_{i+1,f} - \sqrt{\epsilon_{i+1}}E_{i+1,b} \end{cases} \tag{4.29}$$

(4.29) can not be applied on $l_0$ because there is no $d_0$ defined in the problem. On interface $l_0$ there is:

$$\begin{cases} E_{0,f} + E_{0,b} = E_{1,f} + E_{1,b} \\ \sqrt{\epsilon_0}E_{0,f} - \sqrt{\epsilon_0}E_{0,b} = \sqrt{\epsilon_1}E_{1,f} - \sqrt{\epsilon_1}E_{1,b} \end{cases} \tag{4.30}$$

The ABCD matrix can be obtained directly from solving the combination of (4.29) and (4.30). For instance, when there are only one surface layer,

(4.29) and (4.30) becomes:

$$\begin{bmatrix} 1 & 1 & -1 & -1 & 0 & 0 \\ \sqrt{\epsilon_0} & -\sqrt{\epsilon_0} & -\sqrt{\epsilon_1} & \sqrt{\epsilon_1} & 0 & 0 \\ 0 & 0 & e^{-jkd_1} & e^{jkd_1} & -1 & -1 \\ 0 & 0 & \sqrt{\epsilon_1}e^{-jkd_1} & -\sqrt{\epsilon_1}e^{jkd_1} & -\sqrt{\epsilon_2} & \sqrt{\epsilon_2} \end{bmatrix} \begin{bmatrix} E_{0,f} \\ E_{0,b} \\ E_{1,f} \\ E_{1,b} \\ E_{2,f} \\ E_{2,b} \end{bmatrix} = \begin{bmatrix} 0 \\ 0 \\ 0 \\ 0 \\ 0 \\ 0 \end{bmatrix} \tag{4.31}$$

Moving the term $E_{2,f}$ and $E_{2,b}$ to the right side of the equation gives:

$$\begin{bmatrix} 1 & 1 & -1 & -1 \\ \sqrt{\epsilon_0} & -\sqrt{\epsilon_0} & -\sqrt{\epsilon_1} & \sqrt{\epsilon_1} \\ 0 & 0 & e^{-jkd_1} & e^{jkd_1} \\ 0 & 0 & \sqrt{\epsilon_1}e^{-jkd_1} & -\sqrt{\epsilon_1}e^{jkd_1} \end{bmatrix} \begin{bmatrix} E_{0,f} \\ E_{0,b} \\ E_{1,f} \\ E_{1,b} \end{bmatrix} = \begin{bmatrix} 0 & 0 & 0 & 0 \\ 0 & 0 & 0 & 0 \\ 0 & 0 & -1 & -1 \\ 0 & 0 & \sqrt{\epsilon_2} & -\sqrt{\epsilon_2} \end{bmatrix} \begin{bmatrix} 0 \\ 0 \\ E_{2,f} \\ E_{2,b} \end{bmatrix} \tag{4.32}$$

Then, calculating the inverse of the matrix on the left side of (4.32) and multiplying the inverse matrix to the right side of the same equation can give the relation between $(E_{0,f}, E_{0,b})$ and $(E_{2,f}, E_{2,b})$, and the ABCD matrix can be obtained right after this relation is known. The similar method can be used to obtain the ABCD matrix when the number of surface layers is more than two.

Here an example is given to demonstrate how to apply ABCD matrix to calculate the scattering problem. For simplicity, the problem is to solve the TM wave scattered by a coated water cylinder in 2D. The basic setup is shown in Fig. 4.25.

A plane wave is propagating along the x axis from the negtive direction to the positive direction, and scattered by a cylinder whos axis is z-axis. The outer radius of the cylinder is 0.132 m. This value is selected just because it gives the circumference 0.83 m which is the same as the average waist size of all subjects in the experiment. The thickness of the shell would be set to

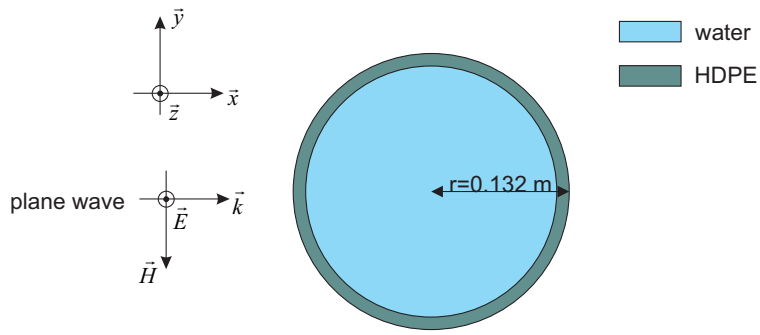


Figure 4.25: The coated water cylinder scattered by a TM wave

different values to test the algorithm. The shell is made up by HDPE.

According to Huygens' equivalence principle, the overall scattering problem can be broken down into two sub-problems. One sub-problem is calculating the field in the core (inside boundary $\Omega_1$) of the cylinder; The other sub-problem is calculating the scattered field in free space (out of boundary $\Omega_2$). The relation between the tangential fields on $\Omega_1$ and $\Omega_2$ can be described by the ABCD matrix. Since we are only dealing with the TM wave, applying both $\vec{J}$ and $\vec{M}$ to the boundary would make the problem more complicated because $\vec{M}$ is located in x-y plane. solving $\vec{M}$ would introduce extra dimensions into the equation system. Here only $\vec{J}$ was applied as the equivalent source and the equivalent problems is demonstrated in Fig. 4.26 where $\Omega_0$ denotes the outer boundary of the cylinder, $\Omega_1$ denotes the inner boundary of the cylinder; $\vec{E}_{\text{inc}}$ and $\vec{H}_{\text{inc}}$ are the E-field and H-field of the incident wave; $\vec{E}_{\text{s0}}$ and $\vec{H}_{\text{s0}}$ are the scattered E-field and H-field out of boundary $\Omega_0$; $\vec{E}_{\text{s1}}$ and $\vec{H}_{\text{s1}}$ are the scattered field within boundary $\Omega_1$; For the problem out of boundary $\Omega_0$, the background material is free space, and the field is generated by the equivalent current $\vec{J}_0$; For the problem in $\Omega_1$, the background material is identical to the core material of the original problem, and the field in $\Omega_1$ is generated by $\vec{J}_1$.

The next step is to combine these two equivalent problems together and

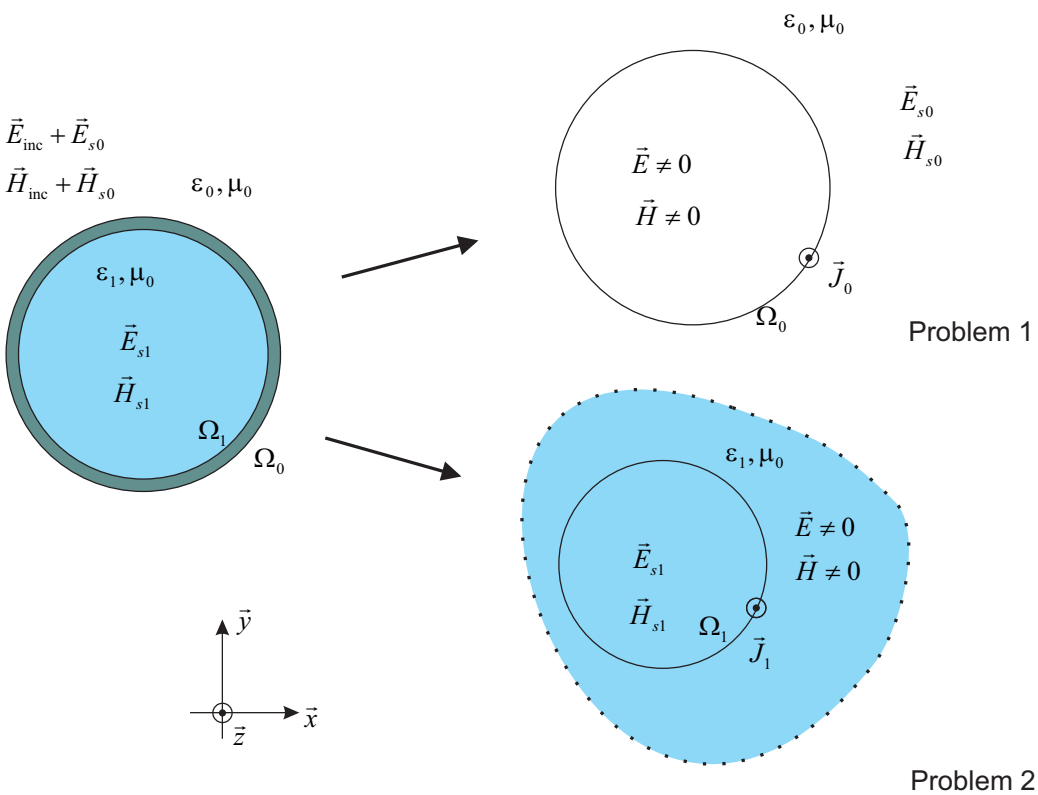


Figure 4.26: Equivalent problems of a plane wave scattered by a coated water cylinder

give an equation system. Since $\Omega_0$ and $\Omega_1$ are two different surfaces and the field across the boundaries in two equivalent problems is unknown, the relations between $\vec{J_0}$ and $\vec{J_1}$ is not known as well.

Applying the Green's function, the $\vec{E}$ field and $\vec{H}$ field at arbitrary point $\vec{r}$ generated by current $\vec{J_e}$ can be written as:

$$E(\vec{r}, \epsilon, \mu, \vec{J_e}) = \oiint_S \left[ j\omega\mu \vec{J_e}(\vec{r'}) G(\vec{r}, \vec{r'}) \right] \mathrm{d}S \tag{4.33}$$

$$H(\vec{r}, \epsilon, \mu, \vec{J_e}) = \oiint_S \left[ \vec{J_e}(\vec{r'}) \times \nabla' G(\vec{r}, \vec{r'}) \right] \mathrm{d}S \tag{4.34}$$

To be more specifically, the EM field generated by $\vec{J_1}$ and $\vec{J_0}$ is:

$$E_{s0}(\vec{r}, \epsilon_0, \mu, \vec{J_e}) = \oiint_S \left[ j\omega\mu \vec{J_0}(\vec{r'}) G_0(\vec{r}, \vec{r'}) \right] \mathrm{d}S \tag{4.35}$$

$$H_{s0}(\vec{r}, \epsilon_0, \mu, \vec{J_e}) = \oiint_S \left[ \vec{J_0}(\vec{r'}) \times \nabla' G_0(\vec{r}, \vec{r'}) \right] \mathrm{d}S \tag{4.36}$$

$$E_{s1}(\vec{r}, \epsilon, \mu, \vec{J_e}) = \oiint_S \left[ j\omega\mu \vec{J_1}(\vec{r'}) G_1(\vec{r}, \vec{r'}) \right] \mathrm{d}S \tag{4.37}$$

$$H_{s1}(\vec{r}, \epsilon, \mu, \vec{J_e}) = \oiint_S \left[ \vec{J_1}(\vec{r'}) \times \nabla' G_1(\vec{r}, \vec{r'}) \right] \mathrm{d}S \tag{4.38}$$

Where $G_0$ and $G_1$ are the Green's function in free space and water, respectively .

Now consider a pair of points on each side of the surface layer, as shown in Fig. 4.27 where $\vec{r_0}$ and $\vec{r_1}$ are the position vector of the two points $P_0$ and $P_1$, respectively. $P_0$ is skewed by the surface normal vector at $P_1$. If the thickness of surface layer is much smaller than the radius of surface curvature, for every $P_1$ on surface $\Omega_1$ there should be a $P_0$ on the surface $\Omega_0$.

The tangential EM field at $P_0$ and $P_1$ should have a relation defined by

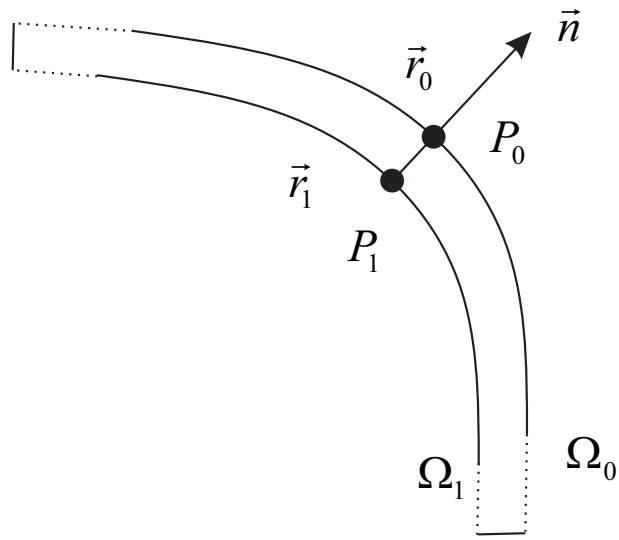


Figure 4.27: The point pairs on the surface

ABCD matrix. Substituting (4.37) and (4.38) into (4.26) gives:

$$\begin{bmatrix} E_{t,e}(\vec{r}_0, \epsilon 0, \mu 0, \vec{J}_0) \\ H_{t,e}(\vec{r}_0, \epsilon 0, \mu 0, \vec{J}_0) \end{bmatrix} = \begin{bmatrix} A & B \\ C & D \end{bmatrix} \begin{bmatrix} E_{\text{inc,t}} + E_{t,i}(\vec{r}_0, \epsilon, \mu 0, \vec{J}_1) \\ H_{\text{inc,t}} + H_{t,i}(\vec{r}_0, \epsilon, \mu 0, \vec{J}_1) \end{bmatrix} \tag{4.39}$$

where the subscript $t, e$ means the tangential external field, and $t, i$ means the tangential internal field, correspondingly. Solving (4.39) would give the solution of $J_0$ and $J_1$.

To validate the numerical method, the shell thickness was set to be 1 mm and 5 mm with outer radius fixed at 0.132 m, then the E-field on the outer surface $\Omega_0$ was calculated in each case at 6 GHz. The cylinder surface is divided into 400 segments in 2D. The memory consumption is 10.24 MByte. CPU runtime is 32 seconds. The result was then compared to the analytical solution which is demonstrated in Fig. 4.28.

The figure shows two facts. First, the impedance patching techniques can successfully calculate the E field. Its result matches good with that given by

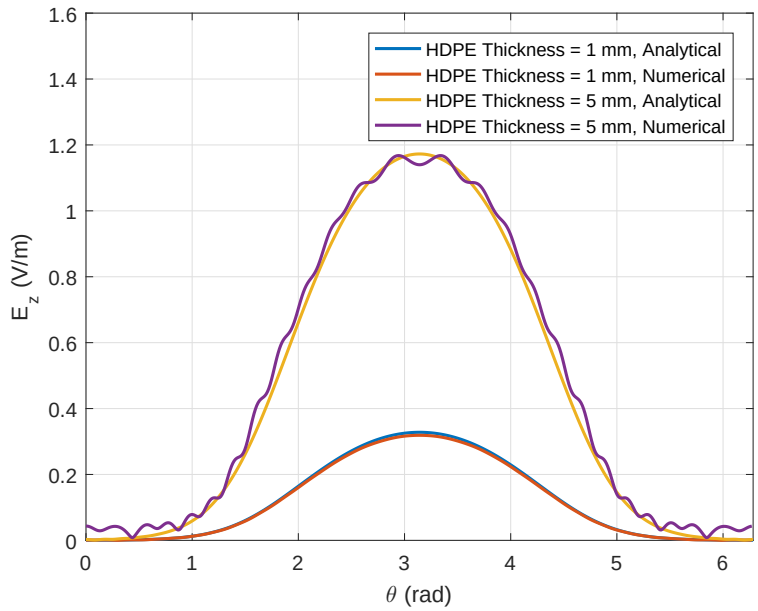


Figure 4.28: The E-field on the outer surface of cylinder at 6 GHz

the analytical method. The maximum difference between numerical results and analytical results is 0.071 V/m. Secondly, the accuracy of numerical method goes down as the shell thickness increases. Thirdly, changing on the surface layer thickness can be critical to the overall absorption cross section of the scattering object, the increases of 4 mm shell thickness almost quadrupled the maximum field on the surface.

To demonstrate the problem further, the water cylinder in Fig. 4.25 is replaced by a muscle cylinder covered by a fat layer and a skin layer. Same as the water cylinder, the surface of the cylinder is also divided into 400 segments, so the memory consumption is the same as the previous water cylinder problem. The outer radius of the covered muscle cylinder is also 0.132 m. The skin layer thickness is 2 mm. The E-field at 6 GHz on the surface of the skin layer of the muscle cylinder with different fat layer thickness is given in Fig. 4.29. The CPU runtime is 35 seconds. The figure shows the analytical results matches well with the numerical results. In the case of fat

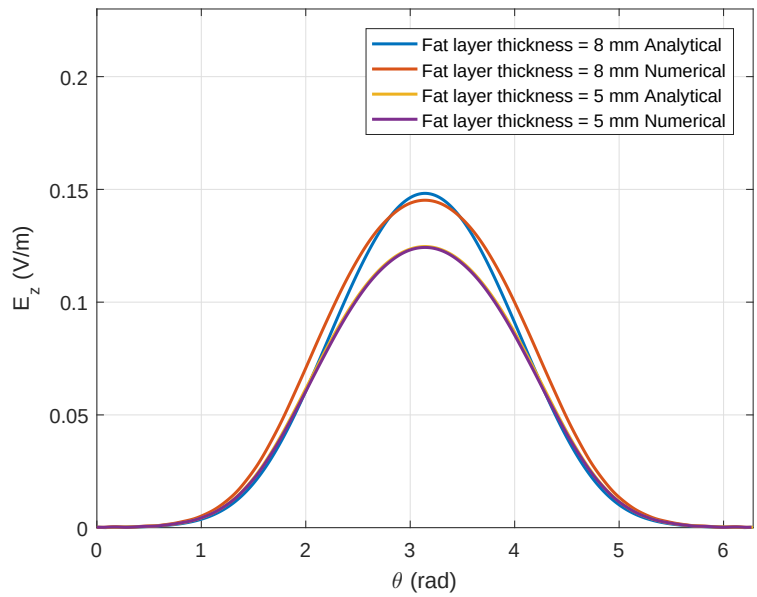


Figure 4.29: E field on the outer surface of the muscle cylinder at 6 GHz

layer thickness is 5 mm, the numerical results and analytical results almost overlap.

The power absorbed by a unit length of the muscle cylinder is calculated by integrating the Poynting vector on its surface. We choose 1 GHz to 6 GHz as the frequency range since this is a band where the fat layer thickness makes a lot of difference to the ACS, while over 6 GHz most of the EM power would be absorbed by the skin, as being analysed in Fig. 2.2. The results calculated by numerical impedance patching was compared to the analytical solution in Fig. 4.30. Fig. 4.30 proves the effectiveness of surface impedance patching in calculating the power loss. The effect of 3 mm fat layer change on the power absorption can be evaluated accurately by the numerical method.

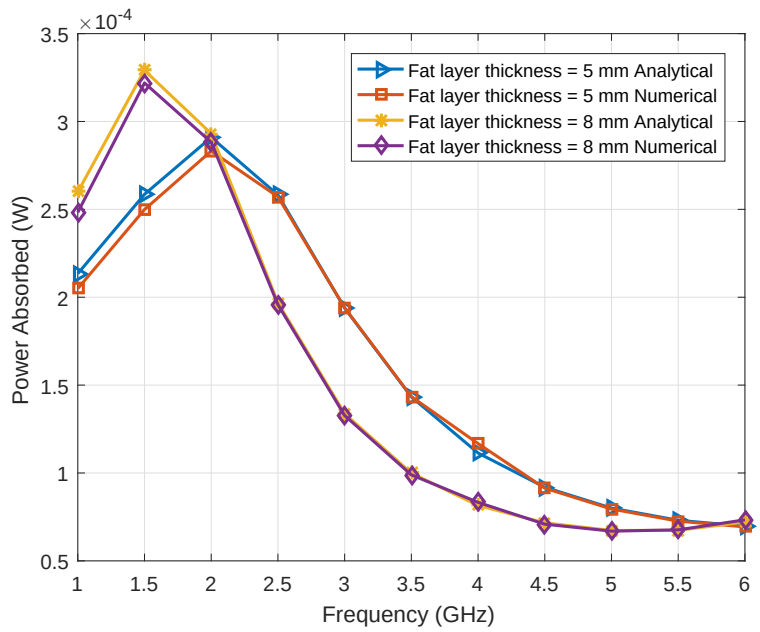


Figure 4.30: The EM power absorbed by a unit length of the muscle cylinder

## 4.9 Summary

In this chapter we firstly performed a study on the posture's effect on the averaged human body ACS. The study shows the more extended posture tend to give higher averaged ACS. Then the group measurements were conducted on 48 subjects and the relation between the averaged human body ACS and morphological parameters were studied. The measurement results show the averaged human body ACS is highly correlated with the BSA over 6 GHz. Therefore a linear empirical formula was inducted for quickly evaluating the human body ACS from BSA with $R^2 > 0.8$ over 6 GHz.

Below 6 GHz, the correlations between the human body ACS and all morphological parameters become weaker. Therefore the linear empirical formula is not suitable for predicting the ACS by morphological parameters below 6 GHz. Instead, we modelled the ACS below 6 GHz by choosing several

markers on the curve of human body absorption coefficient and use their coordinates as simple predictors. The simple predictors were correlated to the morphological parameters by linear formula. We found the local minimum of the human body absorption coefficient around 5 GHz will shift to lower frequencies as averaged fat layer thickness increases, which is very similar to the feature of the absorption coefficient of the multi-layer spherical model. The high absorption coefficient of human body at 1 GHz is also very similar to the absorption property of multi-layer spherical model.

Enlightened by the similarity between the human body absorption coefficient and that of a multi-layer sphere, we expanded the human body absorption coefficient into a summation of the absorption coefficients of several multi-layer spheres with different surface layer thickness. The contribution of each multi-layer sphere into the whole absorption coefficient is weighted by a factor whose value is determined by the GA. The weighted average of the surface layer thickness (skin layer thickness + fat layer thickness) of all sphere models with the weight factor given by the GA gives results very close to the skin fold measurement.

In the last section of this chapter, we presented a surface impedance patching algorithm of calculating the EM power losses in an object. This method can calculate the power absorption of objects with arbitrary surface structure. The coupling between the internal field and the external field of an object is modelled by an ABCD matrix. Then the Huygens's principle was applied to assign the ABCD matrix to a small patch on the surface of the object. The coupling among all patches were given by the surface integral equations. The integral equations were solved to give the EM field on the surface.

The algorithm is validated by calculating the power absorption of a infinite long multilayer cylinder incident by a TM plane wave. The numerical results matches very well with the analytical solution.

The merit of the surface impedance patching method is that it models the multilayer surface structure by only one ABCD matrix, thus the number of integral equations would not increase as the number of surface layer increases. The impedance patching method provides a reliable way of modelling EM power absorption from 1 GHz to 6 GHz.

# Chapter 5

# Conclusion

In order to measure the ACS more efficiently in the RC, a new nonlinear curve fitting technique in extracting chamber time constant were developed. The new technique can cancel the effect of piecewise window function in the IFFT, therefore it allows narrow window functions to be applied in the IFFT. Comparing to the old linear fitting technique, the nonlinear curve fitting can extract the ACS from fewer samples of $S_{21}$, and do not harm the accuracy at the same time. The measurement of small absorbing cubes in the RC shows the nonlinear curve fitting typically requires 50% fewer $S_{21}$ samples to extract the ACS than the ordinary linear curve fitting does, but the accuracy does not decrease.

The accurate ACS measurements were performed on 48 subjects from 1 GHz to 18 GHz. The morphological data of all subject were recorded. The skin fold thickness was included in the measurement of morphological parameters. The subjects under test were supported by a stack of polystyrene sheets with limbs extended for better exposure. Strong positive linear correlations between the BSA and ACS were observed over 6 GHz. Another very strong negative linear correlation between the measured ACS and SFT was shown at 2.5 GHz. Techniques of mapping the human body absorption

coefficient to SFT was demonstrated by expanding the absorption coefficient of human into the summation of absorption coefficients of the multilayer spherical model. The local minimum of human body absorption coefficient at GHz region shifts to lower frequencies as the fat layer thickness increases, which is assumed to be the result of matching effect of fat layer.

In order to accurately model the effect of the surface layer on the power absorption of an object with arbitrary shape, the surface impedance patching algorithm was brought out. The method was validated in 2D TM cases by calculating the power absorption of lossy cylinders with different surface layer thickness. The result given by the impedance patching method matches very well with the analytical solution from 1 GHz to 6 GHz.

In general, all the three aims mentioned in Chapter 1 were achieved. First, the human body ACS is extracted accurately from the $S_{21}$ measured in the RC. The measurement of a reference sphere model shows our method has 3.98% less MAPE than the method applied in the previous research. Second, an empirical model of human body ACS was given by linear correlating the coordinates of the saddle points on the absorption coefficient curves to morphological parameters. At last, the EM power dissipation on the human body surface is modelled by solving Maxwell equations numerically with surface impedance patching algorithm.

## 5.1 Future works

Here are some suggestions on the future works.

1. In order to accurately determine the relations between the BFP and the averaged ACS of human body, the MRI or the dual-energy X-ray absorptiometry (DEXA) can be applied to determine the BFP more accurately than the skin fold method. The MRI is a non-invasive imaging technique which produce section images of human body by magnetic fields and radio

waves; The DEXA produces the inner body image by X-rays of different energy levels, which are usually used for body composition determination.

2. We conducted the group study on the correlation between BFP and human body ACS, which suggests the fat layer acts as a matching layer in the power absorption. This conclusion may be validated more comprehensively by tracking on a single subject's BFP and ACS. The subjects may be asked to manage their diet and exercise, thus their BFP and ACS would change with time. The single subject study would help in excluding the unknown factors that might change the ACS.

3. Our research only validated the impedance patching method in the 2D cases, we suggest the future work should include 3D application of this algorithm. This algorithm would be helpful in general applications such as the calculation of fields scattered by objects covered by thin surface layers.

# Chapter 6

# Appendices

## 6.1 Huygen's equivalent principle

The Huygens' equivalence principle says the actual sources (antenna, transmitter) can be replaced by equivalent surface sources about a region, and the equivalent sources will be generating the same field in that region as the actual sources do [97]. The basic idea is shown in Fig. 6.1 where $\hat{n}$ is the unit normal vector on a enclosed surface; $\vec{J}$ and $\vec{M}$ are the actual electric current source and magnetic current source being enclosed; $\vec{E}$ and $\vec{H}$ are the external field generated by the actual sources; $\vec{J}_e$ and $\vec{M}_e$ are the equivalent

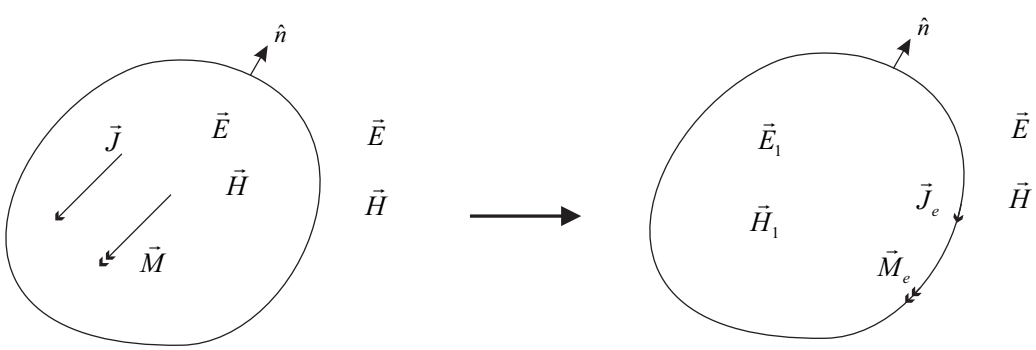


Figure 6.1: The Huygens equivalent principle

current sources which generate the same external field $E$ and $H$ as the actual source do; $\vec{E}_1$ and $\vec{H}_1$ are the internal field generated by $\vec{J}_e$ and $\vec{M}_e$. Beware that the internal field $\vec{E}_1$ and $\vec{H}_1$ of the equivalent problem may be different from the $\vec{E}$ and $\vec{H}$ of the original problem inside the boundary. The $\vec{J}_e$ and $\vec{M}_e$ can be calculated from $\vec{E}$, $\vec{H}$, $\vec{E}_1$, $\vec{H}_1$ by

$$\begin{cases} \vec{J}_e = \hat{n} \times \left(\vec{H} - \vec{H}_1\right) \\ \vec{M}_e = -\hat{n} \times \left(\vec{E} - \vec{E}_1\right) \end{cases} \tag{6.1}$$

In fact, the inner field $\vec{E}_1$ and $\vec{H}_1$ can be any field distributions as long as both of them satisfy the Maxwell's equations in source free region. Obviously $\vec{E}_1$ and $\vec{H}_1$ can be chosen as zero. Then (6.1) transform into:

$$\begin{cases} \vec{J}_e = \hat{n} \times \vec{H} \\ \vec{M}_e = -\hat{n} \times \vec{E} \end{cases} \tag{6.2}$$

It is also worth to point out (6.1) stands only when the whole region (inside and outside the boundary) is homogeneous. In the non-homogeneous cases, such as a scattering object is presented, the equivalent currents should be given in a different way. One common approach is to break down the scattering problem into two problems: one external, one internal [98]. The idea is presented in Fig. 6.2.

The background media for the two problems are different. In problem 1 (the external problem), the background media is free space, and the external field generated by equivalent sources is the same as the external field of the original scattering problem. Using (6.1), The equivalent sources are calculated by:

$$\begin{cases} \vec{J}_0 = \hat{n} \times \vec{H}_{s0} \\ \vec{M}_0 = -\hat{n} \times \vec{E}_{s0} \end{cases} \tag{6.3}$$

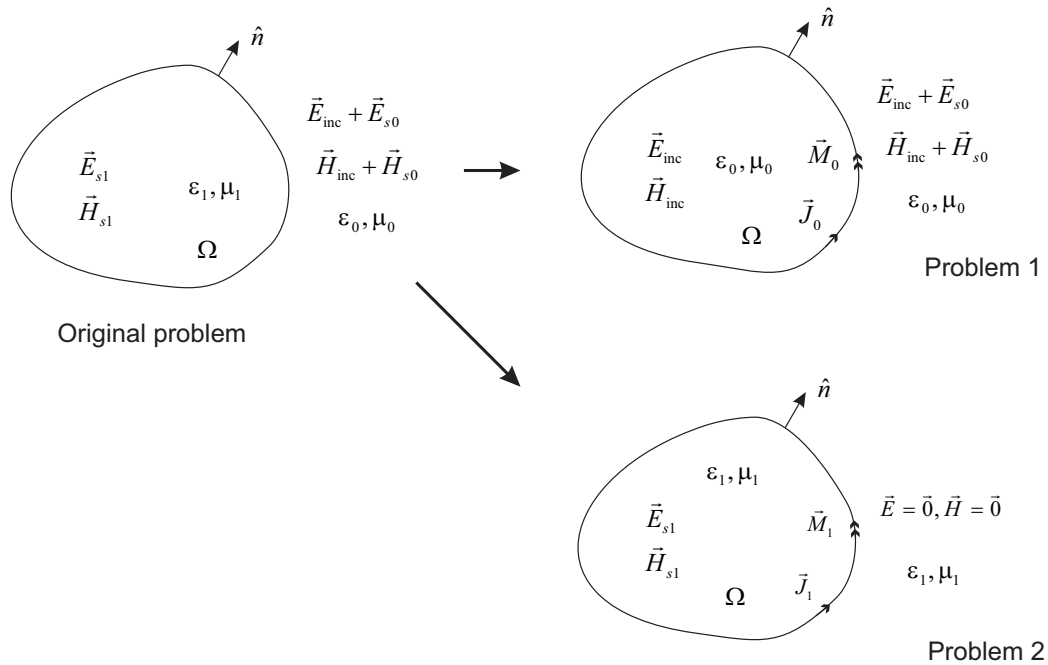


Figure 6.2: The equivalent problems of scattering problem

In problem 2 (the internal problem), the background media is the same as the media of the scattering object in the original scattering problem. In this case, the external field is set to be zero and the internal field is same as that of the original problem. The equivalent source is calculated by

$$\begin{cases} \vec{J}_1 = -\hat{n} \times \vec{H}_{s1} \\ \vec{M}_1 = \hat{n} \times \vec{E}_{s1} \end{cases} \tag{6.4}$$

Since the tangential EM field on $\Omega$ should be continuous in the original problem, there is:

$$\begin{cases} \hat{n} \times \vec{H}_{s1} = \hat{n} \times \left( \vec{H}_{\text{inc}} + \vec{H}_{s0} \right) \\ \hat{n} \times \vec{E}_{s1} = \hat{n} \times \left( \vec{E}_{\text{inc}} + \vec{E}_{s0} \right) \end{cases} \tag{6.5}$$

Substituting (6.3) and (6.4) into (6.5) gives:

$$\begin{cases} -\vec{J_1} = \hat{n} \times \vec{H}_{\text{inc}} + \vec{J_0} \\ \vec{M_1} = \hat{n} \times \vec{E}_{\text{inc}} - \vec{M_0} \end{cases} \tag{6.6}$$

Equation (6.6) gives the relation between the equivalent sources of two sub problems. But these are only two linear equations from which is not possible to solve four unknown variables. Therefore we need two other independent equations to give a unique solution of $\vec{J_0}$, $\vec{M_0}$, $\vec{J_1}$, $\vec{M_1}$.

The Green's function has to be introduced to give the rest of the two equations. The Green's function is the solution of an inhomogeneous linear differential equation [91]:

$$LG(\vec{r}, \vec{r'}) = \delta(\vec{r} - \vec{r'}) \tag{6.7}$$

where $\delta(\vec{r} - \vec{r'})$ is the Dirac delta function; $\vec{r'}$ is the position vector indicating the position of the impulse source; $G$ is Greens function; $L$ is the linear differentiate operator acting on $\vec{r}$. Simply speaking, Green's function gives a field distribution excited by a impulse source. Since an arbitrary source can be represented by a linear combination of many independent impulse sub-sources, the total field excited by this arbitrary source can be calculated by the summation of all the fields excited by the impulse sub-sources.

Given equivalent sources $\vec{J_e}$, and $\vec{M_e}$, the field generated by the equivalent sources in the media $(\mu, \epsilon)$ can be written as [99]:

$$E(\vec{r}, \epsilon, \mu, \vec{J_e}, \vec{M_e}) =$$
$$\oiint_S \left[ j\omega\mu \vec{J_e}(\vec{r'}) G(\vec{r}, \vec{r'}) - \frac{\rho_J(\vec{r'})}{\epsilon} \nabla' G(\vec{r}, \vec{r'}) + \vec{M_e}(\vec{r'}) \times \nabla' G(\vec{r}, \vec{r'}) \right] \mathrm{d}S \tag{6.8}$$

$$H(\vec{r}, \epsilon, \mu, \vec{J}_e, \vec{M}_e) =$$
$$\oiint_S \left[ j\omega\epsilon\vec{M}_e(\vec{r'})G(\vec{r}, \vec{r'}) - \frac{\rho_M(\vec{r'})}{\mu}\nabla' G(\vec{r}, \vec{r'}) + \vec{J}_e(\vec{r'}) \times \nabla' G(\vec{r}, \vec{r'}) \right] \mathrm{d}S \quad (6.9)$$

where $\rho_J$ is free electric charges; $\rho_M$ is fictional magnetic charges. They can be calculated by:

$$\begin{cases} \rho_J = -\frac{\nabla \cdot \vec{J}}{j\omega} \\ \rho_M = -\frac{\nabla \cdot \vec{M}}{j\omega} \end{cases} \quad (6.10)$$

In the original problem demonstrated in Fig. 6.2, the tangential component of EM field is continuous over the boundary, the full form of SIE can be written as:

$$\begin{cases} \hat{n} \times \left[ \vec{E}_{s0}(\vec{r'}, \epsilon_0, \mu_0, \vec{J}_0, \vec{M}_0) + \vec{E}_{\text{inc}} \right] = \hat{n} \times \vec{E}_{s1}(\vec{r'}, \epsilon_1, \mu_1, \vec{J}_1, \vec{M}_1) \\ \hat{n} \times \left[ \vec{H}_{s0}(\vec{r'}, \epsilon_0, \mu_0, \vec{J}_0, \vec{M}_0) + \vec{H}_{\text{inc}} \right] = \hat{n} \times \vec{H}_{s1}(\vec{r'}, \epsilon_1, \mu_1, \vec{J}_1, \vec{M}_1) \end{cases} \quad (6.11)$$

where $E_{s0}$, $H_{s0}$, $E_{s1}$, $H_{s1}$ are calculated by (6.8) and (6.9). $\vec{J}_0$, $\vec{M}_0$, $\vec{J}_1$, $\vec{M}_1$ satisfy (6.6).

The SIE (6.11) can be solved by method of moments [91]. So far the problem is restricted to homogeneous scatterers. When the scatterer is inhomogeneous, equivalent sources should be applied on every enclosed interfaces within the scatterer, therefore the number of unknowns would quickly increase, which makes solving the SIE becoming very inefficient.

# List of Abbreviations

| | |
|---|---|
| 2D | 2 dimensional |
| 3D | 3 dimensional |
| ACS | absorption cross section |
| BD | body density |
| BFP | body fat percentage |
| BMI | body mass index |
| BSA | body surface area |
| CIR | channel impulse response |
| DEXA | Dual energy X-ray absorptiometry |
| EM | electromagnetic |
| FD | frequency domain |
| FDTD | finite difference time domain |
| GA | genetic algorithm |
| HDPE | high density polystyrene |
| IFFT | inverse Fourier transform |
| MAPE | mean absolute percentage error |
| MoM | method of moments |
| MRI | magnetic resonance imaging |
| PDP | power delay profile |
| RC | reverberation chamber |
| RMS | root mean square |

| | |
|---|---|
| SAR | specific absorption rate |
| SFT | skin fold thickness |
| SIE | surface integral equation |
| TD | time domain |
| VNA | vector network analyser |
| VIE | volume integral equation |
| WBSAR | whole-body specific absorption rate |

# Bibliography


[1] B. Turner, "Cooking protestors alive: The excessive-force implications of the active denial system," *Duke Law & Tech Review*, vol. 11, p. 332, 2012.

[2] P. Bernardi, M. Cavagnaro, S. Pisa, and E. Piuzzi, "Specific absorption rate and temperature elevation in a subject exposed in the far-field of radio-frequency sources operating in the 10-900-MHz range," *IEEE Transactions on Biomedical Engineering*, vol. 50, pp. 295–304, March 2003.

[3] I. Flintoft, M. Robinson, G. Melia, A. Marvin, and J. Dawson, "Average absorption cross-section of the human body measured at 1–12 GHz in a reverberant chamber: results of a human volunteer study," *Physics in medicine and biology*, vol. 59, no. 13, p. 3297, 2014.

[4] P. Dimbylow, "FDTD calculations of the whole-body averaged SAR in an anatomically realistic voxel model of the human body from 1 MHz to 1 GHz," *Physics in medicine and biology*, vol. 42, no. 3, p. 479, 1997.

[5] P. Dimbylow, "Resonance behaviour of whole-body averaged specific energy absorption rate (SAR) in the female voxel model, NAOMI," *Physics in Medicine and Biology*, vol. 50, no. 17, p. 4053, 2005.

[6] O. P. Gandhi, "State of the knowledge for electromagnetic absorbed dose in man and animals," *Proceedings of the IEEE*, vol. 68, no. 1, pp. 24–32, 1980.

[7] M. Hagmann and O. Gandhi, "Numerical calculation of electromagnetic energy deposition in models of man with grounding and reflector effects," *Radio Science*, vol. 14, no. 6S, pp. 23–29, 1979.

[8] D. M. Sullivan, D. T. Borup, and O. P. Gandhi, "Use of the finite-difference time-domain method in calculating EM absorption in human tissues," *IEEE Transactions on Biomedical Engineering*, no. 2, pp. 148–157, 1987.

[9] P. Dimbylow, "The calculation of induced currents and absorbed power in a realistic, heterogeneous model of the lower leg for applied electric fields from 60 Hz to 30 MHz," *Physics in medicine and biology*, vol. 33, no. 12, p. 1453, 1988.

[10] ICRP, "Human respiratory tract model for radiological protection," *ICRP Publication 66*, 1994.

[11] T. Nagaoka, S. Watanabe, K. Sakurai, E. Kunieda, S. Watanabe, M. Taki, and Y. Yamanaka, "Development of realistic high-resolution whole-body voxel models of Japanese adult males and females of average height and weight, and application of models to radio-frequency electromagnetic-field dosimetry," *Physics in medicine and biology*, vol. 49, no. 1, p. 1, 2003.

[12] P. Dimbylow, "Development of the female voxel phantom, NAOMI, and its application to calculations of induced current densities and electric fields from applied low frequency magnetic and electric fields," *Physics in medicine and biology*, vol. 50, no. 6, p. 1047, 2005.

[13] P. J. Dimbylow, A. Hirata, and T. Nagaoka, "Intercomparison of whole-body averaged SAR in European and Japanese voxel phantoms," *Physics in medicine and biology*, vol. 53, no. 20, p. 5883, 2008.

[14] L. Sandrini, A. Vaccari, C. Malacarne, L. Cristoforetti, and R. Pontalti, "RF dosimetry: a comparison between power absorption of female and male numerical models from 0.1 to 4 GHz," *Physics in medicine and biology*, vol. 49, no. 22, p. 5185, 2004.

[15] D. Yu, M. Wang, and Q. Liu, "Development of Chinese reference man deformable surface phantom and its application to the influence of physique on electromagnetic dosimetry," *Physics in medicine and biology*, vol. 60, no. 17, p. 6833, 2015.

[16] E. Conil, A. Hadjem, F. Lacroux, M. Wong, and J. Wiart, "Variability analysis of SAR from 20 MHz to 2.4 GHz for different adult and child models using finite-difference time-domain," *Physics in medicine and biology*, vol. 53, no. 6, p. 1511, 2008.

[17] A. Hirata, S. Kodera, J. Wang, and O. Fujiwara, "Dominant factors influencing whole-body average SAR due to far-field exposure in whole-body resonance frequency and GHz regions," *Bioelectromagnetics*, vol. 28, no. 6, pp. 484–487, 2007.

[18] X. Xu, T. Chao, and A. Bozkurt, "VIP-Man: an image-based whole-body adult male model constructed from color photographs of the visible human project for multi-particle Monte Carlo calculations," *Health Physics*, vol. 78, no. 5, pp. 476–486, 2000.

[19] V. Spitzer, M. J. Ackerman, A. L. Scherzinger, and D. Whitlock, "The visible human male: a technical report," *Journal of the American Medical Informatics Association*, vol. 3, no. 2, pp. 118–130, 1996.

[20] T. Wu, L. Tan, Q. Shao, C. Zhang, C. Zhao, Y. Li, E. Conil, A. Hadjem, J. Wiart, B. Lu, *et al.*, "Chinese adult anatomical models and the application in evaluation of RF exposures," *Physics in medicine and biology*, vol. 56, no. 7, p. 2075, 2011.

[21] C. H. Kim, S. H. Choi, J. H. Jeong, C. Lee, and M. S. Chung, "HDRK-Man: a whole-body voxel model based on high-resolution color slice images of a Korean adult male cadaver," *Physics in medicine and biology*, vol. 53, no. 15, p. 4093, 2008.

[22] P. Dimbylow, "Fine resolution calculations of sar in the human body for frequencies up to 3 GHz," *Physics in medicine and biology*, vol. 47, no. 16, p. 2835, 2002.

[23] I. G. Zubal, C. R. Harrell, E. O. Smith, A. L. Smith, and P. Krischlunas, "Two dedicated software, voxel-based, anthropomorphic (torso and head) phantoms," in *Proceedings of the International Workshop, National Radiological Protection Board, Chilton, UK*, vol. 6, 1995.

[24] A. Christ, W. Kainz, E. G. Hahn, K. Honegger, M. Zefferer, E. Neufeld, W. Rascher, R. Janka, W. Bautz, J. Chen, *et al.*, "The Virtual Family-development of surface-based anatomical models of two adults and two children for dosimetric simulations," *Physics in medicine and biology*, vol. 55, no. 2, p. N23, 2009.

[25] J. S. Park, M. S. Chung, S. B. Hwang, B.-S. Shin, and H. S. Park, "Visible Korean human: its techniques and applications," *Clinical Anatomy*, vol. 19, no. 3, pp. 216–224, 2006.

[26] A. K. Jonscher, "Dielectric relaxation in solids," *Journal of Physics D: Applied Physics*, vol. 32, no. 14, p. R57, 1999.

[27] J. Kong, *Electromagnetic Wave Theory.* A Wiley-interscience publication, Wiley, 1990.

[28] C. Gabriel, S. Gabriel, and E. Corthout, "The dielectric properties of biological tissues: I. literature survey," *Physics in medicine and biology*, vol. 41, no. 11, p. 2231, 1996.

[29] P. Mantas, "Dielectric response of materials: extension to the Debye model," *Journal of the European Ceramic Society*, vol. 19, no. 12, pp. 2079–2086, 1999.

[30] S. Gabriel, R. Lau, and C. Gabriel, "The dielectric properties of biological tissues: III. parametric models for the dielectric spectrum of tissues," *Physics in medicine and biology*, vol. 41, no. 11, p. 2271, 1996.

[31] K. S. Cole and R. H. Cole, "Dispersion and absorption in dielectrics I. alternating current characteristics," *The Journal of chemical physics*, vol. 9, no. 4, pp. 341–351, 1941.

[32] J. A. Stratton, *Electromagnetic theory.* John Wiley & Sons, 2007.

[33] J. Schuster and R. Luebbers, "An FDTD algorithm for transient propagation in biological tissue with a Cole-Cole dispersion relation," in *Antennas and Propagation Society International Symposium, 1998. IEEE*, vol. 4, pp. 1988–1991, IEEE, 1998.

[34] G. C. Melia, M. P. Robinson, I. D. Flintoft, A. C. Marvin, and J. F. Dawson, "Broadband measurement of absorption cross section of the human body in a reverberation chamber," *Electromagnetic Compatibility, IEEE Transactions on*, vol. 55, no. 6, pp. 1043–1050, 2013.

[35] P. W. Barber, O. P. Gandhi, M. J. Hagmann, and I. Chatterjee, "Electromagnetic absorption in a multilayered model of man," *IEEE Transactions on Biomedical Engineering*, no. 7, pp. 400–405, 1979.

[36] H. P. Schwan and K. Li, "Hazards due to total body irradiation by radar," *Proceedings of the IRE*, vol. 44, pp. 1572–1581, Nov 1956.

[37] H. Massoudi, C. H. Durney, P. W. Barber, and M. F. Iskander, "Electromagnetic absorption in multilayered cylindrical models of man," *IEEE Transactions on Microwave Theory and Techniques*, vol. 27, no. 10, pp. 825–830, 1979.

[38] D. A. Hill, J. G. Van Bladel, J. A. Stratton, L. Josefsson, P. Persson, Y. Zhu, and A. C. Cangellaris, "Time-harmonic electromagnetic fields," 1961.

[39] E. Le Ru and P. Etchegoin, "SPlaC package v1.0 guide and supplementary information," tech. rep., Victoria University, 2008.

[40] D. A. Hill, *Electromagnetic fields in cavities: deterministic and statistical theories*, vol. 35. John Wiley & Sons, 2009.

[41] D. Hill, M. T. Ma, A. R. Ondrejka, B. F. Riddle, M. L. Crawford, R. T. Johnk, *et al.*, "Aperture excitation of electrically large, lossy cavities," *Electromagnetic Compatibility, IEEE Transactions on*, vol. 36, no. 3, pp. 169–178, 1994.

[42] U. Carlberg, P.-S. Kildal, A. Wolfgang, O. Sotoudeh, and C. Orlenius, "Calculated and measured absorption cross sections of lossy objects in reverberation chamber," *Electromagnetic Compatibility, IEEE Transactions on*, vol. 46, no. 2, pp. 146–154, 2004.

[43] R. G. Jackson, *Novel sensors and sensing.* CRC Press, 2004.

[44] R. E. Richardson, "Mode-stirred chamber calibration factor, relaxation time, and scaling laws," *IEEE Transactions on Instrumentation and Measurement*, vol. 34, no. 4, pp. 573–580, 1985.

[45] C. L. Holloway, H. A. Shah, R. J. Pirkl, W. F. Young, D. A. Hill, and J. Ladbury, "Reverberation chamber techniques for determining the radiation and total efficiency of antennas," *Antennas and Propagation, IEEE Transactions on*, vol. 60, no. 4, pp. 1758–1770, 2012.

[46] D. Seni, C. L. Holloway, J. M. Ladbury, G. H. Koepke, and A. aroli, "Absorption characteristics and SAR of a lossy sphere inside a reverberation chamber," in *2014 International Symposium on Electromagnetic Compatibility*, pp. 962–967, Sept 2014.

[47] Z. Tian, Y. Huang, Q. Xu, T. H. Loh, and C. Li, "Measurement of absorption cross section of a lossy object in reverberation chamber without the need for calibration," in *2016 Loughborough Antennas Propagation Conference (LAPC)*, pp. 1–5, Nov 2016.

[48] D. Cox and R. Leck, "Distributions of multipath delay spread and average excess delay for 910-MHz urban mobile radio paths," *IEEE Transactions on Antennas and Propagation*, vol. 23, no. 2, pp. 206–213, 1975.

[49] R. S. A. Oppenheim, *Discrete-time signal processing (2nd edition)*. New Jersey: Prentice Hall, 1998.

[50] I. Glover and P. M. Grant, *Digital communications*. Essex, England: Pearson Education, 2010.

[51] W. B. Davenport, W. L. Root, *et al.*, *An introduction to the theory of random signals and noise*, vol. 159. McGraw-Hill New York, 1958.

[52] M. B. Wilk and R. Gnanadesikan, "Probability plotting methods for the analysis for the analysis of data," *Biometrika*, vol. 55, no. 1, pp. 1–17, 1968.

[53] R. R. Yarlagadda, *Analog and digital signals and systems*, vol. 1. Springer, 2010.

[54] D. W. Marquardt, "An algorithm for least-squares estimation of non-linear parameters," *Journal of the society for Industrial and Applied Mathematics*, vol. 11, no. 2, pp. 431–441, 1963.

[55] C. L. Holloway, H. A. Shah, R. J. Pirkl, K. A. Remley, D. A. Hill, and J. Ladbury, "Early time behavior in reverberation chambers and its effect on the relationships between coherence bandwidth, chamber decay time, rms delay spread, and the chamber buildup time," *Electromagnetic Compatibility, IEEE Transactions on*, vol. 54, no. 4, pp. 714–725, 2012.

[56] J. B. Andersen, J. Nielsen, G. Pedersen, G. Bauch, and M. Herdin, "Room electromagnetics," *Antennas and Propagation Magazine, IEEE*, vol. 49, no. 2, pp. 27–33, 2007.

[57] J. C. for Guides in Metrology/Work Group1 (JCGM/WG1), "Evaluation of measurement data–supplement to the guide to the expression of uncertainty in measurement-propagation of distributions using a Monte Carlo method," 2008.

[58] S. G. Rabinovich, *Measurement errors and uncertainties: theory and practice*. Springer Science & Business Media, 2006.

[59] B. S. Everitt, *The Cambridge dictionary of statistics*. Cambridge University Press, 2006.

[60] M. Abramowitz, I. A. Stegun, *et al.*, "Handbook of mathematical functions," *Applied mathematics series*, vol. 55, no. 62, p. 39, 1966.

[61] I. D. Flintoft, S. J. Bale, S. L. Parker, A. C. Marvin, J. F. Dawson, and M. P. Robinson, "On the measurable range of absorption cross section in a reverberation chamber," *IEEE Transactions on Electromagnetic Compatibility*, vol. 58, no. 1, pp. 22–29, 2016.

[62] U. Kaatze, "Complex permittivity of water as a function of frequency and temperature," *Journal of Chemical and Engineering Data*, vol. 34, no. 4, pp. 371–374, 1989.

[63] B. Riddle, J. Baker-Jarvis, and J. Krupka, "Complex permittivity measurements of common plastics over variable temperatures," *IEEE Transactions on microwave theory and techniques*, vol. 51, no. 3, pp. 727–733, 2003.

[64] K. Seeger, "Microwave measurement of the dielectric constant of high-density polyethylene," *IEEE Transactions on Microwave Theory and Techniques*, vol. 39, no. 2, pp. 352–354, 1991.

[65] J. Clegg, A. C. Marvin, J. F. Dawson, and S. J. Porter, "Optimization of stirrer designs in a reverberation chamber," *IEEE Transactions on Electromagnetic Compatibility*, vol. 47, pp. 824–832, Nov 2005.

[66] R. Armstrong, *Measurement of shielding in electrically large metallic enclosures*. PhD thesis, University of York, 2013.

[67] D. A. Hill, "Electronic mode stirring for reverberation chambers," *IEEE Transactions on Electromagnetic Compatibility*, vol. 36, pp. 294–299, Nov 1994.

[68] C. Tofallis, "A better measure of relative prediction accuracy for model selection and model estimation," *Journal of the Operational Research Society*, vol. 66, no. 8, pp. 1352–1362, 2015.

[69] International Electronical Commission, IEC, "Electromagnetic compatibility (EMC). part 4.21: testing and measurement techniques - reverberation chamber test methods," 2003.

[70] "Emerson & Cuming, ECCOSORB LS permittivity & permeability data." `http://www.eccosorb.com/Collateral/Documents/English-US/Electrical20Parameters/ls20parameters.pdf`. [Online; accessed 13-July-2017].

[71] D. A. Hill, "Boundary fields in reverberation chambers," *IEEE transactions on electromagnetic compatibility*, vol. 47, no. 2, pp. 281–290, 2005.

[72] M. Mitchell, *An introduction to genetic algorithms*. MIT press, 1998.

[73] T. Uusitupa, I. Laakso, S. Ilvonen, and K. Nikoskinen, "SAR variation study from 300 to 5000 MHz for 15 voxel models including different postures," *Physics in Medicine & Biology*, vol. 55, no. 4, p. 1157, 2010.

[74] R. P. Findlay and P. J. Dimbylow, "Effects of posture on FDTD calculations of specific absorption rate in a voxel model of the human body," *Physics in Medicine & Biology*, vol. 50, no. 16, p. 3825, 2005.

[75] I. D. Flintoft, G. C. R. Melia, M. P. Robinson, J. F. Dawson, and A. C. Marvin, "Rapid and accurate broadband absorption cross-section measurement of human bodies in a reverberation chamber," *Measurement Science and Technology*, vol. 26, no. 6, p. 065701, 2015.

[76] G. Melia, *Electromagnetic Absorption by the Human Body from 1-15 GHz*. PhD thesis, University of York, 2013.

[77] A. S. Jackson and M. L. Pollock, "Generalized equations for predicting body density of men," *British journal of nutrition*, vol. 40, no. 03, pp. 497–504, 1978.

[78] A. S. Jackson and M. L. Pollock, "Practical assessment of body composition," *The Physician and Sportsmedicine*, vol. 13, no. 5, pp. 76–90, 1985.

[79] A. S. Jackson, M. L. Pollock, and A. Ward, "Generalized equations for predicting body density of women.," *Medicine and science in sports and exercise*, vol. 12, no. 3, pp. 175–181, 1979.

[80] W. E. Siri *et al.*, "Body composition from fluid spaces and density: analysis of methods," *Techniques for measuring body composition*, vol. 61, pp. 223–44, 1961.

[81] A. Nevill, G. Metsios, A. Jackson, J. Wang, J. Thornton, and D. Gallagher, "Can we use the Jackson and Pollock equations to predict body density/fat of obese individuals in the 21st century?," *International journal of body composition research*, vol. 6, no. 3, p. 114121.

[82] J. V. Durnin and J. Womersley, "Body fat assessed from total body density and its estimation from skinfold thickness: measurements on 481 men and women aged from 16 to 72 years," *British journal of nutrition*, vol. 32, no. 01, pp. 77–97, 1974.

[83] S. Bam, "Body composition, dietary intake and supplement use among triathletes in the western cape region," Master's thesis, Stellenbosch Univeristy, 12 2008.

[84] I. S. for the Advancement of Kinanthropometry, *International Standards for Anthropometric Assessment*. International Society for the Advancement of Kinanthropometry, 2001.

[85] D. Gallagher, S. B. Heymsfield, M. Heo, S. A. Jebb, P. R. Murgatroyd, and Y. Sakamoto, "Healthy percentage body fat ranges: an approach for developing guidelines based on body mass index," *The American journal of clinical nutrition*, vol. 72, no. 3, pp. 694–701, 2000.

[86] P. Tikuisis, P. Meunier, and C. Jubenville, "Human body surface area: measurement and prediction using three dimensional body scans," *European journal of applied physiology*, vol. 85, no. 3, pp. 264–271, 2001.

[87] D. C. Montgomery, E. A. Peck, and G. G. Vining, *Introduction to linear regression analysis*. John Wiley & Sons, 2015.

[88] Y. Lee and K. Hwang, "Skin thickness of korean adults," *Surgical and radiologic anatomy*, vol. 24, no. 3, pp. 183–189, 2002.

[89] M. Lean, T. Han, and C. Morrison, "Waist circumference as a measure for indicating need for weight management," *Bmj*, vol. 311, no. 6998, pp. 158–161, 1995.

[90] D. M. Pozar, *Microwave engineering*. John Wiley & Sons, 2009.

[91] R. F. Harrington and J. L. Harrington, *Field computation by moment methods*. Oxford University Press, 1996.

[92] J. Richmond, "Scattering by a dielectric cylinder of arbitrary cross section shape," *IEEE Transactions on Antennas and Propagation*, vol. 13, no. 3, pp. 334–341, 1965.

[93] R. Harrington and J. Mautz, "An impedance sheet approximation for thin dielectric shells," *IEEE Transactions on Antennas and Propagation*, vol. 23, no. 4, pp. 531–534, 1975.

[94] I.-T. Chiang and W. C. Chew, "Thin dielectric sheet simulation by surface integral equation using modified RWG and pulse bases," *IEEE transactions on antennas and propagation*, vol. 54, no. 7, pp. 1927–1934, 2006.

[95] D. E. Livesay and K.-M. Chen, "Electromagnetic fields induced inside arbitrarily shaped biological bodies," *IEEE Transactions on Microwave Theory and Techniques*, vol. 22, no. 12, pp. 1273–1280, 1974.

[96] S. He, Z. Nie, J. Wei, and J. Hu, "A highly efficient numerical solution for dielectric-coated PEC targets," *Waves in Random and Complex Media*, vol. 19, no. 1, pp. 65–79, 2009.

[97] C. A. Balanis, *Antenna theory: analysis and design.* John Wiley & Sons, 2016.

[98] M. Djordjevic and B. M. Notaros, "Double higher order method of moments for surface integral equation modeling of metallic and dielectric antennas and scatterers," *IEEE Transactions on antennas and propagation*, vol. 52, no. 8, pp. 2118–2129, 2004.

[99] J.-M. Jin, *The finite element method in electromagnetics.* John Wiley & Sons, 2015.